Neuroimaging of Brain Activity using Spatio-temporal Signal Modelling

by

Adil Deniz Duru

B.S., Computer Engineering Istanbul University, 2000

M.S., Biomedical Engineering Bogazici University, 2004

Submitted to the Institute of Biomedical Engineering
in partial fulfillment of the requirements
for the degree of
Doctor
of
Philosophy

Boğaziçi University

2012

Neuroimaging of Brain Activity
using Spatio-temporal Signal Modelling

APPROVED BY:

Prof. Dr. Ahmet Ademoğlu .....
(Thesis Advisor)

Prof. Dr. Mehmed Özkan .....

Prof. Dr. Tamer Demiralp .....

Assoc. Prof. Dr. Ata Akın .....

Assoc. Prof. Dr. Burak Güçlü .....

DATE OF APPROVAL: 18 June 2012

ACKNOWLEDGMENTS

First and foremost, I would like to express my sincere gratitude to my advisor Prof. Dr. Ahmet Ademoğlu for the continuous support of my Ph.D study and research, for his patience and motivation. His guidance helped me in all the time of research and writing of this thesis. I could not have imagined having a better advisor and mentor for my Ph.D study.

Besides my advisor, this dissertation would not have been possible without the guidance of Prof. Dr. Tamer Demiralp. I would like to thank for his encouragement, support and insightful comments.

I would like to express my thanks to the director of Biomedical Engineering Institute at Boğaziçi University, Prof. Dr. Yekta Ülgen for his support.

I would like to thank Prof. Dr. Mehmed Özkan and Assoc. Prof. Dr. Burak Güçlü for their invaluable suggestions.

I would also like to thank Assoc. Prof. Dr. Ata Akın for his support during my study.

I would like to thank the Biomedical Engineering Institute at Boğaziçi University for the oppurtunities I enjoyed during my study.

I thank my labmates in NeuroSignal Analysis Lab: Ali Bayram, Burak Parlak, Esin Karahan, Basri Erdoğan and Burcu Sinem Erdoğan for the stimulating discussions. Also I thank my labmates in Capa Medical School TD-ERP Lab: Itır Kaşıkçı, Zubeyir Bayraktaroğlu, Elif Kurt.

I would like to thank Ayşe Gedik, Gökay Gedik and Dr. Onur Gedik. They

encouraged me during my study.

Special thanks to Asuman Göksel and Metin Göksel for their support and understanding through the duration of my studies.

I wish to thank my parents Süheyla Duru, Arif Şeney Duru and my brother İzzet Paruğ Duru for supporting me unconditionally.

I owe my loving thanks to my wife Dilek Göksel Duru. Without her encouragement and understanding it would have been impossible for me to finish this work.

I would like to dedicate this work to my grandfathers, Adil Duru and İzzet Çelik.

ABSTRACT

Neuroimaging of Brain Activity using Spatio-temporal Signal Modelling

Functional neuroimaging enables us to obtain information about how the brain responds to cognitive and/or emotional tasks. Neuroimaging of brain activity requires spatio-temporal modelling of measured electrical and/or hemodynamic data and integration of the measurements obtained at different spatial and or temporal scales. In this thesis, new techniques are employed for the investigation of spatio-temporal dynamics of different functional data as the EEG-ERP, the invasive/non-nonivasive recordings of epileptic EEG, and simultaneously recorded steady state EEG-fMRI. Spatio-temporal wavelet decompositions using realistic head models are applied in order to produce simple stationary input subtopographies for the source localization. Besides, a spatial decomposition method based on radial basis functions is used. The usage of the subtopographies facilitate the inverse solution and it is shown that even the temporally correlated EEG sources can be localized by this approach. Integration of the data obtained from different spatial scales is an important problem in epileptic EEG. To assess their reliability, the spatial performance of the scalp EEG based inverse solutions are compared with deep or cortical measurements and their simultaneously measured datasets. The multimodal functional information integration is proposed to compare the dynamics deduced by the simultaneously recorded SSVEP and fMRI. The temporal correlation between the time series of EEG and fMRI is calculated via the GLM. It is observed that the SSVEP source maps are the spatial subsets of the fMRI activity. The study demonstrates the applicability and potential of new spatio-temporal methods in EEG research which can be used to study cognition, attention, memory, and perception. Proposed methods can also be used as tools in more practical areas like brain computer interfacing, neurosurgical planning and neuro-psychological assessment of certain disorders.

Keywords: Spatio-temporal, Asymmetric, Subtopography, Wavelet.

ÖZET

Uzay-zamansal İşaret Modelleme ile Beyin Etkinliğinde Nörogörüntüleme

Fonksiyonel nörogörüntüleme bilişsel ve/veya duygusal ödevler sırasında beyin aktivitesi hakkında bilgi edinmemize olanak verir. Beyin aktivitesinin nörogörüntülenmesi, ölçülen elektriksel ve/veya hemodinamik verinin uzay-zaman modellemesini ve farklı uzaysal ve/veya zamansal ölçeklerdeki verinin tümleştirilmesini gerektirir. Bu tez çerçevesinde, EEG-OİP, kafaderisi ve derin elektrotlardan ölçülen epileptik EEG, ve aynı anda kayıt edilmiş durağan hal EEG-fMRg gibi fonksiyonel ölçümlerin uzay-zaman dinamiklerini araştırmak amacıyla yeni teknikler incelendi. Kaynak yerelleştirme işlemine girdi olarak basit durağan alttopografiler üretmek için gerçekçi kafa modeli kullanan uzay-zaman dalgacık dönüşümleri uygulandı. Ayrıca, radyal baz fonksiyonları temel alan uzaysal ayrıştırma metodu kullanıldı. Alttopografilerin kullanımı geri yön çözümünü kolaylaştırdığı ve bu yaklaşımla ilintili EEG kaynaklarının bile yerelleştirilebildiği gösterildi. Farklı uzaysal ölçeklerdeki verinin bütünleştirilmesi epileptik EEG'nin önemli sorunlarından biridir. Kafaderisi EEG verisini kullanarak yapılan geri yön çözümü, derin, kortikal ölçümler ve bu ölçümlerin aynı anda kayıt edilmiş verikümeleri ile karşılaştırılarak, geri yön çözümünün güvenilirliği incelendi. Çoklumodalite fonsiyonel bilgi tümleştirilmesi, aynı anda kayıt edilen durağan hal görsel uyarım potansiyelleri ve fMRg ölçümlerinden ortaya çıkarılan dinamikleri incelemek için önerildi. EEG ve fMRg zaman serileri arasındaki ilinti, genel doğrusal model kullanılarak hesaplandı. Durağan hal uyarılma potansiyeli kaynaklarının fMRg aktivitesinin uzaysal altkümesi olduğu gözlendi. Bu çalışma, bilişsel, dikkat, hafıza ve algı çalışmalarının yapılabileceği EEG araşırmalarında, yeni uzay-zaman metodlarının uygulanabilirliği ve potansiyelini göstermektedir. Önerilen metodlar, beyin-bilgisayar arayüzü, nörocerrahi planlama ve bazı bozuklukların nöro-psikolojik değerlendirmesi gibi pratik alanlarda kullanabilecek birer araç olarak kullanılabilir.

Anahtar Sözcükler: Uzay-zaman, Asimetrik, Alttopografi, Dalgacık.

TABLE OF CONTENTS

ACKNOWLEDGMENTS iii
ABSTRACT v
ÖZET vi
LIST OF FIGURES x
LIST OF TABLES xiv
LIST OF SYMBOLS xv
LIST OF ABBREVIATIONS xvii
1. INTRODUCTION xix
1.1 General Objectives and Motivation xix
1.2 Outline of the thesis xxiii
2. Theoretical basis of EEG Source Reconstruction 1
2.1 Origin of the EEG 1
2.2 Forward Problem of EEG 3
2.2.1 Boundary Element Method 6
2.3 EEG Source Reconstruction 8
3. Subtopographic EEG decomposition in Neuroimaging 13
3.1 Spatio-temporal modeling of EEG 13
3.2 Spatial decomposition using Radial Basis Functions 14
3.2.1 Estimation of Radial Basis Function Parameters 14
3.2.2 Application to simulated data 17
3.3 Spatial Wavelet decomposition of the topographies 19
3.3.1 Continuous Wavelet decomposition 20
3.3.2 Discrete Wavelet decomposition of spatial topographies 20
3.3.3 Application to simulated data 22
3.3.4 Source Reconstruction of Simulated Data 23
3.4 Spatio-Temporal Wavelet Decomposition on Realistic Head Model . . . 24
3.4.1 Flattening with contortion 26
3.4.2 Implementation of the algorithm to simulated data 27
3.4.3 Application to real data 34

3.4.4 Results & Discussion 38
3.5 Discussion & Conclusion 38
4. Epilepsy in Neuroimaging 42
4.1 Clinical approach to epilepsy 42
4.2 Non-invasive and invasive imaging of epileptic sources 45
4.2.1 Finite Difference Method 46
4.2.2 Electrical source imaging with LORETA 48
4.2.3 Electrical source imaging using, hierarchical observation model and Bayesian approach 49
4.2.4 Case 1: Epileptic source reconstruction using deep and scalp EEG 51
4.2.5 Case 2: Epileptic source reconstruction using subdural and scalp EEG 53
4.2.6 Case 3: Epileptic source reconstruction using simultaneously measured deep and scalp EEG 57
4.3 Discussion and Conclusion 60
5. Multimodal functional neuroimaging: EEG & fMRI fusion 62
5.1 EEG & fMRI fusion theory 62
5.2 Steady State Visual Evoked Potentials 65
5.3 Asymmetric Temporal Fusion of EEG & fMRI 67
5.3.1 Localization of Brain activity with BOLD Signal Changes . . . 67
5.3.2 General Linear Modelling 68
5.3.3 Simultaneously recorded EEG&fMRI 70
5.3.3.1 Experimental Setup and Stimulation 70
5.3.3.2 MRI data acquisition 72
5.3.3.3 EEG data acquisition 72
5.3.4 General Analysis Scheme 73
5.3.5 EEG data analysis & source energy maps 73
5.3.6 EEG & fMRI processing 75
5.3.7 EEG informed fMRI processing 77
5.4 Results 78
5.5 Discussion and Conclusion 82
6. General Summary and Conclusion 87

APPENDIX A. The Appendices A-D offer the list of publications originated from the of Ph.D. dissertation study. 92
A.1 Publications in Journals 92
A.2 Publications in Books 92
A.3 Conference Proceeding Papers 93
A.4 National Conference Proceedings 94
A.5 Conference Abstracts 96
REFERENCES 99

LIST OF FIGURES

Figure 2.1 Illustration of amplitudes and time periods of IPSP, EPSP and AP with respect to RMP. 2

Figure 2.2 The presynaptic neuron (1) has its axonal termination at the basal dendrites of postsynaptic neuron (2) which undergoes an EPSP. The EPSP event induces specific channels to open and inflow of Na^+ takes place. Thus, the neuron behaves as a current dipole shown as the arrow. 3

Figure 2.3 Relation of measured signals $V_i(t)$ and the dipole moments $j_i(t)$ of the primary currents. 5

Figure 3.1 Mesh images of *2D* RBF Morlet kernel and Gaussian kernel, respectively. 15

Figure 3.2 *2D* topography of simulation data for the a) superficial source and b) deeper source, c) superimposition of these two subtopographies, d) location of the superficial and deeper source, respectively. 16

Figure 3.3 a) Original raw subtoporaphies. b) Approximation and detail subtopographies decomposed using Morlet RBF and c) Gaussian RBF kernels. 17

Figure 3.4 *2D* topographies of decomposed subtopographies based on Morlet and Gaussian RBF. Source localization of the corresponding topographies using MUSIC algorithm. 18

Figure 3.5 *3D* spatial wavelet decomposition on a regular volumetric grid. 19

Figure 3.6 Axial slices of the segmented raw MRI data and the gray matter, white matter and CSF images 22

Figure 3.7 Realistic scalp model developed from T1 weighted human brain MRI data 23

Figure 3.8 Triangulated surfaces of Scalp, skull and CSF tissues 23

Figure 3.9 Topographies of the sources and the inverse solutions of the subtopographies 25

Figure 3.10	Illustration of flattening and contortion method.	27
Figure 3.11	The decomposition and reconstruction filter coefficients of discrete Meyer wavelet.	28
Figure 3.12	The decomposition and reconstruction filter coefficients of biorthogonal wavelet.	29
Figure 3.13	Source configuration of the simulated ERP data.	30
Figure 3.14	Topographies of simulated data temporal wavelet coefficients.	31
Figure 3.15	Delta 3 subtopography of spatio-temporal wavelet coefficients and their source localization results.	32
Figure 3.16	Delta 6 subtopography of spatio-temporal wavelet coefficients and their source localization results.	33
Figure 3.17	Alpha 11 subtopography of spatio-temporal wavelet coefficients and their source localization results.	35
Figure 3.18	30 channel averaged ERP activity for Go and NoGo CPT respectively. Sampling Rate is 200 Hz and the duration is 1.5 second.	36
Figure 3.19	i)Temporal Decompositon (Delta Coefficient 3 (350-525ms)) ii)5 octave Spatial Decomposition and Localization for D3	37
Figure 3.20	i)Temporal Decompositon (Theta Coefficient4 (525-700 ms)) ii)5 octave Spatial Decomposition and Localization T4	39
Figure 4.1	0 unit voxel element, Δx, Δy, Δz distances to the neighbouring voxels	46
Figure 4.2	A center voxel is denoted with yellow color and its 6 orthogonal neighbours are represented with gray marks.	49
Figure 4.3	Sagittal, coronal, axial and *3D* views of postoperative T1 weighted MR images. Deep electrode locations are marked on the slices (Data is obtained from Czech Republic, Brno Epilepsy Center).	51
Figure 4.4	a)The realistic head model formed by triangulated surfaces of the scalp, skull and brain tissues. b) 19 electrodes are registered to scalp surfaces. Blue colored triangles denote the electorde locations. c) Red points denote the contact points of the deep electrodes. Deep electrodes are placed to the left hemisphere of the brain.	52

Figure 4.5 a)The source locations obtained from the deep electrodes using the FDM based, b) from the scalp EEG using the BEM based LORETA approach, respectively (activity is normalized individually). c) Average Scalp EEG topography of the selected 1150 peaks. 53

Figure 4.6 a) Scalp model is obtained using the MR images. b) Concentric surfaces of scalp, skull and the brain tissue having homogeneous conductivity values are triangulated with 2466, 2340, 1575 vertices and 4837, 4574, 3146 triangles, respectively. c) Cortical source space used for the inverse problem. 54

Figure 4.7 a) MR image, b) White dots in the CT images denote the locations of the subdural electrode contacts 55

Figure 4.8 Placement of the subdural electrodes to the right hemisphere of the subject during an invasive operation (Image is obtained from Neurosurgery Department, Cerrahpasa Medical School). 55

Figure 4.9 Subdural electrode source localization is shown in yellow, scalp EEG source localization is shown in red and the locations of the other subdural contact points are drawn with gray color. 56

Figure 4.10 Scalp model is represented with 5000 triangles and 2500 vertices. 22 electrode locations are registered to the scalp model using international $10-20$ electrode placement system. 56

Figure 4.11 Preictal period topographic distribution of the electrical potentials and the correponding source images on the cortical surface estimated through the linear inverse solution. 56

Figure 4.12 (Left) The anotomical location that is thought to be responsible from the seizures is marked with a yellow ellipse. (Right) The source locations that are estimated by the inverse solution for 4 different seizures are marked with colored spheres. 57

Figure 4.13 Postoperative T2 wieghted MR images. The locations of the deep electrodes are shown with colored markers (64 contacts). 58

Figure 4.14 Locations of the deep electrode contacts are shown; i) on the T2 weighted MR images and ii) on the cortical source space. 59

Figure 4.15	a) Deep electrode activity of preictal period b) Preictal deep electrode activity amplitude greater than its 80% of the maximum value c) Source activity deduced from the linear inverse solution d) The temporal dynamics of the deep electrode measurements which are projected to the cortical surface (sampling rate: 1024 Hz) e) The temporal waveform obtained through the linear inverse solution.	59
Figure 5.1	A typical design matrix of a voxel for multiple subjects.	70
Figure 5.2	Stimulus Paradigm	71
Figure 5.3	The locations of the sensors are marked with associated labels. The scalp surface, canonical cortical surface (left) and the scalp, inner skull surfaces (right) of the realistic head model are plotted.	74
Figure 5.4	EEG source energy pattern and energy computation filter structure for 6 Hz stimuli	76
Figure 5.5	The BOLD and SSVEP time series of the voxels for a single subject	78
Figure 5.6	BOLD and SEM_f mean voxel signal intensity time series for the unimodal fMRI, EEG and fusion areas analysis of $8Hz$ stimulation frequency	79
Figure 5.7	The spatial activation patterns for 8Hz stimulus frequency.	81
Figure 5.8	The activation patterns for 6Hz and 10Hz stimulus frequencies.	82
Figure 5.9	The activation patterns for 12Hz and 14Hz stimulus frequencies.	83

LIST OF TABLES

LIST OF SYMBOLS

V	Electrical potential
j	Current Density Vector
J	Current Density matrix
L	Leadfield Matrix
e	Error term
A^T	Transpose of matrix A
A^{-1}	Inverse of matrix A
Cov	Covariance function
n_e	Number of electrodes
n_t	Temporal length of a signal
mV	milliVolt
ms	milliSecond
σ_s	Conductivity value of the s tissue
r_{dip}	Indice of an electrical dipole
$N(0, \sigma^2 I)$	Normal distribution with 0 mean and σ^2 variance
ϵ	Measurement error
diag(A)	vector containing the elements of the leading diagonal of A
$\vec{\nabla} a$	gradient of a
S_j	$j.th$ surface
N_{tr}^j	number of triangles of the $j.th$ surface
Δ_i^j	$i.th$ triangle of the $j.th$ surface
$\vec{n}(s)$	unit normal vector of s to the surface
$\Omega^(i,j)(s)$	the solid angle of s subtended by the $(i,j).th$ triangle
G	free space potential matrix
M	Linear Inverse filter
C_e	Covariance of observation noise
C_p	Source covariance matrix
$\theta(x)$	Radial basis function

$V_t(x, y)$	Topographic EEG data of point x, y at time indice t
α	Parameter set of a radial basis function
$F(\alpha)$	Radial basis function estimation error
$J(\alpha)$	Jacobian of the radial basis function expressed with the parameter α
d_t	direction of the solution
$h_{a,b}(t)$	wavelet function
$CWT_f(a, b)$	Continuous wavelet decomposition
W	The time-frequency constraint matrix
$A_u(j+1)$	The approximation at level $j+1$ of *1D* decomposition
$D_u(j+1)$	The detail at level $j+1$ of *1D* decomposition
$A_{u,v}(j+1)$	The approximation at level $j+1$ of *2D* decomposition
$D_{u,v}(j+1)$	The detail at level $j+1$ of *2D* decomposition
X	Design matrix
β	Regressor coefficient vector
mm	millimeter
$n_{vertice}$	Number of vertices
n_{scans}	Number of scans
S	Temporal covariance filter
Q_1	Covariance structure of the sensor space
Q_2	Covariance structure of the source space
V_e	Temporal correlation matrix
V_p	Temporal correlation structure of the sources
SEM	Source Energy Map

LIST OF ABBREVIATIONS

AP	Action Potential
AR	Auto Regressive
BCG	Ballistocardiography
BEM	Boundary Element Method
BOLD	Blood Oxygenation Level Dependency
COG	Centre of Gravity
CPV	Constant Potential at Vertices
CT	Computed Tomography
CWT	Continuous Wavelet Analysis
DCT	Discrete Cosine Transform
DT-MRI	Diffusion Tensor-Magnetic Resonance Imaging
DWT	Discrete Wavelet Analysis
ECD	Equivalent Current Dipole
EEG	Electroenchephalography
EPI	Echo Planar Imaging
EPSP	Excitatory Post-synaptic Potential
ERP	Event Related Potential
FDM	Finite Difference Method
FEM	Finite Element Method
FFT	Fast Fourier Transform
fMRI	Functional Magnetic Resonance Imaging
FOCUSS	FOCal Underdetermined System Solution
FWHM	Full Width Half Maximum
GLM	General Linear Model
IED	Interictal Epileptiform Discharge
ISI	Inter Stimulus Interval
HRF	Hemodynamic Response Function
ICA	Independent Component Analysis

IPSP	Inhibitory Post-synaptic Potential
LAURA	Local Autoregressive Average
LORETA	Low Resolution Electro Magnetic Tomography
LPV	Linear Potential at Vertices
MAP	Maximum a Posteriori
MNE	Minimum Norm Estimation
MRI	Magnetic Resonance Imaging
MUSIC	Multiple Signal Classification
OLS	Ordinary Least Squares
PCA	Principal Component Analysis
PET	Positron Emission Tomography
PsP	Post-synaptic Potential
RMP	Resting Membrane Potential
ReML	Restricted Maximum Likelihood
SEM	Source Energy Map
sLORETA	Standardized Low Resolution Electro Magnetic Tomography
SPM	Statistical Parameter Mapping
SSVEP	Steady State Visual Evoked Potential
TR	Repetition Rate

1. INTRODUCTION

1.1 General Objectives and Motivation

Functional neuroimaging is a branch of medical imaging that is used for the diagnosis of the diseases and to assess the brain health. In addition to diagnostic purposes, functional neuroimaging studies enable researchers to obtain information about how the brain works and how it responds to cognitive or emotional tasks. Neuroimaging helps us to identify distinct neural events that are detectable at different spatial and temporal scales.

In recent years, functional neuroimaging utilizes a number of technologies to directly or indirectly measure the chemical and electrical changes occured in the brain tissue. The responses that correspond to the changes in metabolic cellular activity are measured with single-photon emission tomography (SPECT) [1] and positron emission tomography (PET) [2] using radioactive substances. Despite the usage of radiation, these indirect measurements produce images having poor temporal and spatial resolution.

As a non-invasive method, functional magnetic resonance imaging (fMRI) is used to measure the changes of the blood flow or oxygenation in the brain with a better spatial resolution [3]. Therefore, fMRI is widely used to determine the spatial locations of the regions that are involved in a given task. These techniques undoubtely provide functional maps with high spatial resolution where the temporal resolution of the measured signals is on the order of seconds. Among these techniques, the best temporal resolution can be achieved by fMRI but it is limited to several seconds due to the latency of the hemodynamic response. Moreover, the fMRI signal is very sensitive to movement artifacts and its analysis is complex and time consuming.

Conversely, noninvasive electromagnetic imaging modalities, electroencephalog-

raphy (EEG) and magnetoencephalography (MEG) provide high temporal resolution with low spatial resolution [4]. Based on Berger's discovery [5] that the brain electrical activity could be measured using the scalp electrodes, EEG is considered as the oldest functional brain imaging technique (1929). It records transient electrical dipoles generated by the net flow of electrical current across the cellular membrane during neuronal depolarisation associated with postsynaptic potentials. As a convenient and relatively inexpensive technique, EEG is used to explore the abnormalities in the electrical activity of the brain that are formed by the brain disorders or diseases such as epilepsy. In addition to this, event related potential (ERP) measurements are obtained in order to observe the response of a subject to a given task. The neuronal activity within the brain is modelled using current sources whose locations and amplitudes are determined by solving the EEG inverse problem [6, 7]. This way, a spatio-temporal functional map can be obtained based on EEG. The accuracy of the EEG inverse solution is directly related with the complexity of the EEG topographic maps. Therefore, prior to inverse solution, temporal and spatial pre-processing techniques should be applied in order to produce simple stationary input patterns for the source localization process. However, precise localization of the activity in the brain using neuroimaging measurements is one of the main challenges in the area of functional imaging.

Time-frequency analyses are performed to isolate stationary frequency components in temporal windows and their corresponding source images are obtained by solving the EEG inverse problem [8, 9]. The pre-processing methodologies based on time-frequency analyses are improved by introducing spatial smoothness contrainsts [10], artificial assumptions as indepence in ICA or uncorrelatedness in PCA approaches [11] in the optimization step. Moreover, multichannel EEG data is decomposed to unique components of channel/frequency/time [12] as an alternative to previous preprocessing methods. In addition to these studies, the spatial frequency characteristics of the EEG/ERP topographies are explored and the scalp topographies are expressed as the summation of simpler maps [13]. Thus, by using the spatio-temporal decomposition methods on realistic head models, the spatial resolution of the EEG inverse solution can be improved. A spatio-temporal preprocessing of the EEG simplifies the complexity of the scalp map by separating it into several submaps each of which is

produced by an individual EEG source combination. This is a very convenient preprocessing prior to source localization for the isolation of different maps corresponding to different dipole sources. This way, even the temporally correlated EEG sources can be localized after spatio-temporal decomposition of EEG.

In clinical applications, EEG recordings are commonly used in the multiaxial diagnosis of epilepsy. The spatio-temporal activation maps are explored for the analysis of the seizures. As a diagnosis and therapy planing tool, EEG is used to identify the locations of the brain sources that generates focal seizures. It is criticaly important to identify the source locations of seizure activity for the epileptic surgery. This undoubtedly provides a very important information to the clinical team for the surgical planning. Once the focal point is found, its surgical resection prevents the future epileptic attacks. The parametric spatio-temporal source localization procedures were implemented using spherical head models with EEG [14], MEG [15] and the results were shown to be in agreement with the corresponding structural MR findings. Distributed source localization methods are also used in the imaging of the epileptogenic regions [16]. It requires to locate the epileptic focus using the EEG data recorded from the surface as well as from the deep sites located in the brain in order to improve the widely accepted current surgical planning approach. Recently, electrical measurements are obtained directly from the brain tissue in order to minimize the conductance effect of the skull. The findings of the invasive measurements are considered to give more reliably information about the origin of the seizures. However, the placement of the electrodes into the brain tissue or onto the cortex is a risky operation for both, the surgeon and the patient. For that reason, the noninvasive EEG measurement may provide sufficient information instead of using the invasive electrodes.

The spatial resolution limitation of the EEG can also be improved with the use of multimodal functional neuroimaging measurements such as EEG-fMRI. Combining the high temporal resolution of EEG source maps and the millimeter-scale fMRI measurements provides us with a more accurate picture of the functional processing in the human brain both, temporally and spatially. First attempts of the simultaneously recorded EEG-fMRI integration was the localization of the epileptic regions by com-

bining the high resolution fMRI spatial maps with the temporal localization of the seizure obtained through the EEG [17, 18, 19]. This type of spatio-temporal integration where the temporal information of EEG is used as a predictor for the fMRI, is an example of asymmetric fusion. Asymmetric approaches rely on constraining the extent of activation, either in space or in time, in one modality by the information provided from the other, as a prior. Generally, the EEG data collected from a few electrodes are chosen to be used for the EEG-fMRI integration scheme [20]. Conventional statistical fMRI analysis technique called General Linear Modeling, (GLM) is used for the investigation of the relation between the scalp EEG and the voxel time series obtained from the fMRI [21]. Separate GLM analyses of the EEG and the fMRI data were also performed and the spatial coincidence of the resulting maps were also analyzed [22]. On the other hand, spatio-temporal analysis of EEG source maps can be obtained by using spatial constraints obtained from other functional neuroimaging modalities. As another example of an asymmetric integration, the location of EEG sources is estimated using the spatial information provided from fMRI activations as prior information [23, 24, 25, 26, 27, 28]. For the analysis of EEG&fMRI data, a common spatio-temporal solution domain is needed that has the capability to include both spatial and temporal properties of the datasets without any loss of information. This common spatio-temporal domain undoubtedly enables us to investigate the relationship between the sources of electrical and hemodynamic activities.

In this thesis, the spatio-temporal properties of the brain dynamics are investigated by analyzing various functional measurements including the EEG-ERP, the invasive and the non-nonivasive recordings of epilepsy patients, and the simultaneously recorded steady state EEG-fMRI data. New discrete techniques are proposed for the investigation of spatio-temporal dynamics of the simulated and real EEG-fMRI recordings. Moreover, a multimodal functional information integration procedure is proposed to analyze the relation between the neuronal dynamics deduced by the simultaneously recorded EEG and fMRI.

1.2 Outline of the thesis

The historical overview and the mathematical principles of the EEG source localization procedures are summarized in the second Chapter. In the thirth Chapter of the thesis, spatial preprocessing techniques to decompose the EEG topographies into simpler subtopographies are proposed. In the first stage, Radial Basis Functions are used as kernel functions in order to explain the EEG topographies with simpler subtopographies. Afterwards, a spatial preprocessing technique is proposed that is based on the spatial frequency characteristics of the topographies. *1D* discrete wavelet transform is implemented on a *3D* cartesian space as spatial filters that decompose the topographies into subtopographies. The technique is also integrated into a new algorithm based on a contorted and flattened realistic scalp model. The proposed spatio-temporal decomposition techniques are applied to simulated and to averaged ERPs datasets and results are presented. In the fourth Chapter, source reconstruction algorithms are applied to the clinical epilepsy datasets. Both, the parametric and linear inverse solution methodologies are applied to the invasive and non-invasive EEG recordings. *RAP-MUSIC* method is used for the parametric solution while LORETA and Bayesian source reconstruction methods are applied for the linear case. The inverse solution accuracy of scalp recordings is determined using the reference information obtained through the invasive recordings. Moreover, simultaneously measured invasive and non-invasive recordings of an epilepsy patient, are used to investigate the spatial and temporal dynamics of the underlying sources. In Chapter 5, a novel voxel wise EEG&fMRI information integration (fusion) method is proposed that allows the investigation of the brain activity using the simultaneously measured EEG&fMRI data. In the Chapter 6, a general discussion and conclusions of the results and further recommendations are given.

2. Theoretical basis of EEG Source Reconstruction

2.1 Origin of the EEG

The human brain is composed of three primary divisions; brainstem, cerebellum and cerebrum. The cerebral cortex is the outer portion of the cerebrum and consists of strongly interconnected cortical neurons. The neuron's task is to process and transmit signals. The information in the neuron is in the form of electrical potentials across the membrane. Information is transmitted via the synapse by the arrival of neurotransmitter on receptors and this triggers the postsynaptic potentials (PSPs).

Active neurons secrete a neurotransmitter, which is a chemical substance, at the synaptical side. The synapses are mainly localized at the dendrites and the cell body of the postsynaptic cell. A postsynaptic neuron has a large number of receptors on its membrane that are sensitive for this neurotransmitter. The neurotransmitter in contact with the receptors changes the permeability of the membrane for charged ions which causes a depolarization or a hyperpolarization [29].

The synaptic inputs to a neuron are of two types: those that produce excitatory postsynaptic potentials (EPSPs) accross the membrane of the target neuron, thereby making it easier for the target neuron to fire an action potential (AP) and the inhibitory postsyanptic potentials (IPSPs), which act in the opposite manner on the output neuron [30].

An IPSP pushes the resting membrane potential (RMP is about -70 mV [31]) down to more negative values and away from its firing potential. If two EPSPs with sufficiently large ampltides occur in a small time frame, the cell would fire an AP. The AP is the signal that can be sent down the axon to create a PSP in another neuron [32].

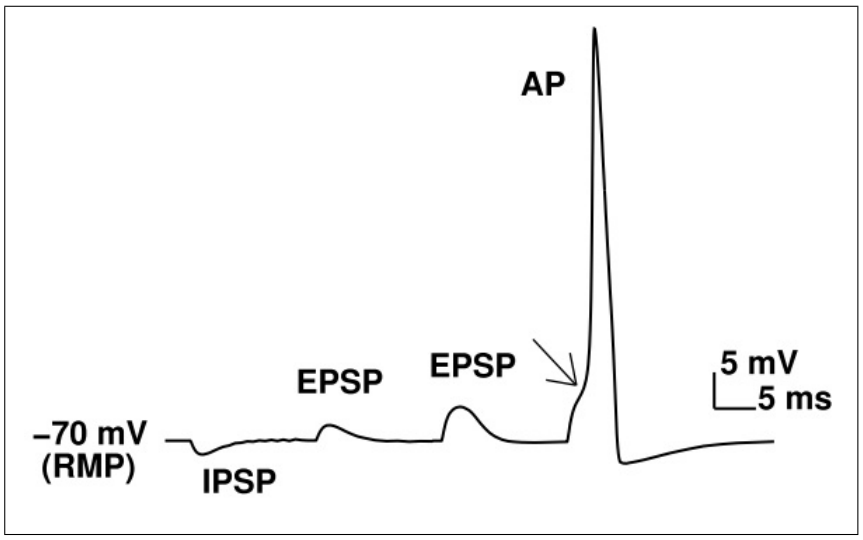

Figure 2.1 Illustration of amplitudes and time periods of IPSP, EPSP and AP with respect to RMP. The amplitude of the APs is $70-110$ mV and the time course is 0.3 ms while the time course of EPSP is $10-20$ ms.

The postsynaptic potentials are the generators of the extracellular potential field and the summation of activities of a large group of neurons that are synchronously electrically active can be detected from the scalp electrodes.

The principle EEG generators are the dipole layers of pyramidal neurons in the cortical gray matter. The relationship between the scalp measurements at some distance from the generator and the flow of current through the extracellular space can be described using the volume conduction theory. The solid angle theorem of the volume conduction states that the potential generated by a dipole layer in a volume conductor measured at any point in the conductor is proportional to both the generator's potential and the solid angle subtended by the dipole layer at the point of measurement.

The electrical field generated from convoluted layers of pyramidal neurons is reffered to as an open field. The field potential around an open field decays inversely to the distance from the generator and can be viewed from almost any distance in a volume conductor. There are structures in the central nervous system in which groups of cells and their processes are not aligned as dipoles and are referred to as close fields. Structures in the thalamus and brain-stem generate closed field potentials and are not large enough to be detected by scalp electrodes. [33]

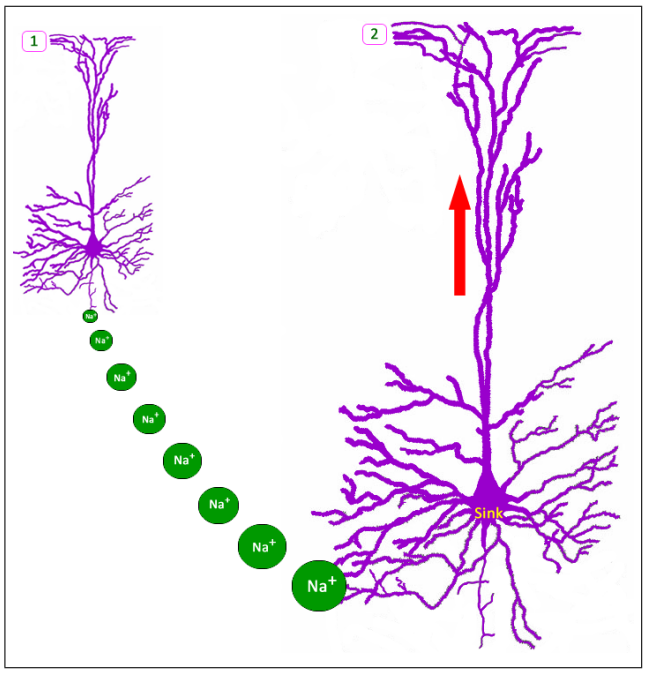

Figure 2.2 The presynaptic neuron (1) has its axonal termination at the basal dendrites of postsynaptic neuron (2) which undergoes an EPSP. The EPSP event induces specific channels to open and inflow of Na^+ takes place. Thus, the neuron behaves as a current dipole shown as the arrow.

2.2 Forward Problem of EEG

The process of calculating the scalp potentials using the current sources inside the brain is referred to as the forward problem in EEG. The electromagnetic properties of the head and the location of the electric current generators in the brain are assumed to be known for the solution of the forward problem.

The scalp electric potential $V \in \Re^{n_e \times n_t}$ at all electrodes can be formulated as Eq. 2.1

$$V = Lj + \epsilon \tag{2.1}$$

where n_e is the number of electrodes, n_s is the number of sources, n_t is the number of samples, $L \in \Re^{n_e \times n_s}$ is the leadfield matrix, $j \in \Re^{n_s \times n_t}$ is the dipole activity strentgh vector and $\epsilon \in \Re^{n_e \times n_t}$ is the additive noise at the sensors.

The lead field matrix is a deterministic transfer function that transforms the

electrical activity of the brain tissue to the electrical potential vector of the sensors placed on the head model. The lead field matrix is influenced by the structure and electrical conductivity values of the head model which is used for solving the electromagnetic Maxwell's equations [34].

The assumptions on the electrical conductivity values of the skull, scalp, CSF and the model chosen determine the approach for the solution of the forward problem. The conductivity values of these tissues were computed using electromagnetic impedance tomography [35, 36], intracranial and scalp electrodes [37] and the conductivity of scalp/skull ($\sigma_{scalp}/\sigma_{skull}$) was found to be between $15 - 80$.

The skull tissue shows low conductivity in the radial and high conductivity in the tangential directions [38]. The conductivity values of gray matter, scalp and CSF are isotropic in all directions, hence σ can be represented with a scalar value for a specific location (isotropic conductivity) whereas the components of the skull and white matter have anisotropic conductivity which means that the conductivity values of the tissues are not identical in every direction [39]. Recently, DT-MRI measurements enable researchers to relate the conductivity values of a voxel with its directional information on the diffusion of the water and it is assumed that the conductivity is highest in the direction in which the water diffuses most easily [40, 41].

The presence of anisotropic conducting tissues affects the computation of the forward and, as a consequence, the inverse problem [42]. It has been shown that anisotropic conducting compartments should be incorporated in volume conductor models of the head whenever possible [43] [44] [45].

The simplest head model used in EEG forward problem is the single spherical shell model. The entire conducting volume is modelled as a sphere of constant conductivity. The single spherical shell is too unrealistic as a model for the head due to the large difference between the conductivities of brain and skull.

The basic head model is as a set of concentric homogeneous volume conductors;

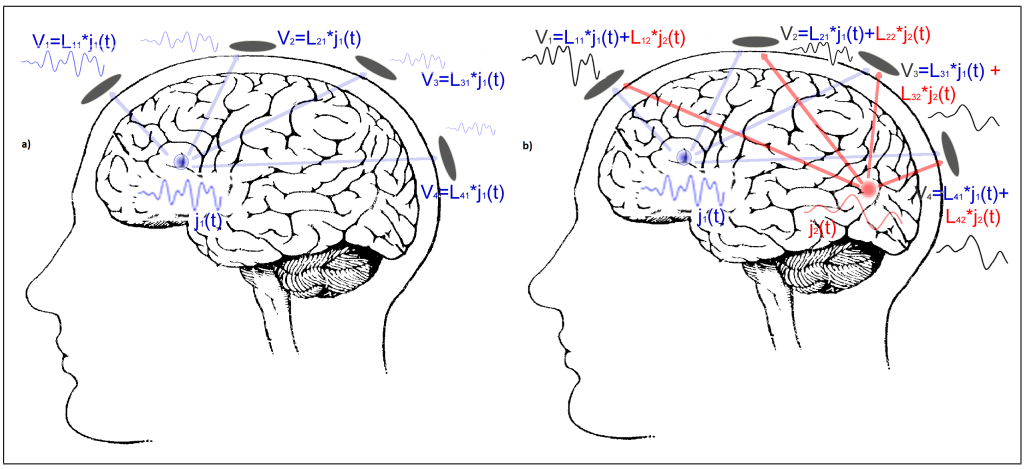

Figure 2.3 Relation of measured signals $V_i(t)$ and the dipole moments $j_i(t)$ of the primary currents: a)A time dependent dipole moment $j_1(t)$ (red trace) is seen by the sensor 1 with a leadfield coefficient L_{11} and scaled versions are projected to the sensors $2, 3, 4$. b)In the presence of a second source $j_2(t)$, linear mixture of the source signals weighted with the leadfield L are seen by the sensors.

the scalp, the skull, the CSF and the brain. For this model geometry, analytical solutions are derived for the forward problem for both the isotropic [46] and anisotropic cases [47].

A realistic volume conductor model derived from individual MR Images (or CT) increases the accuracy of the reconstruction algorithms. It was shown that the efficiency of the forward calculations can be improved by replacing the spherical geometry with a more realistic head shape extracted from anatomical images [48, 49]. How the actual geometry of the head [50, 51, 52] together with the varying thickness and curvatures of the skull affects the forward solutions are discussed [53, 54]. Recently, realistic head models are used in conjunction with either boundary-element (BEM), finite-element (FEM), or finite-difference (FDM) methods. The computational requirements for a realistic head model are higher than that for a multi-layer sphere.

The realistic head model is formed by extracting the brain, the cerebro-spinal-fluid, the skull and the scalp compartments from the anatomical data. To enable the extraction of the various surfaces of different tissues, the anatomical data has to be segmented. MR images can be segmented into different tissue classes using several statistical clusterin methods [55, 56]. The segmented anatomical data obtained from

MRI is used to form the head model. Depending on the type of the forward solution method, either the boundaries or the solid volumes of these segmented tissue models are used.

2.2.1 Boundary Element Method

As a numerical approach, BEM is capable of calculating the potential values at the interfaces and boundary of the volume induced by a given current source which is based on the hypothesis that the head model volume is divided into a set of homogeneous contiguous regions having isotropic conductivity values [57, 58, 59, 60, 61]. The surfaces (boundaries) separating these regions are further tessellated with the triangles [62] and the potential V is computed over triangles. The potential V can be considered to be constant for each location over a triangle. Thus one value is obtained for each triangle and this value is computed at the centre of gravity of each triangle (COG approach) [63, 64]. The potential value of a point on a triangle can be calculated using the potential values of the vertices at that triangle. If the potential over a triangle is assumed to be constant, the mean value of the potential at its vertices is used (Constant Potential at vertices CPV) [65]. Besides this, the potential can be assumed to vary over the triangles. In this case, the potential value at a point over a triangle is linearly weighted with the potential values of the vertices forming the triangle (Linear Potential at Verices LPV).

$$V(\vec{s}) = V_{\infty}(\vec{s}) - \frac{1}{2\pi}\sum_{l=1}^{3}\frac{\sigma_l^- - \sigma_l^+}{\sigma_k^- + \sigma_k^+}\sum_{m=1}^{N_{tr}^{(l)}}\int_{\Delta_m^{(l)}} V(\vec{s})\nabla'\left(\frac{1}{|\vec{s} - \vec{s}'|}\right)\vec{n}(\vec{s'})dS' \qquad (2.2)$$

Centre of gravity approach of BEM is implemented as the solution of the forward problem. Once the nodal points of the tesellated surfaces are determined, BEM COG approach is used to find the potentials on the nodes given the dipole parameters. The electrical potential $V(\vec{s})$ at any surface point $\vec{s}$ can be represented by Eq. 2.2

where, σ_i^+ and σ_i^- are the conductivities belonging to the outside and inside of the surface S_j, respectively, $\vec{n}(\vec{s'})$ is the unit normal vector of $\vec{s'}$ to the surface. Surfaces are approximated by a set of plane triangles. The surface S_l can be represented with N_{tr}^l triangles by Δ_m^l. V_∞ is the potential in an infinite extent conductor with unit conductivity due to N_j sources at $\vec{r}_i \quad i = 1...N_j$ with strength $\vec{j}(\vec{r}_i)$ and computed by Eq. 2.3.

$$V_\infty(\vec{s}) = \frac{1}{2\pi(\sigma_k^- + \sigma_k^+)} \sum_{i=1}^{N_j} \frac{(\vec{s} - \vec{r}_i)}{|\vec{s} - \vec{r}_i|^3} \vec{j}(\vec{r}_i) \tag{2.3}$$

The integral in Eq. 2.2 can be rewritten for COG approximation as in Eq. 2.4

$$\int_{\Delta_m^{(l)}} V(\vec{s}) \nabla' (\frac{1}{|\vec{s} - \vec{s'}|}) \vec{n}(\vec{s'}) dS' = -V(\vec{s}_{cog}) \Omega^{(l,m)}(\vec{s}) \tag{2.4}$$

where $\Omega^{(l,m)}(\vec{s})$ is the solid angle subtended by the triangle $\Delta_m^{(l)}$. So, Eq. 2.2 takes the form of Eq. 2.5

$$V(\vec{s}_{cog_p}) = V_\infty(\vec{s}_{cog_p}) - \frac{1}{2\pi} \sum_{l=1}^{3} \frac{\sigma_l^- - \sigma_l^+}{\sigma_k^- + \sigma_k^+} \sum_{m=1}^{N_{tr}^{(l)}} V(\vec{s}_{cog_m}) \Omega_{(l,m)}(\vec{s}_{cog_p}) \tag{2.5}$$

where $\vec{s}_{cog_m}$ is the centre of gravity point of the mth triangle Δ_m^l on the lth surface S_l. Eq. 2.6 is achieved when Eq. 2.5 is written in the matrix form

$$V = BV + GJ \tag{2.6}$$

where V shows the electrical potential of each nodal point and has a length of N_{tr}, B shows the influence of the points on other points and has a dimension of $N_{tr} \times N_{tr}$, J is the moment matrix with a dimension of $3 \times N_{tr}$. The free space potential matrix having a dimension of $N_{tr} \times 3$ is denoted with G [66, 29]

$$B_{k,l}^{p,q} = \frac{\sigma_l^- - \sigma_l^+}{2\pi(\sigma_k^- - \sigma_k^+)} \sum_{m}^{N_{tr}(l)} \frac{\Omega^{p,m}}{3} \tag{2.7}$$

$$G_k^{p,q} = \frac{(\vec{s}_p - \vec{r}_q)^t}{2\pi(\sigma_k^- + \sigma_k^+)|\vec{s}_p - \vec{r}_q|^3} \tag{2.8}$$

where $\vec{s}_p$ is the $p.th$ nodal point of the surface S_k and $\vec{r}_q$ is the location of the $q.th$

source.

$$V = LJ \tag{2.9}$$

The lead field matrix in Eq. 2.9 is computed once for a realistic head model and used many times in the source localization procedures.

In addition to BEM, FEM [67, 68] and FDM [69, 70] solutions can also be used to solve the forward problem using the realistic head models. Unlike BEM, FEM and FDM solutions do not require the isotropic conductivity of the head model comparments. The volume is represented with small volume elements in which Maxwell's equations are solved locally. As each volume element is characterized by its own conductivity (isotropic or not), any configuration of conductive volume can be modelled. With the FEM, the volume elements are of arbitrary shape, while the volume elements are cubic with the FDM. The technical details of the FDM is given in Chapter 4.2.1. If cubic elements are used, the FEM becomes similar to the finite difference method [71]. The disadvantage of using cubic elements is that all cubes must have the same dimensions. Against this, using cubic elements lead to faster convergence of the forward solution. On the other hand, FEM enable researchers to use realistic head models that are formed by tetrahedral elements which can vary in size. The accuracy of the realistic head model can be ensured by locally refining the tetrahedral meshes [72].

2.3 EEG Source Reconstruction

The location and the strength of the current sources inside the brain that best fits the measurements of the voltage potential at various locations on the scalp, are estimated by solving the inverse problem of EEG. Generally, two types of source models are assumed for the EEG inverse solution;

i) The brain electrical activity can be represented with a few number of dipole sources (Equivalent Current Dipole, ECD [6]) at a given moment in time. These type

of models are named as parametric methods where the number of sources are less than the number of measurements. It was shown that parametric model performs very well in some epileptic spike events [14, 15], and in the description of the early components of the brain-stem auditory evoked potential [73]. The aim is to perform a search in order to find the best dipole positions and orientations. A non-linear minimization of the cost function $||V - L(r_{dip_j})J(r_{dip_j})||$ over all of the parameters (the dipole indice r_{dip_j}, the electrical source activity vector J) is performed to find the best location and dipole moment. *Standard Simplex* search techniques are used to localize the electrical sources in the brain from EEG measured on the scalp [74, 75, 76]. The location, orientation and magnitude of the dipole source are changed iteratively to find the best fit between the measured EEG and those calculated by the source. A time window in which the dipoles are assumed to have fixed position and fixed or varying orientation is considered in the Brain Electrical Source Analysis (BESA) dipole-fit model [77, 78]. Another parametric approach is the beamformers that are used to filter the measured signals in such a way that only those coming from sources of interest are maintained [4]. As a spatio-temporal approach, the multiple-signal Classification algorithm (MUSIC) and its recursively applied and projected version (RAP-MUSIC) is based on subdividing the brain tissue into a *3D* grid and computing the spatial power spectrum with an eigenbased approach for each voxel element [7, 79, 80, 81, 82]. In several studies, in clinical epilepsy, MUSIC [83, 84] and RAP-MUSIC [85, 86] algorithms are used for localizing the sources of the measured scalp data. MUSIC Algorithm is implemented using the below steps;

- Compute the correlation matrix of V
  $C_e = (1/N)VV^T$, where T is the matrix transpose operator.
- Perform eigenvalue decomposition of C_e
  $C_e = [\phi_S \phi_N]\Lambda[\phi_S \phi_N]^T$
  where ϕ_S is signal and ϕ_N is noise eigenvector matrice,
  and $\Lambda : \lambda_1 > \lambda_2 > ... > \lambda_M$ are eigenvalues of C_e.
- Calculate the forward matrix L as defined in Eq.2.7 and its singular value decomposition on each grid point $\{x_j, y_j, z_j\}$ forming the 3-D space.

$H = U_H S_H V_H^T$ (U_H and V_H are left and right eigenvector matrices, S_H contains the singular values of H.)

- $Z(x_i, y_i, z_i) = \frac{1}{\lambda_{min}(U_H^T \phi_N \phi_N^t U_H)}$
  The spikes of Z give the position of dipole sources. Once the location of dipole sources are found, strength of these sources can be found using Eq.2.9.

ii) Several fixed dipole sources covering the whole brain volume are used as a solution space (imaging approach, distributed solution) where the number of sources are more than the number of measurements. This type of non-parametric inverse solutions are investigated as underdetermined linear problems, since the dipole source locations are not estimated. The aim of the non-parametric inverse solutions is to estimate the amplitude and the current orientation of each dipole source in the whole solution space.

Anatomical constraints can be used to reduce the ambiguity of the inverse solution [26]. The forward solution can be computed only for the dipole locations and orientations that are deduced from the anatomical data. The solution of the inverse problem can be selected as the cortical sheet if the origin of the EEG is assumed as the currents flowing in the apical dendrites of cortical pyramidal cells. In this case, the dipole moment would be oriented perpendicularly to the cortical surface because of the columnar organization of the cortex. Thus, the inverse problem reduces to estimating the scalar distribution of dipole activity over the oriented cortical patches (vertices). A linear solution that can consider anatomical constraints derived from MR images and minimizes the expected difference between the estimated and the correct distribution of the brain electrical activity is given in Eq. 2.10 [87]

$$e_M = < ||MV - J||^2 > \tag{2.10}$$

where "$< >$" is the expectation operator. If the noise vector ϵ and the dipole strength vector J in Eq. 2.1 are normally distributed with zero mean and covariance matrices C_e and C_p, then the optimal linear estimator takes the form as in Eq. 2.11.

$$M = C_p L^T (L C_p L^T + C_e)^{-1} \tag{2.11}$$

If the activities (dipole strength) of two neighboring patches of the cortex are correlated and the correlation between any two cortical patches is known, then the inverse solution can be constrained using the prior source covariance matrix (C_p). If the dipoles are assumed a priori to be completely independent and have the same variance then the method reduces exactly to the minimum-norm approach [66]. Source estimation accuracy of the minimum norm approach is limited because of its tendency of favouring the weak and surface sources [88] whereas a weighting matrix which is formed by normalizing the leadfield matrix L, can be used to compansate for this weakness.

The recursively applied weighted norm minimization procedure called FOCUSS (FOCal Underdetermined System Solution) was developed that concentrate the solution in the minimal active regions that are essential for accurately reproducing the measurements [89]. The localization accuracy obtained using FOCUSS was improved in comparison to MNE. However, locations of deeper sources cannot be properly estimated [90]. The brain electrical activity maps that are obtained by the solution of inverse problems, must take into account that neighboring neurons are most likely to be active synchronously and simultaneously. Thus, the inverse solution should consider that neighboring voxels are more likely to be synchronized than voxels that are far from each other. Based on this idea, Pascual-Marqui et al. developed the low resolution electromagnetic tomography (LORETA) method that selects the smoothest of all posible *3D* current distributions [91].

Also based on a similar idea, Grave de Peralta Menendez et al. proposed to incorporate the fact that the strength of the source decreases with distance. A local autoregressive average with homogeneous regression coefficients depending on the distance between solution points is integrated as a constraint to the distributed inverse solution called LAURA (Local Autoregressive Average) [92]. It is known that, some spurious activity was observed when LORETA or LAURA was used for focal source estimation. On the other hand, LORETA was used to obtain the spatial extent of the ictal and interictal generators of the partial epilepsy patients whose lesions were visually identified in MRI [16].

Under the hypothesis that all neurons are equally likely to be active, Pascual-Marqui et al. proposed a linear imaging method which is called as standardized LORETA (sLORETA) approach [93]. The localization results were based on the estimates of the standadization of the minimum norm inverse solution. In the simulation studies, it was shown that under ideal conditions, minimum localization errors were obtained by the use of the standardized current density values of the voxels [94].

Unlike the above distributed inverse solutions, Valdes-Sosa et al. proposed a new type of weighted minimum norm solution that uses spatially varying regularization parameters. A weighted version of laplacian operator is incorporated into the minimum norm solution by using the regularization parameters that vary spatially at each point of the solution grid.

Accurate estimation of the brain activity from the scalp measurements requires the usage of prior information such as anatomical, functional or mathematical constraints. The data driven relevance of different priors is investigated through Bayesian model inversion [95] and different sets of constraints/priors can be examined using Bayesian model comparison. Friston et. al, developed an approach in which the inverse solution is adjusted to be a parametric or distributed type depending to the measured data using multiple sparse priors [96].

3. Subtopographic EEG decomposition in Neuroimaging

3.1 Spatio-temporal modeling of EEG

Precise localization of electrical events in the brain, based on the EEG data recorded from the scalp, has been one of the main challenges of functional brain imaging. Several current density estimation techniques for identifying the electrical sources generating the brain potentials are developed for the so-called neuroelectromagnetic inverse problem in the last three decades.

The sources underlying the EEG (or ERP), which are rather distributed in the brain and nonstationary in time, also motivate the researchers to invent additional simplifications and analyses on the multichannel data before they apply source localizaton. Several studies aimed for isolating stationary frequency components in temporal windows, using time frequency analysis, and then applying source localization techniques to the scalp maps generated by these time frequency components. Source localization of epileptic discharges is performed after wavelet prefiltering to isolate the spiky waveforms from the background EEG [8]. The source localization of ERP is performed by first applying the time-frequency analysis and then using MUSIC source localiztion algorithm on these time-frequency components [9].

Gonzalez Andino et al. proposed an eigen-based method to identify the location of each underlying source in the time−frequency plane that generates a certain topographic distribution [97]. Unlike the previous time-frequency studies that use single channel data, Koenig et al. [10] perform time-frequency optimization on mutichannel data with the wavelet coefficients having minimum energy and maximum spatial smoothness distributions. A more general and unique space/frequency/time decomposition in terms of so-called atoms are proposed by Miwakaichi et al. [12], which overcomes the limitation of introducing artificial assumptions as indepence in ICA or uncorrelatedness in PCA approaches [11]. In all these studies, the problem of identi-

fying the individul EEG (ERP) components are treated by proposing a decomposition method that involves the time, frequency, channel, or their various combinations. Another common feature observed is that the concept of frequency is always associated with, and defined in, temporal domain. In Wang et al., the spatial ERP maps are enhanced by using first, a projection method that transforms the scalp potentials defined on a *3D* surface to a *2D* plane, and then applying a *2D* multiresolution decomposition [13]. This is the first approach that attempts to simplify the scalp topography by decomposing it into simpler maps using a spatial multiresolution.

A scalp topographic map for an EEG/ERP may be a superposition of several simpler subtopographic maps, each resulting from an individual electrical source located at a certain depth as a focal or extended activity. Furthermore, this source may have a temporal characteristics as an oscillation or a rhythm that extends in a certain time window, which has been a basis of assumption for the time-frequency analysis methods.

3.2 Spatial decomposition using Radial Basis Functions

2D spatial basis functions are used as kernel functions in order to identify the subtopographic maps from the complex topographies. For this purpose, Radial Basis Functions (RBFs) are used to form the subtopographic structures. Non-linear optimization is used to estimate the parameters of several RBFs under the constraint that the summation of the subtopographic maps converge to the input topography.

3.2.1 Estimation of Radial Basis Function Parameters

An RBF is a real-valued function whose value depends only on the distance from the origin, so that $\theta(x) = \theta(||x||)$; or alternatively on the distance from some other point c, called a center, so that $\theta(x, c) = \theta(||x - c||)$. Any function θ that satisfies the property $\theta(x) = \theta(||x||)$ is a radial function.

Two different RBF, a gaussian as in Eq. 3.1 and a morlet function as in Eq. 3.2 kernels are selected to approximate the input image. RBF is fitted to the EEG *2D* topography by solving Eq. 3.4 using nonlinear least squares optimization [98, 99]. The mesh images of *2D* gaussian and morlet RBFs are seen in Fig. 3.1.

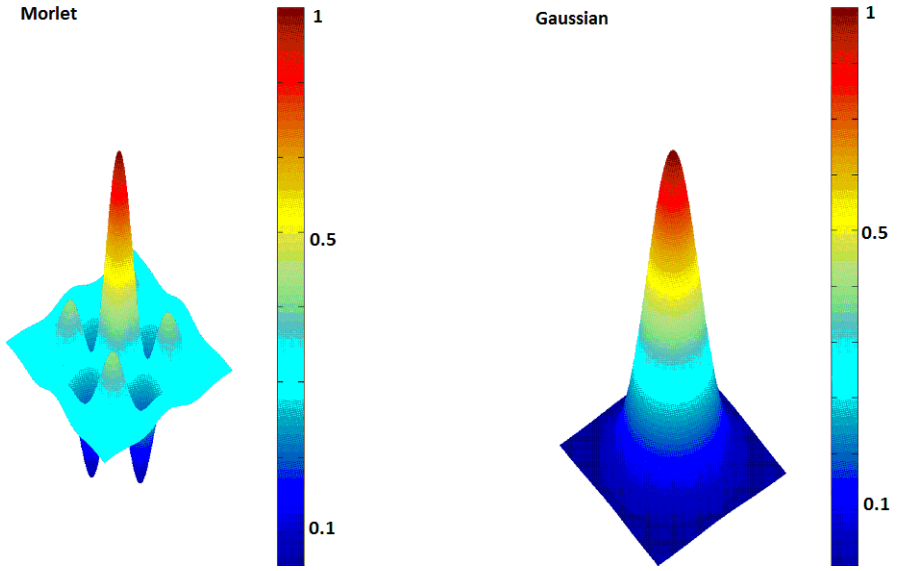

Figure 3.1 Mesh images of *2D* RBF Morlet kernel and Gaussian kernel, respectively.

$$V_t(x,y) = \sum_{i=1}^{Nf} a_i e^{-f} \tag{3.1}$$

$$V_t(x,y) = \sum_{i=1}^{Nf} a_i e^{-f} \cos(k_i(x - x_{c_i})) \cos(l_i(y - y_{c_i})) \tag{3.2}$$

$$f = \frac{(x - x_{c_i})^2}{\sigma_{x_{c_i}}^2} + \frac{(y - y_{c_i})^2}{\sigma_{y_{c_i}}^2} \tag{3.3}$$

where V_t is the approximated *2D* scalp topography for an instance of time, x_{c_i} and y_{c_i} are coordinates of the center points, N_f is the number of RBFs and a_i is the weighting coefficient of RBF.

The nonlinear least square optimization tries to adjust the parameters $\alpha = \{ a_i, y_{c_i}, x_{c_i}, k_i, l_i, \sigma_{x_{c_i}}, \sigma_{y_{c_i}} \}$ of the kernel function V_t by minimizing the cost function

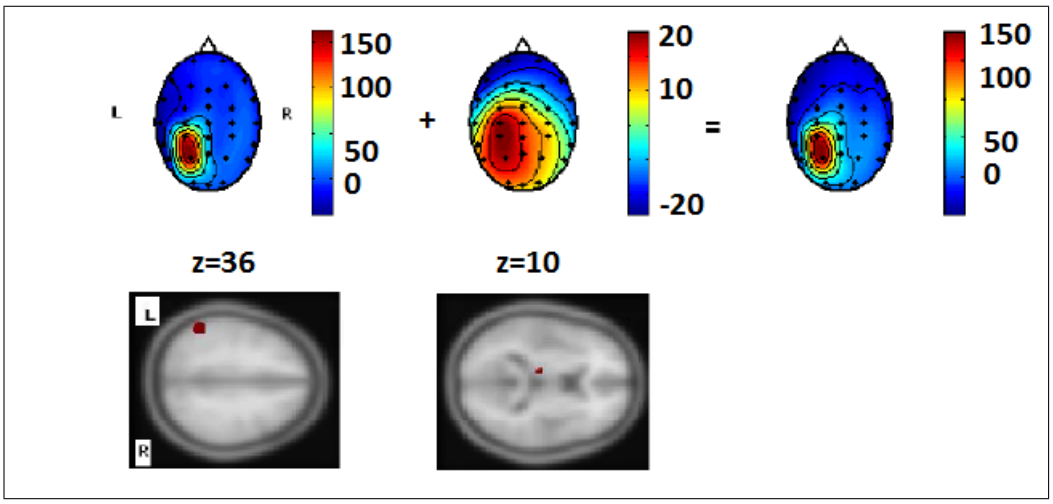

Figure 3.2 *2D* topography of simulation data for the a) superficial source and b) deeper source, c) superimposition of these two subtopographies, d) location of the superficial and deeper source, respectively.

in Eq. 3.4

$$min||V_o(x,y) - V_t(x,y)|| \tag{3.4}$$

where V_o is the raw *2D* scalp topography [100].

$$F(\alpha) = \begin{bmatrix} V_{o_1}(x,y) - V_{t_1}(x,y) \\ V_{o_2}(x,y) - V_{t_2}(x,y) \\ \vdots \\ V_{o_{nc}}(x,y) - V_{t_{nc}}(x,y) \end{bmatrix} \tag{3.5}$$

The Levenberg-Marquardt method uses a search direction that is a solution of the linear set of equations in Eq.3.6

$$(J(\alpha_t)^T J(\alpha_t) + \lambda_t \, diag(J(\alpha_t)^T J(\alpha_t)))d_t = -J(\alpha_t)^T F(\alpha_t) \tag{3.6}$$

where the scalar λ controls both the magnitude and direction of d_t and J is the jacobian matrix of multichannel cost function F. α is updated with the direction and the optimization procedure continues until the desired error level is achieved. After the cost function minimization procedure, the estimated parameters (α) are used to form subtopographies.

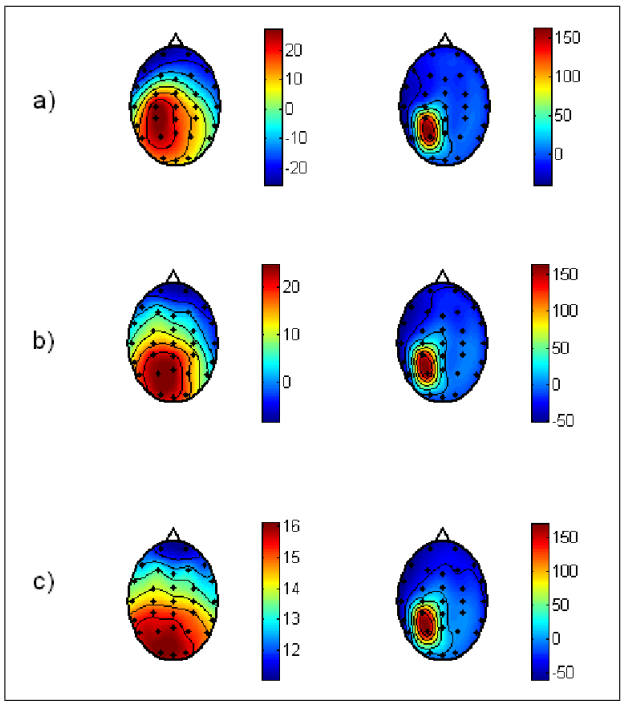

Figure 3.3 a) Original raw subtoporaphies. b) Approximation and detail subtopographies decomposed using Morlet RBF and c) Gaussian RBF kernels.

3.2.2 Application to simulated data

In order to validate the RBF decomposition method, a simulated multichannel EEG data is generated using BEM. Two stationary radial point sources are assumed; one being superficial while the other being deeper in the brain. Forward problem is solved for these point sources using BEM over the predefined head model given in Fig. 3.8 and the topograhies are shown in Fig. 3.2.

The inverse problem is solved using MUSIC for the total topographic activity. The inverse solution could not localize the deeper source. After the RBF decomposition, two suptopographic maps are obtained and their superimposition yielded the original EEG topography. Results of the RBF decomposition method for two kernel functions are shown in Fig. 3.3. When these decomposed topographies are individually localized, it can be observed that the predefined sources can be easily discriminated as shown in Fig. 3.4. Superficial source is localized from the approximation output while the deeper source is estimated from the detail output.

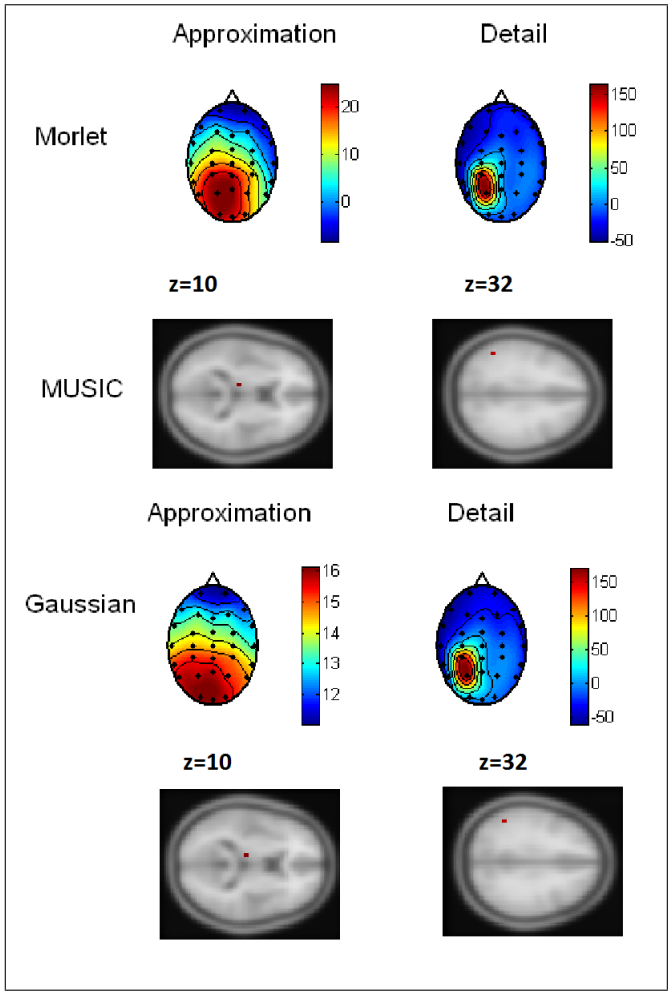

Figure 3.4 *2D* topographies of decomposed subtopographies based on Morlet and Gaussian RBF. Source localization of the corresponding topographies using MUSIC algorithm.

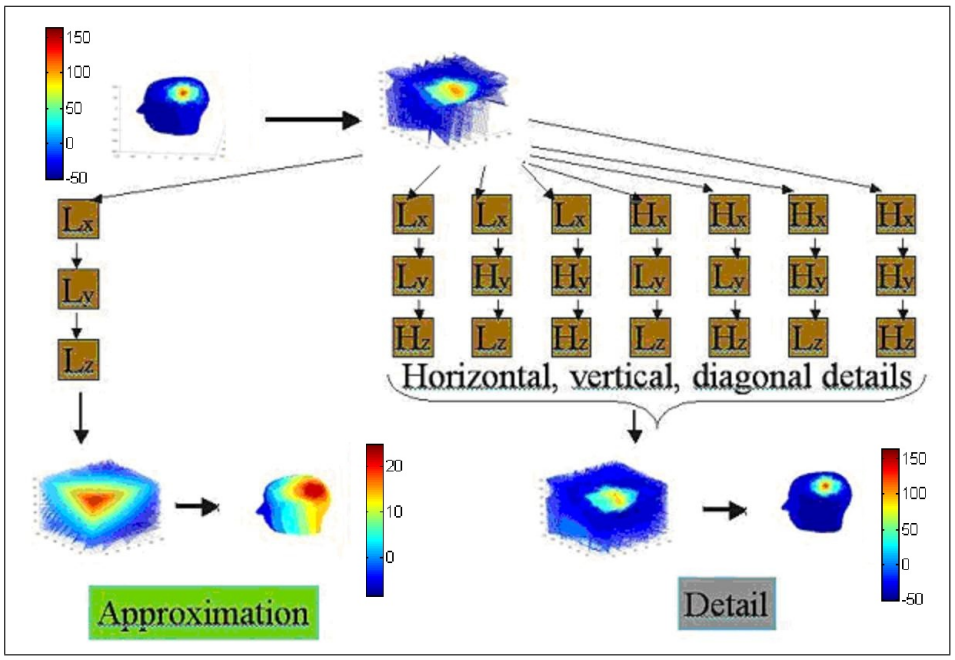

Figure 3.5 *3D* topography is converted to a *3D* regular volumetric grid. By using *1D* DWTs, at each stage volumetric grid with raw data is decomposed into two sets called approximation and detail. Finally, the original topograhies are regenerated from these volumetric maps.

3.3 Spatial Wavelet decomposition of the topographies

The subtopographic maps arising from sources located at certain depths with different extention of activities generally fall into different spatial frequency bands on the scalp. Therefore, a spatial frequency decomposition of a scalp potential distribution yields these subtopographic maps, whose source localizations will lead us to their electrical sources in the brain. It is essential to perform this spatial frequency decomposition on a realistic scalp surface without any distortion. To achieve this purpose, we propose a method that involves a realistic scalp model on which a *3D* wavelet transform is performed, and the subtopographic maps obtained are source localized using inverse modeling.

3.3.1 Continuous Wavelet decomposition

The wavelet transform of a continuous signal $f(t)$ can be defined as Eq. 3.7

$$CWT_f(a,b) = \left\langle f(t), |a|^{(-1/2)} h^*(\frac{t-b}{a}) \right\rangle = |a|^{(-1/2)} \int f(t) h^*(\frac{t-b}{a}) dt \tag{3.7}$$

where "*" represents the complex conjugation and where "$\langle\rangle$" represents the inner product. In the wavelet transform the sampling in frequency is logarithmic which enables one to analyze higher frequencies in shorter windows and lower frequencies in longer windows in time.

The wavelet functions $h_{a,b}(t)$ are generated from a single function $h(t)$ by the operation of dilations and translations as in Eq. 3.8

$$h_{a,b}(t) = |a|^{(-1/2)} h(\frac{t-b}{a}) \quad a, b \in \underline{R}, a \neq 0. \tag{3.8}$$

3.3.2 Discrete Wavelet decomposition of spatial topographies

Given a signal s of length N, the first step of Discrete Wavelet Transform (DWT) produces two sets of coefficients: approximation, and detail coefficients. These vectors are obtained by convolving the signal with the low-pass filter for approximation (h), and with the high-pass filter for detail (g), followed by dyadic decimation (downsampling) [101]. This decomposition splits data at level j into two components: the approximation at level $j+1$, and the detail at level $j+1$ [102, 103, 104].

The approximation A_u^{j+1} at level $j+1$ and the detail D_u^{j+1} at level $j+1$ are calculated by Eq. 3.9 and Eq. 3.10, respectively.

$$A_u^{j+1} = \sum_x h(x-2u) A_x^j \tag{3.9}$$

$$D_u^{j+1} = \sum_x g(x-2u) A_x^j \tag{3.10}$$

For images, the algorithm is similar to the *1D* case where the two dimensional (*2D*) wavelets and scaling functions are obtained by the tensor product of respective *1D* functions. *2D* DWT leads to a decomposition at level j into four components: the approximation at level j+1, and the details in three orientations (horizontal, vertical, and diagonal).

The approximation $A_{u,v}^{j+1}$ at level $j+1$ is calculated by Eq. 3.11,

$$A_{u,v}^{j+1} = \sum_x \sum_y h(x-2u)h(y-2v)A_{x,y}^{j} \tag{3.11}$$

horizontal detail component is denoted with $D_{u,v}^{j+1}(1)$ and computed in Eq. 3.12,

$$D_{u,v}^{j+1}(1) = \sum_x \sum_y h(x-2u)g(y-2v)A_{x,y}^{j} \tag{3.12}$$

vertical detail component is denoted with $D_{u,v}^{j+1}(2)$ and computed in Eq. 3.13,

$$D_{u,v}^{j+1}(2) = \sum_x \sum_y g(x-2u)h(y-2v)A_{x,y}^{j} \tag{3.13}$$

and diagonal detail component is denoted with $D_{u,v}^{j+1}(3)$ and computed in Eq. 3.14,

$$D_{u,v}^{j+1}(3) = \sum_x \sum_y g(x-2u)g(y-2v)A_{x,y}^{j} \tag{3.14}$$

$$D_{u,v}^{k} = \sum_{i=1}^{3} D_{u,v}^{k}(i) \qquad\qquad 1 \le k \le j \tag{3.15}$$

finally, the vertical, horizontal and diagonal details are summed to produce one detail component for each level as in Eq. 3.15.

Similarly, to perform *3D* wavelet decomposition, *1D* DWT is applied on three directions on the *3D* volume data, as illustrated in Fig. 3.5. That leads to eight components from level j to j+1, one being the low pass filtered data, and seven others as the various combinations of low and high pass filtered data, in all three directions [105, 106].

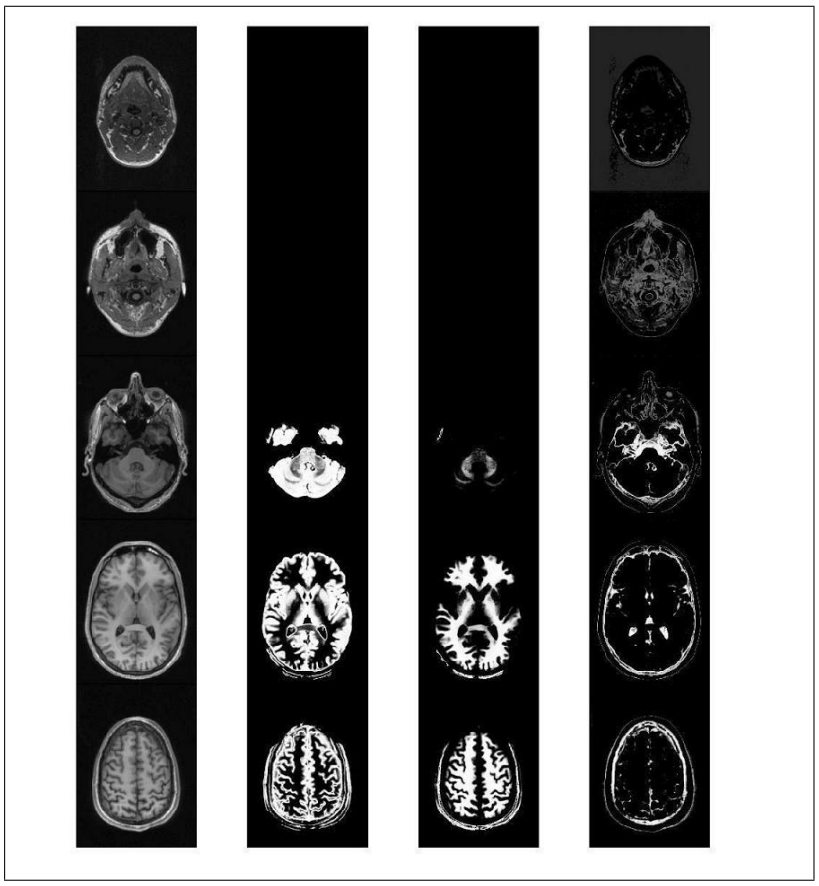

Figure 3.6 Axial slices of the segmented raw MRI data and the gray matter, white matter and CSF images

3.3.3 Application to simulated data

EEG forward solution is computed to simulate EEG data. The human head is modeled as three homogeneous isotropic conductor layers; the outermost surface being the boundary for the scalp, the intermediate for the skull and the innermost being for the brain. Statistical Parameter Mapping software 2005 release (SPM05) [107] which is developed by Wellcome Institute is used for *3D* segmentation of the brain, skull and scalp (output of the segmentation is shown in Fig. 3.6). After segmentation, the surfaces are triangulated in order to generate the realistic head model. Surfaces of the brain, skull and scalp are tesselated with 1000, 1000 and 2000 triangles respectively as shown in Fig. 3.7. Scalp electrodes (30) are registered to the head model, by spline interpolation using the T1 weighted MR data and the inion and nasion coordinates based on $10-20$ electrode placement system. The registered locations of the electrodes are

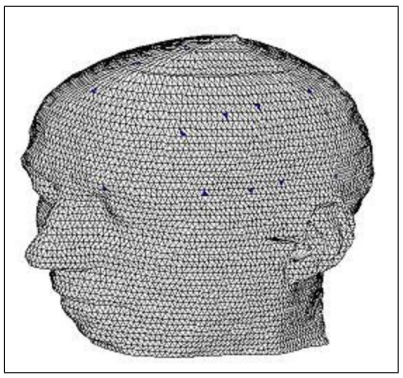

Figure 3.7 Realistic scalp model developed from T1 weighted human brain MRI data containing 16188 triangles and 7800 vertices.

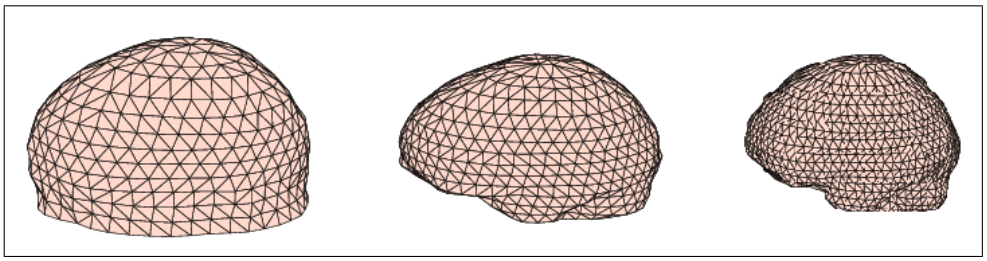

Figure 3.8 Scalp, skull and CSF surfaces are tessellated with 1000,1000,2000 surfaces respectively.

shown with blue triangles in Fig. 3.7. A simulated multichannel ERP data is generated by using COG approximation of the BEM. Two stationary radial point sources are assumed, one being superficial, while the other being deeper in the brain. Forward problem is solved for these point sources using BEM over the predefined head model given in Fig. 3.8. The amplitude changes of the two point sources were sinusoidal with 128 data points, and they were temporally correlated.

3.3.4 Source Reconstruction of Simulated Data

The inverse problem is solved using the total topographic activity. Although, temporally uncorrelated sources can be easily discriminated by the MUSIC algorithm, the source positions, in this case, are not clearly separated because of the temporal correlation of individual sources. MUSIC estimated the location of the superficial source from the total topography, which is a missing solution. Deeper source could not be localized by these inverse solutions. By the spatial wavelet decomposition prior

to source localization, subtopographic maps, which originate from individual sources, can be identified, whose superimposition yields the original ERP topography. In our case, seven octave spatial wavelet decomposition is applied to the topography serie of total activity and the original topography serie is divided into two sets, as seen in Fig. 3.9. One of the topographic map series denotes the approximation outputs, which is the low-pass filtered in all directions, and the other series shows the detail output, which is the remaining part of the original topography series. When these topographic map series are individually localized, it can be observed that the predefined sources can be easily discriminated, as shown in Fig. 3.9. Superficial source is localized from the approximation output while the deeper source is estimated from the detail output. Although it could be decomposed into any number of subtopographies, the original simulated map is divided into two, each of which corresponds to one individual distinct source. Due to the large number of grid points, the spatial wavelet decomposition requires a high computational complexity and memory usage. An efficient algorithm is designed to perform a spatial wavelet decomposition on *3D* realistic head surface without any loss of information.

3.4 Spatio-Temporal Wavelet Decomposition on Realistic Head Model

Spatio-temporal wavelet transform can be performed in two steps: i) a temporal wavelet decomposition of the multichannel data to identify the individual time-frequency components in terms of wavelet coefficients, ii) a spatial wavelet decomposition of a topographic scalp map of each individual wavelet coefficient into subtopographic maps corresponding to different spatial frequency bands. Therefore, a spatio-temporal decomposition of multichannel ERP data involves a multidimensional wavelet transform.

As an alternative way, we treat the scalp map of an individual temporal wavelet coefficient as a *3D* topographic surface on a realistic head model whose intensity is color

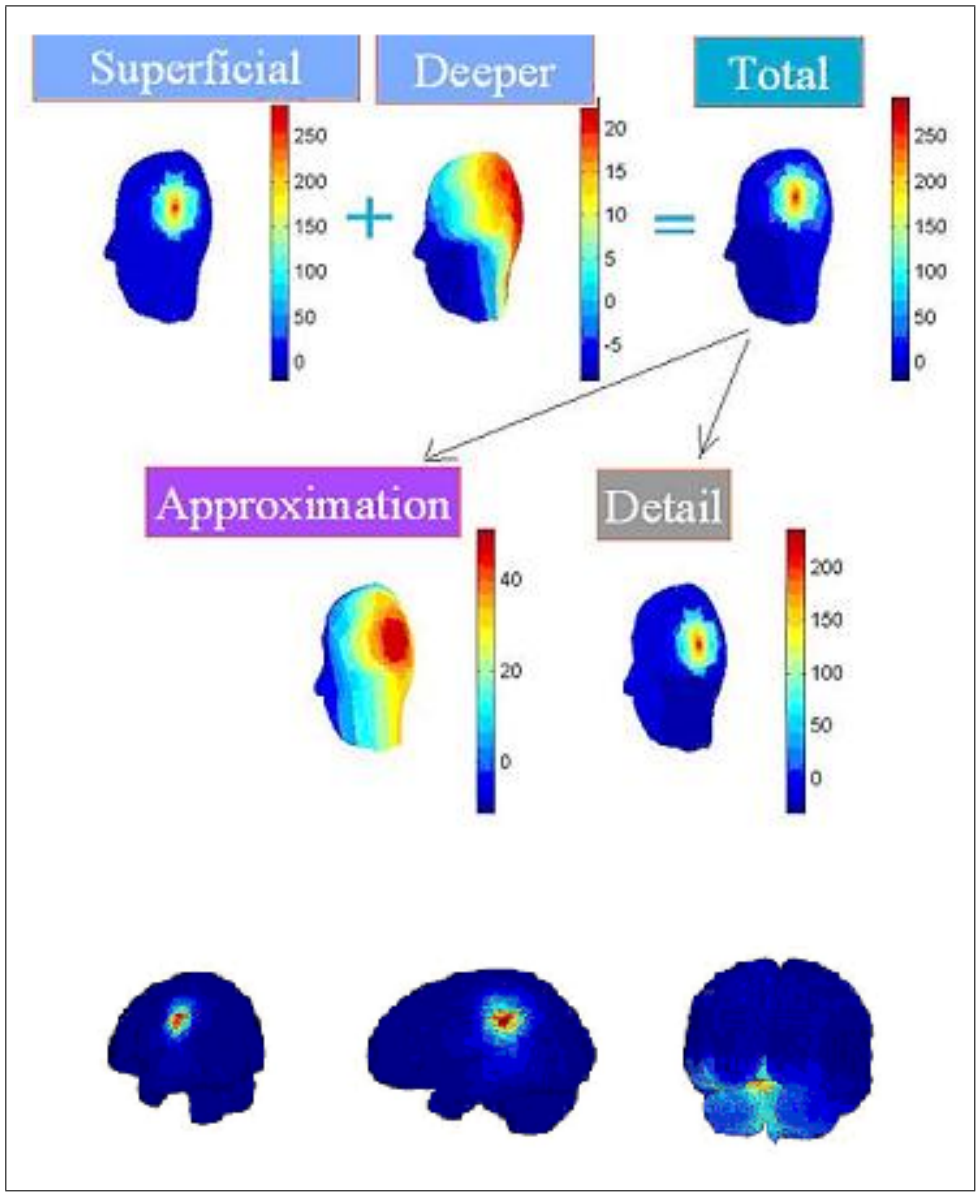

Figure 3.9 Topography of superficial source, deeper source and total activity at the time instant of 32. Fourth topography is the approximation and the fifth topography is the detail output. Inverse solutions of the total, approximated and detail topographies with MUSIC, respectively.

coded with the amplitude of EEG. In order to perform a spatial wavelet transform on this hypersurface, a *3D* interpolation and flattening with contortion are performed which physically corresponds to cutting this scalp surface and spreading it onto a *2D* plane. This transformation does not presume any spherical model for the scalp surface whose projection on a *2D* may incur possible distortions of the EEG data [108].

3.4.1 Flattening with contortion

The path between the PCz electrode as a reference point and any other electrode location on the scalp is interpolated with a *3D* spline algorithm before the curve is contorted on a plane as shown in Fig. 3.10 a,b. Then the entire region is resampled as a uniform rectangular grid as shown in Fig. 3.10 c. The steps of the algorithm can be summariazed below;

- (i) The PCz electrode location is selected as the reference point of the *3D* realistic model and denoted as $p(x_0, y_0, z_0)$. New coordinate of this electrode is going to be the centre point $(0, 0)$ of the new *2D* model.
- (ii) $\forall\ p(x_i, y_i, z_i)$, $i \in \{1, 2, ...N_c\}$ The shortest curve P_i between $p(x_0, y_0, z_0)$ and $p(x_i, y_i, z_i)$ that lays on the scalp surface is computed and Eq.3.16 is used to compute the new location on *2D* model.
- (iii) $q(x_i, y_i)$ is the transformed coordinate of the $p(x_i, y_i, z_i)$ in the new *2D* domain.

$$q(x_i, y_i) = \frac{p(x_i, y_i) - p(x_0, y_0)}{||p(x_i, y_i) - p(x_0, y_0)||} \times length(P_i) \tag{3.16}$$

- (iv) A uniform higher resolution *2D* regridding and a corresponding nearest neighbourhood interpolation are performed using the $q(x_i, y_i)$, V_i duple to fill in the potential values on the new grid.

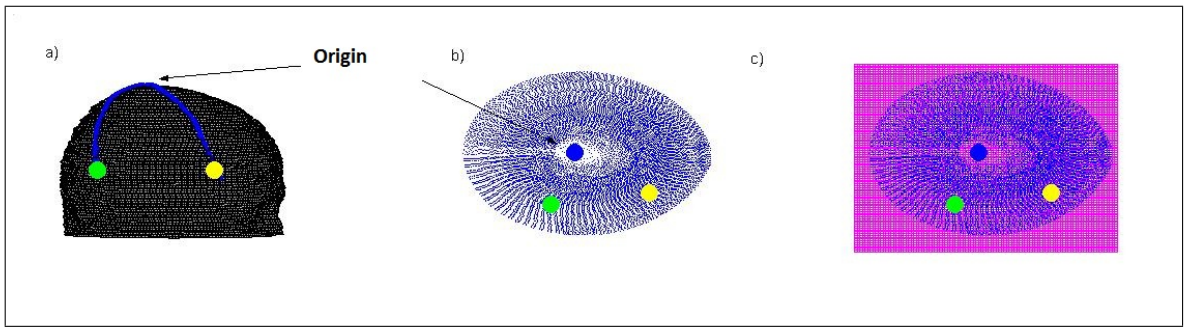

Figure 3.10 a) 3 electrode locations are symbolized with blue circle (CPz), yellow circle (F8) and green circle (P8). CPz point is selected as the reference and the paths between origin and the other 2 electrodes are denoted with blue color. b) The new locations of these 3 points are plotted on the *2D* domain. c) Regridding is applied to the *2D* space.

Finally, a *2D* wavelet transform is applied on the plane and the subimages obtained are remapped to the original scalp surface. This way, a spatial wavelet decomposition is accomplished on a realistic scalp model without introducing any possible distortion due to a geometric projection.

3.4.2 Implementation of the algorithm to simulated data

In order to demonstrate the effect of preprocessing the multichannel ERP with the spatio-temporal wavelet transform, 30 channel ERP data is simulated using the sources as shown in Fig. 3.13. Six point sources with the same spatial extension of $2 \times 2 \times 2$ mm are used and scalp potentials are generated using BEM. Two of the sources, one deep, one superficial (Brodmann area 44 Precentral Gyrus Frontal Lobe, Brodmann area 8 Middle Frontal Gyrus Frontal Lobe) oscillate with 2 Hz temporal frequency in 129-192 ms time window. The other four sources overlap in the same time window (321-384 ms). Two of these are superficial with different frequencies i.e. 2 (delta) and 11 Hz (alpha) (Brodmann area 4 Precentral Gyrus Frontal Lobe, Brodmann area 39 Inferior Parietal Lobule Parietal Lobe), while the remaining two are deep (Brodmann area 29 Superior Temporal Gyrus Temporal Lobe, Brodmann area 39 Superior Temporal Gyrus Temporal Lobe) and differ in frequency in the same way as summarized in Fig.3.13. The sampling rate is 512 Hz. Finally, white noise with 10 db SNR is added to the simulated ERP data. Spatio-temporal analysis start with

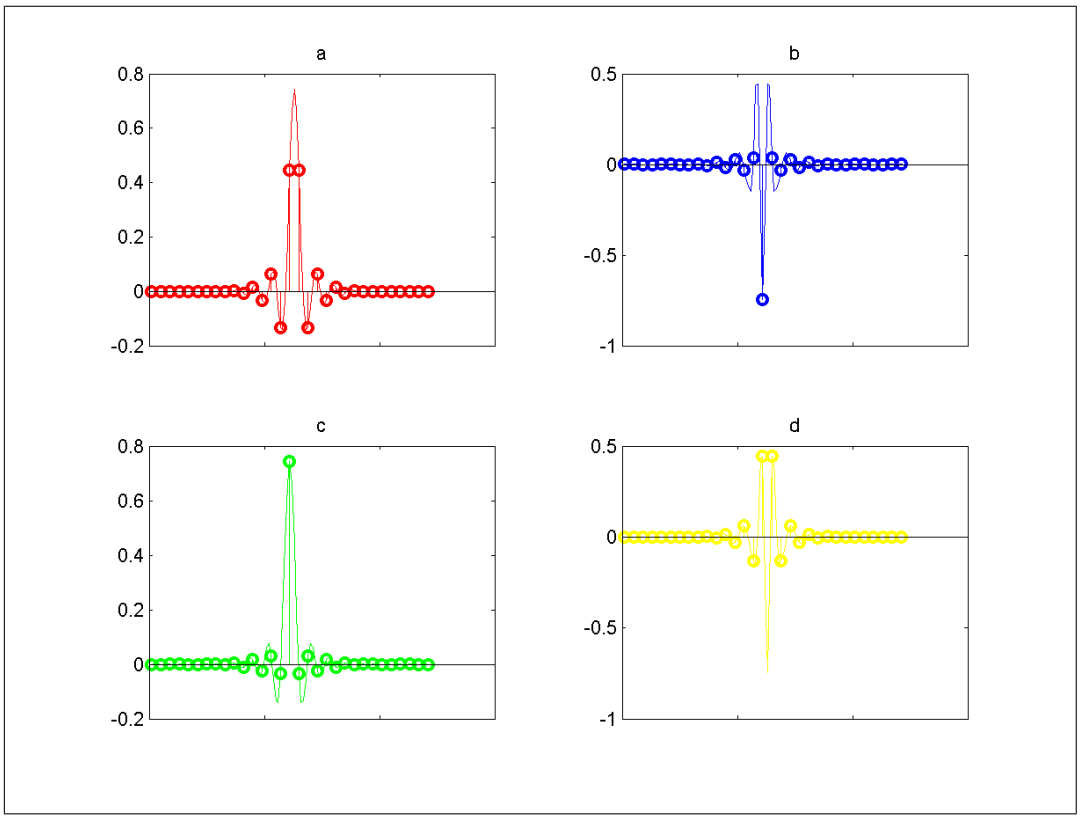

Figure 3.11 Discrete Meyer wavelet, a)The decomposition low-pass filter, b)decomposition high-pass filter, c)reconstruction low-pass filter, d)reconstruction high-pass filter respectively.

decomposing ERP data into time-frequency components using *1D* wavelet transform. 6 octave *1D* wavelet decomposition ("bior 3.9") is applied to the simulated ERP data. 30×512 distinct coefficients each of which represents unique frequency-time-channel information are generated by the *1D* decomposition of the multichannel simulated ERP data.

After temporal decomposition, amplitudes of the three wavelet coefficients significantly differ from the others as stated in Fig. 3.14. These components fall into Delta 3, Delta 6 and Alpha 11 bands, respectively. Discrete Meyer wavelet as shown in Fig. 3.11 is used for spatial decomposition. Three detail components are summed to form one detail component for each octave, so k octave decomposition yields one approximation and k detail components.

The 3-D topographies are decomposed with spatial wavelet transform with ("Meyer") wavelet into 5 spatial octaves. Each decomposition yields 6 subtopographies

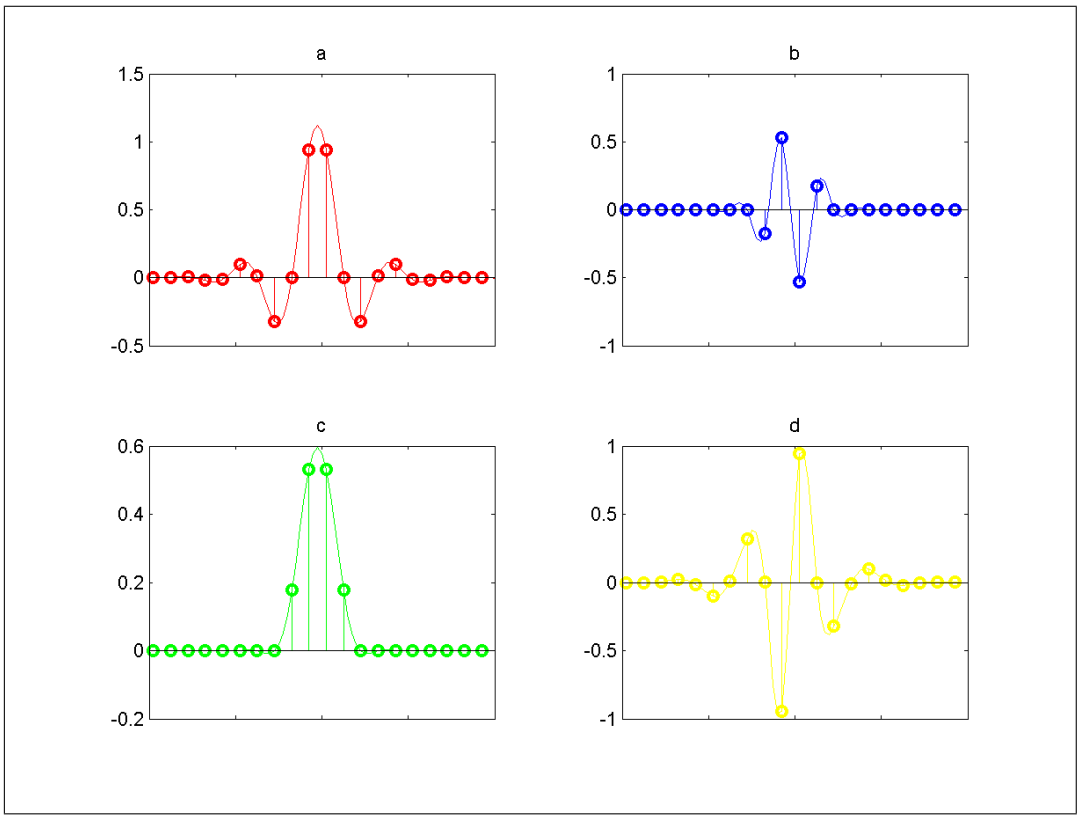

Figure 3.12 Biorthogonal wavelet. a) The decomposition low-pass filter (h), b) decomposition high-pass filter (g), c) reconstruction low-pass filter, d) reconstruction high-pass filter respectively.

differing from each other by their spatial frequency extent. The first subtopographic map is the approximation while the other 5 are summed to form one map and called as the detail. For a comparative demonstration of the difference, source localization algorithm is applied both to temporally decomposed maps and to their spatially decomposed approximations and details. After the temporal wavelet decomposition is performed on the simulated multichannel EEG data, specific coefficients exhibit higher values than the others. When the coefficients are analyzed through their amplitudes across all channels, the temporal decomposition reveals three time/frequency components, namely D3 (129-192 ms), $D6$ (321-352 ms) and $A11$ (321-352 ms). Once the topographic maps corresponding to these components are source localized, the true locations cannot be determined accurately. In the analysis of the topographic map corresponding to $D3$, MUSIC algorithm estimates the location of activity close to Brodmann Area ($BA8$) (Middle Frontal Gyrus in Frontal Lobe) which is shown in Fig. 3.15(a) with a significant maximum indicated with red color. This solution yields a spatially approximated single location for two separate sources. However, it fails to

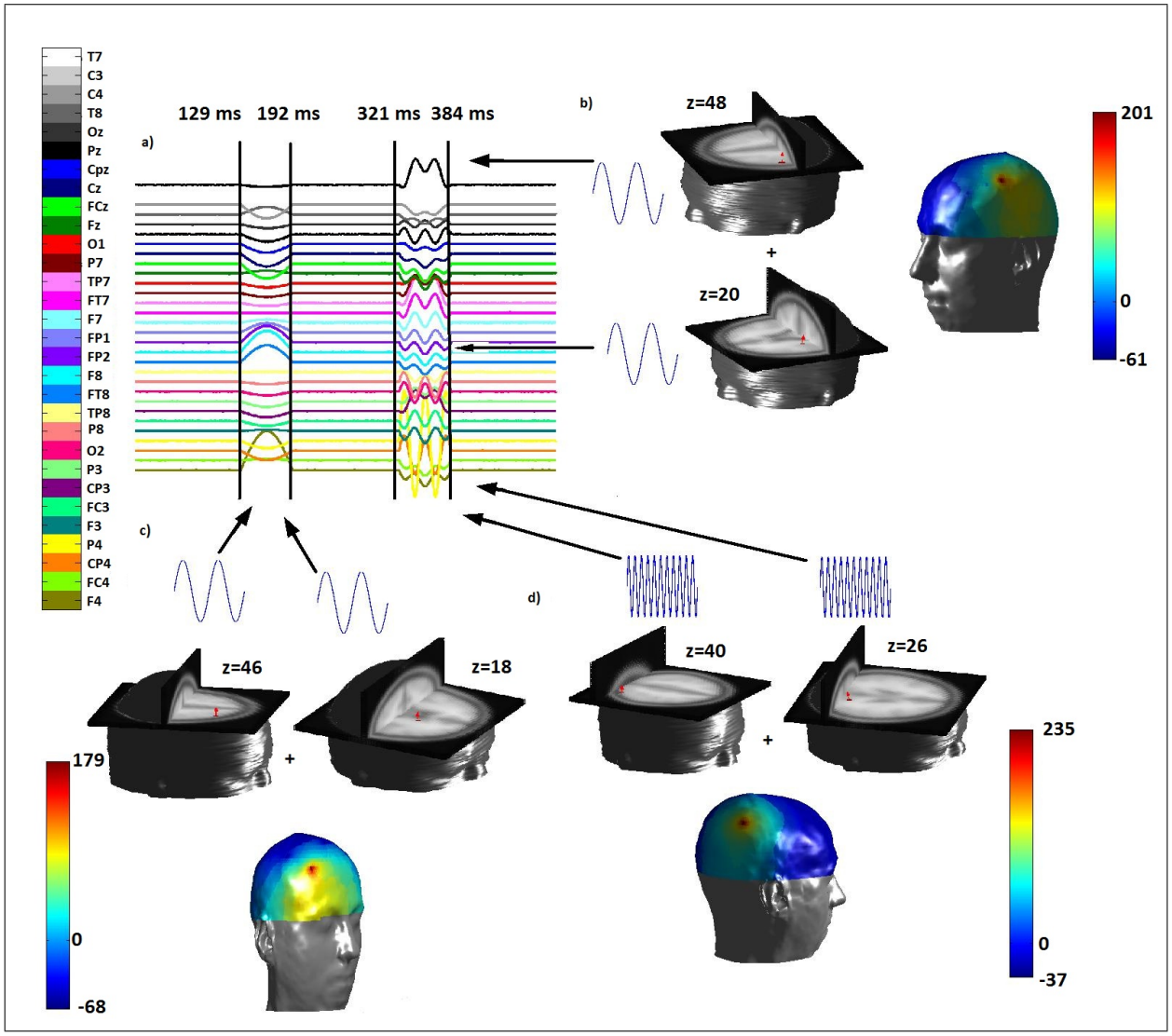

Figure 3.13 Source configuration of the simulated ERP data a) 30 channel ERP data having a sampling rate of 512 Hz with 512 ms second duration. b) Two dipole sources with the same moment values, different spatial locations oscillating at the Delta frequency band in the 321-384 ms time window, and scalp topography of the instantaneous ERP produced by these sources. c) Two dipole sources with the same moment values, different spatial locations oscillating at the Delta frequency band in the 129-192 ms time window, and scalp topography of the instantaneous ERP produced by these sources. d)Two dipole sources with the same moment values, different spatial locations oscillating at the Alpha frequency band in the 321-352 ms time window, and scalp topography of the instantaneous ERP produced by these sources.

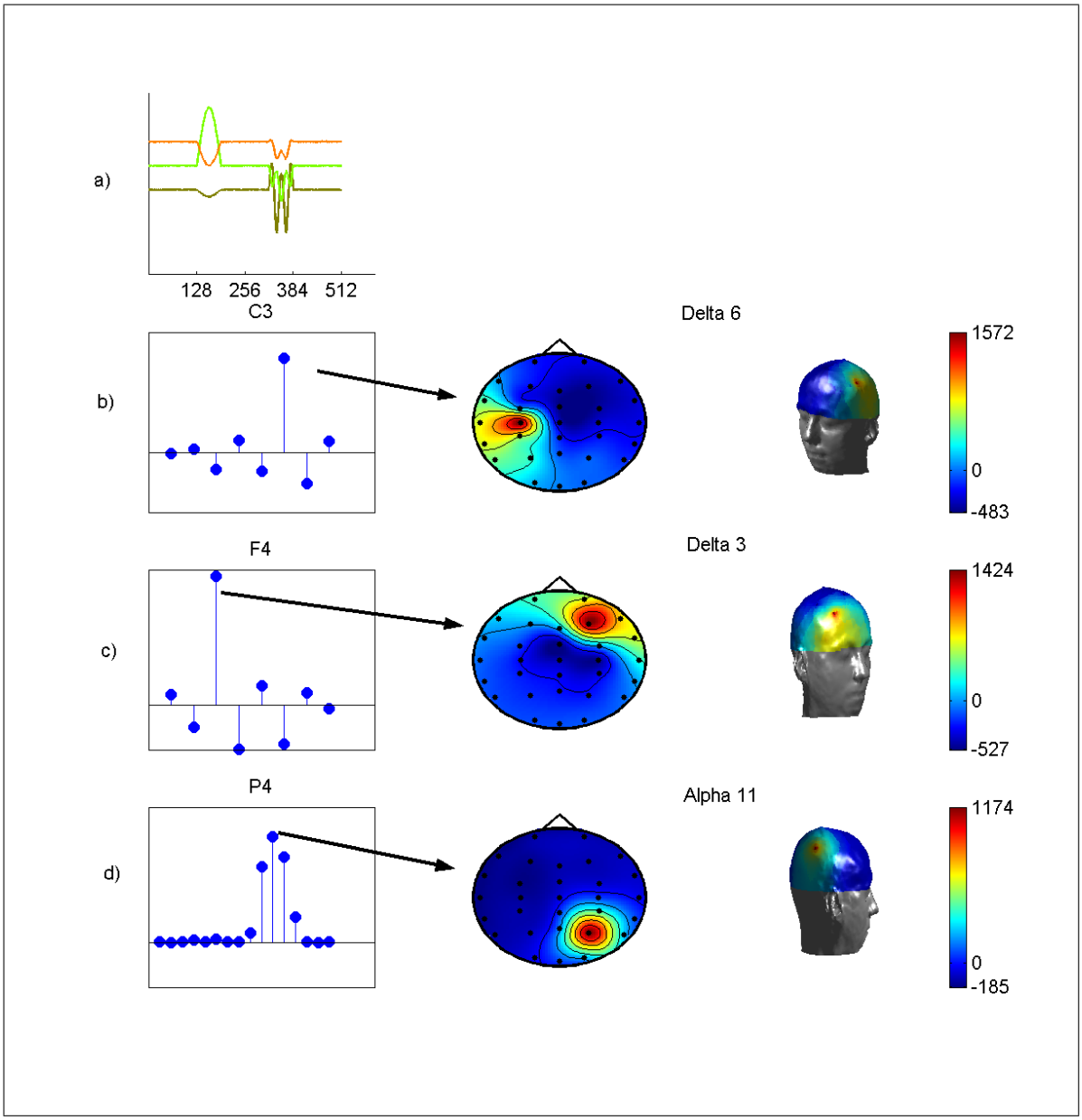

Figure 3.14 Topographies of temporal wavelet coefficients. a) Simulated data for 3 channels, C3, F4 and P4. b)After temporal decomposition process, the maximum wavelet coefficient was found as Delta 6 which was in the 321-384 ms time window of the C3 channel. *2D* and *3D* topographies of Delta 6 coefficient were plotted respectively. c) The second biggest coefficient was Delta 3, which occured in the 129-192 ms time window of the F4 channel. Corresponding *2D* and *3D* topographies of Delta 3 coefficient were plotted respectively. d) Alpha 11 coefficient of P4 channel in 321-352 ms time window was the third highest value. *2D* and *3D* topographies of Alpha 11 coefficient were plotted respectively.

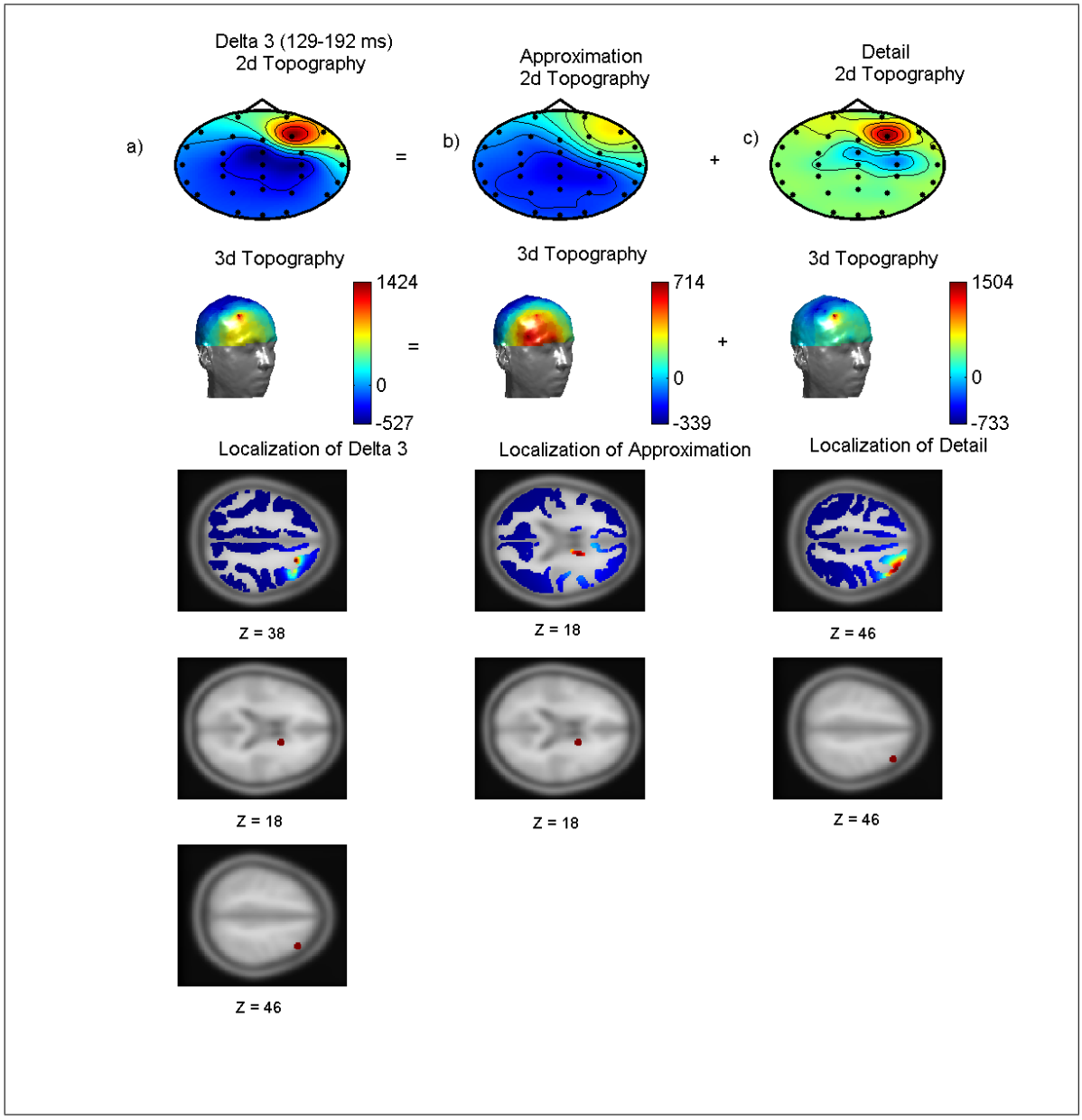

Figure 3.15 Subtopographies of spatio-temporal wavelet coefficients and their source localization. a)*2D* and *3D* topographies of the Delta 3 coefficient (129-192 ms) and localization results obtained by MUSIC algorithm. The original locations are shown in the 4th and 5th row. b) *2D* and *3D* subtopographies of approximation output produced by spatial decomposition and localization results of the associated topographies. Correct location of the dipole source is shown in the 4th row. c)*2D* and *3D* subtopographies of the detail output produced by spatial decomposition and localization results for the detail topographies. Correct location of the dipole source is shown in the 4th row.

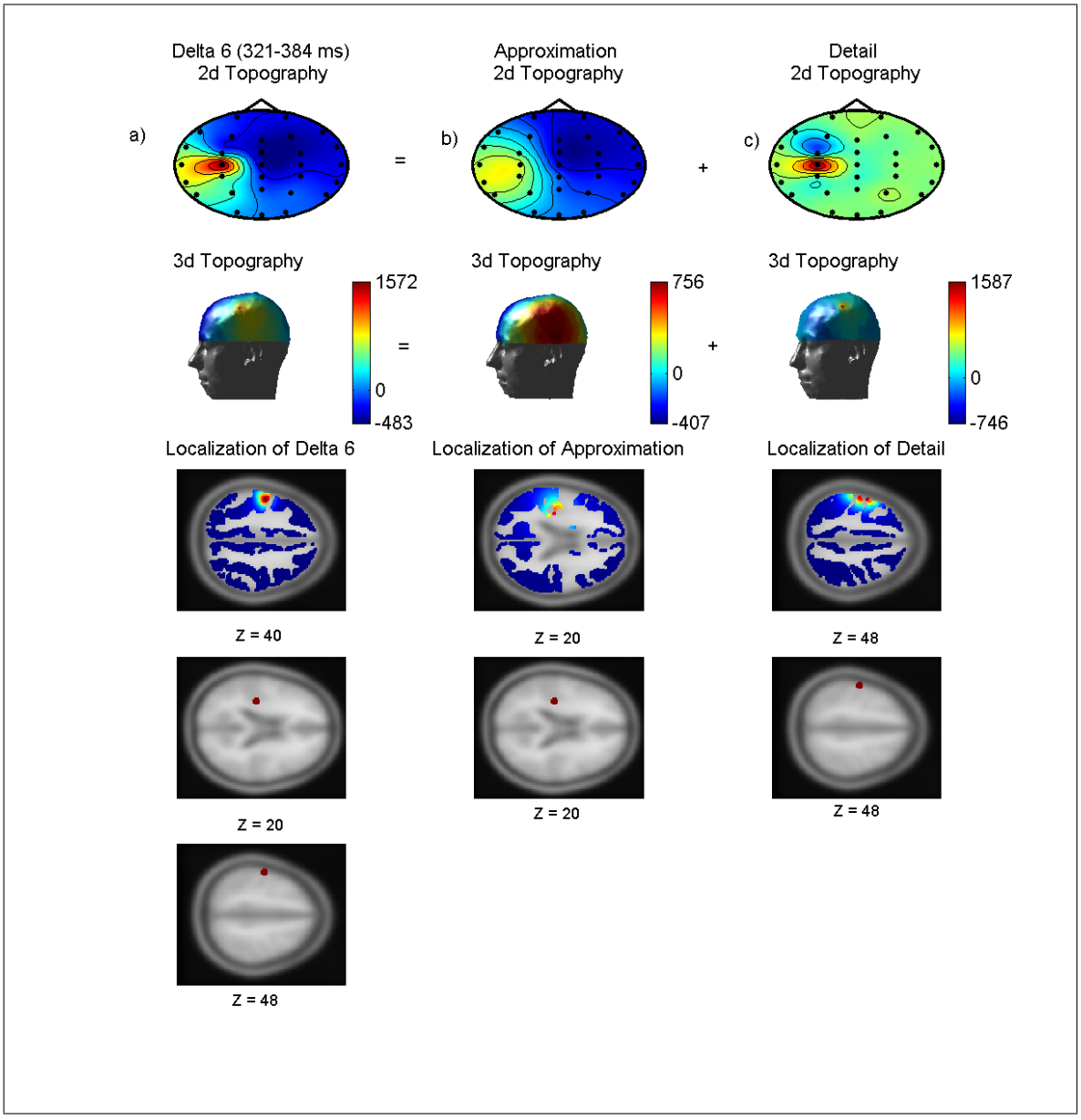

Figure 3.16 Subtopographies of spatio-temporal wavelet coefficients and their source localization. a)2-D and 3-D topographies of the Delta 6 coefficient (321-384 ms) and localization results obtained by MUSIC algorithm. The original locations are shown in the 4th and 5th row. b) 2-D and 3-D subtopographies of approximation output produced by spatial decomposition and localization results of the associated topographies. Correct location of the dipole source is shown in the 4th row. c)2-D and 3-D subtopographies of the detail output produced by spatial decomposition and localization results for the detail topographies. Correct location of the dipole source is shown in the 4th row.

localize the source that is located in $BA44$ (Precentral Gyrus in Frontal Lobe). If the topographic map of $D3$ is further spatially decomposed into subtopographic maps, and then the approximation map is localized, an activation appears in $BA(44)$ (Precentral Gyrus in Frontal Lobe) which corresponds to the missing source. Additionally, the source localization of the detail map of $D3$, estimates the activation in $BA(8)$ as shown in Fig. 3.15(b, c). This additonal decomposition allows for the localization of two spatially separate sources which overlap in temporal and frequency domains. For the $D6$, the localization yields a single source close to $(BA)4$ (Precentral Gyrus in Frontal Lobe) as shown in Fig. 3.16(a). Similarly, the source which is located in BA (29) (Superior Temporal Gyrus in Temporal Lobe) cannot be localized. However, if we perform spatial decomposition to the topographic map of D6, and then source localize the approximation and detail maps, we can spot the activities in BA(29) (Superior Temporal Gyrus in Temporal Lobe) and BA(4) (Precentral Gyrus in Frontal Lobe), respectively, as shown in Fig. 3.16(b, c). Finally, the localization of A11 map yields and activation at the BA(39) (Angular Gyrus in Parietal Lobe) while the original locations of the simulated sources were both in the BA(39) region (one at the Inferior Parietal Lobule in Parietal Lobe and the other at the Superior Temporal in Gyrus Temporal). Again, the precise locations of activity are obtained when the spatially decomposed topographic maps of A11 are individually localized as seen in Fig. 3.17(b), (c). Localization of spatio-temporally decomposed topographic maps determine the exact locations of simulated sources without any localization error. Also, it has been observed that the detail maps are associated with the superficial sources while the approximation maps are responsible for the deeper sources as shown in Fig. 3.15(b, c), Fig. 3.16(b, c), Fig. 3.17(b, c).

3.4.3 Application to real data

Real EEG data is obtained from Istanbul University, Istanbul Medical School. Twenty−four healthy right−handed volunteers (13 males and 11 females) were recruited as subjects with a mean age of 25.8 ∓ 5.6 and a mean education of 17.8 ∓ 3.3 years. The cued continuous performance task (CPT) is designed to measure complex

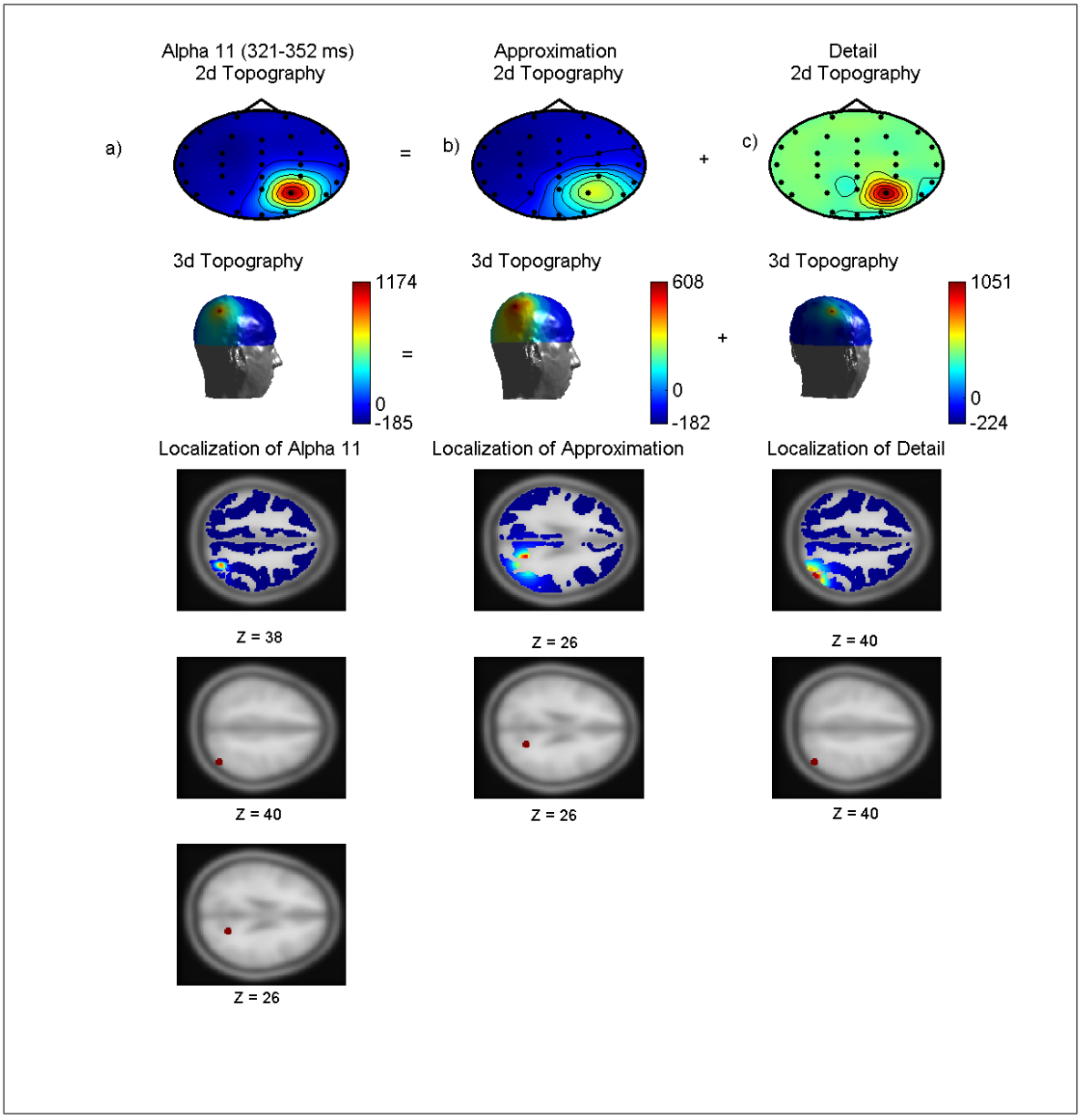

Figure 3.17 Subtopographies of spatio-temporal wavelet coefficients and their source localization. a)2-D and 3-D topographies of the Alpha 11 coefficient (321-352 ms) and localization results obtained by MUSIC algorithm. The original locations are shown in the 4th and 5th row. b) 2-D and 3-D subtopographies of approximation output produced by spatial decomposition and localization results of the associated topographies. Correct location of the dipole source is shown in the 4th row. c)2-D and 3-D subtopographies of the detail output produced by spatial decomposition and localization results for the detail topographies. Correct location of the dipole source is shown in the 4th row.

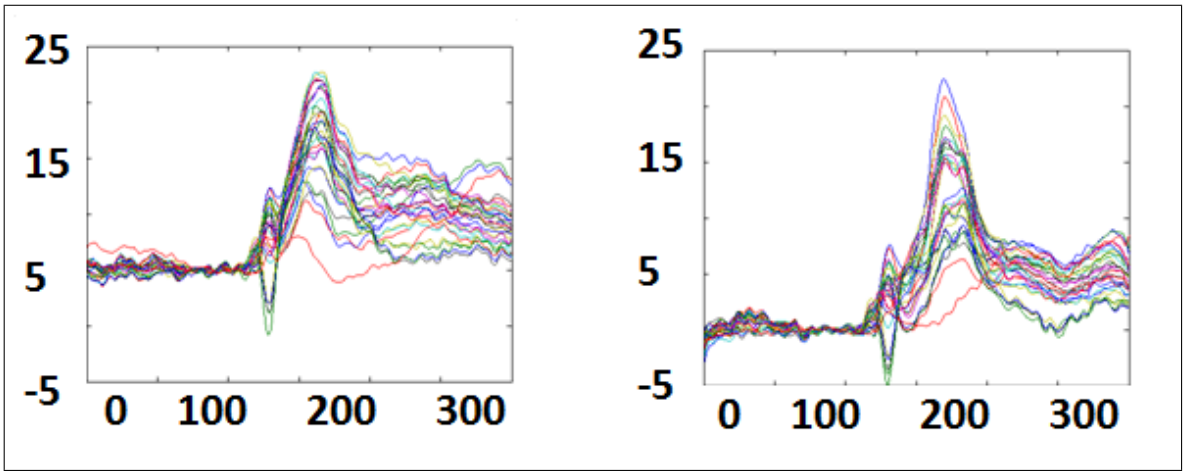

Figure 3.18 30 channel averaged ERP activity for Go and NoGo CPT respectively. Sampling Rate is 200 Hz and the duration is 1.5 second.

attentional functions [109]. CPT is used to measure sustained attention but is also sensitive to response inhibition and has been used for the assestment of numerous clinical entities such as attention, deficit disorder, schizophrenia and depression. The CPT paradigm consisted of 400 stimuli, 10 distractors (B, C, D, E, F, G, H, J, K, L), 1 primer "'A"', 1 target "'Z"' appearing with the following probabilities: 20% primers, 10% Go stimuli (any "'Z"' after an "'A"'), 10% NoGo stimuli (any distractor letter after an ""A"") and 60% distractors. EEG was amplified with a band pass of $0.1 - 70$ Hz from 30 scalp electrodes, Oz, O1, O2, Pz, P3, P4, P7, P8, Cz, C3, C4, T7, T8, Fz, F3, F4, FCz, FC3, FC4, CPz, CP3, CP4, FT7, FT8, F7, F8, TP7, TP8, FP1, FP2, and sampled at 200 Hz. After building the ERP epochs of 1500 ms duration between -500 and 1000 ms, trials with EEG or EOG amplitudes exceeding $\mp$ 90 μV were rejected automatically as artifact. ERPs were averaged for the Go and NoGo CPT paradigms as shown in Fig.3.18.

After the temporal wavelet decomposition is performed on the ERP data, it was observed that the Delta coefficient 3 (350-525ms) and the Theta Coefficient 4 (525-700 ms) coefficient exhibit higher values than the others. Inverse solution is computed using the RAP-MUSIC algorithm on these D3 and T4 maps and the source images are shown in Fig. 3.18. Then, 5 octave spatial decomposition is applied and the resulting subtopographies are source localized for both Go and NoGo datasets.

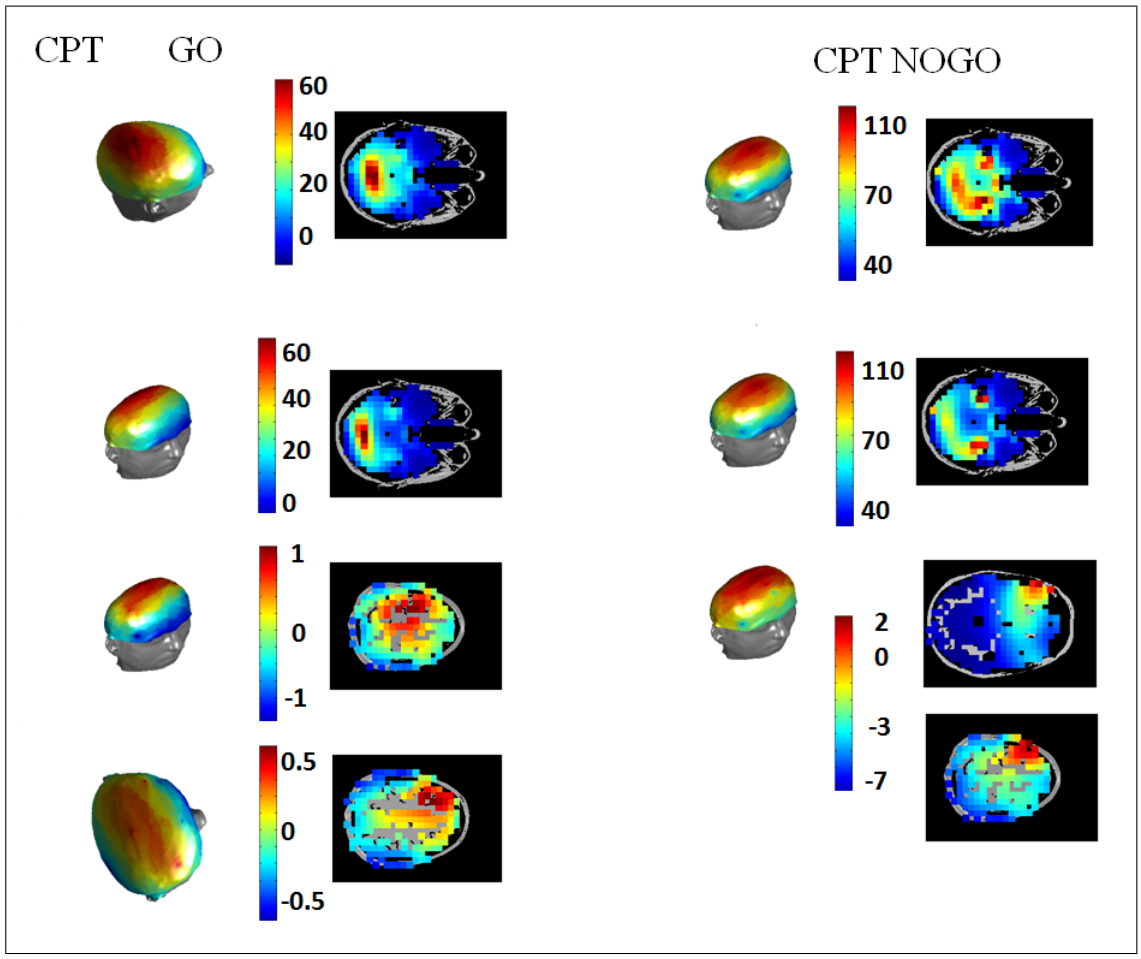

Figure 3.19 i)Temporal Decompositon (Delta Coefficient 3 (350-525ms)) ii)5 octave Spatial Decomposition and Localization for D3

3.4.4 Results & Discussion

The T4 coefficient that represents the theta response between 525 and 700 ms shows a left lateralized activation in temporally decomposed data. After spatial decomposition a clear activation is obtained on the left motor cortex that probably corresponds to the motor activity related with the button press with the right hand in addition to a cerebellar activation. The same time-frequency region in the NoGo condition shows two separate activations after spatial decomposition: One in the posterior parietal area and another activation in prefrontal cortex, which does not appear at all in the source localization of the temporally decomposed data. The orbito-frontal activation might correspond to the response inhibition in the NoGo condition of the CPT paradigm (Fig. 3.20). The D3 coefficient corresponding to the delta response between 350 and 525 ms mostly resembling the topography of the Go-P3 wave is represented with a single source in the temporaly decomposed data of the Go condition, whereas after spatial decomposition multiple generators appear in the mesial surface of the posterior parietal cortex and in left frontal area as expected for the Go-P3. The same delta coefficient in the NoGo condition seems to be generated by a parietal and two bilateral temporal generators when the raw data is used for source localization. After spatial decomposition two generators in the left frontal region appear in addition to a sharper dissociation of the parietal and bilateral temporal sources (Fig. 3.19).

3.5 Discussion & Conclusion

There is a vast amount of literature which demonstrate that the EEG data is a highly nonstationary activity because of its oscillations occuring in distinct frequency bands at different time windows. When the EEG data are associated with their electrical generators in the *3D* brain tissue, the existence of sources which are located at different spatial positions become important. When these multiple sources coincide on the same time window, at the same band, and/or at the same location, overlap in time/frequency/spatial region will occur. The spatial decomposition enables us to identify the topographic maps with different spatial frequency content which are related

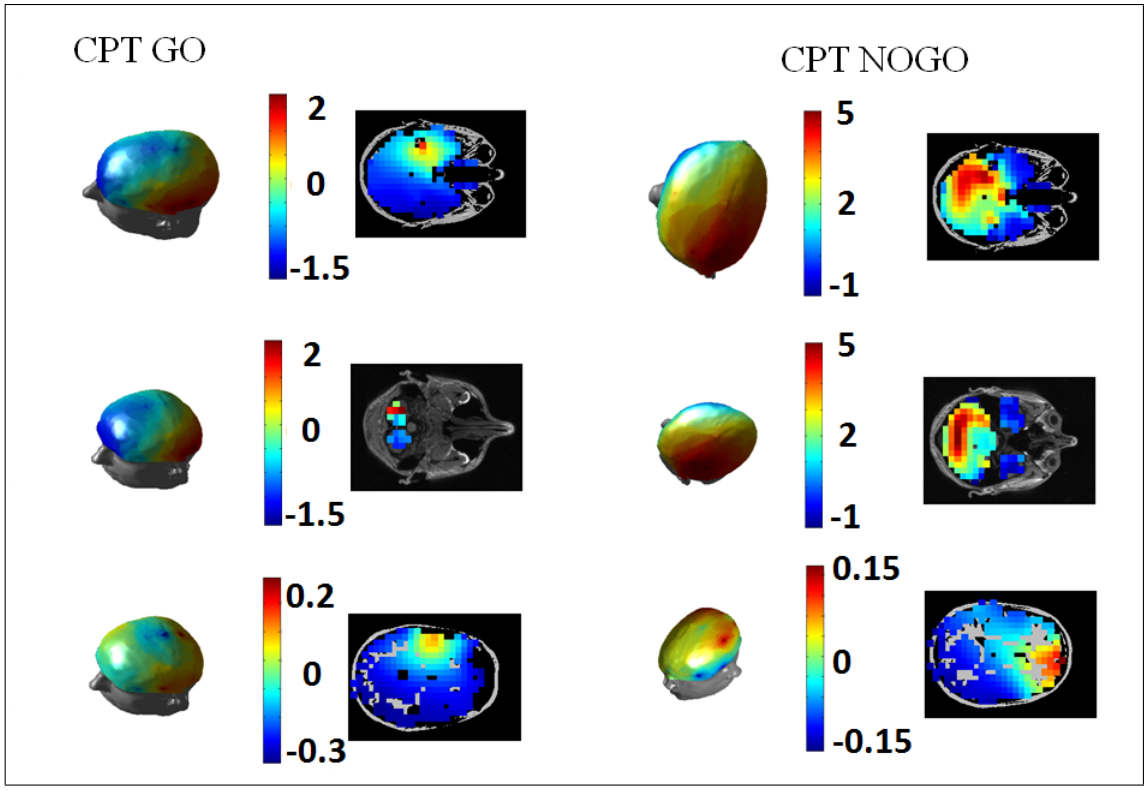

Figure 3.20 i)Temporal Decompositon (Theta Coefficient4 (525-700 ms)) ii)5 octave Spatial Decomposition and Localization T4

to the depth of the electrical sources. Temporal wavelet decomposition is a solution for identifying either the temporal or frequency domain overlap of EEG components. However, an additonal spatial decomposition of overlapping components yield several subtopographic maps which are associated with sources from different spatial depths. The source localization applied to the individual maps after decomposition may reveal the distinctly located sources. The subtopographic maps are simpler than the raw topographic potential distributions in their spatial frequency content. It has been shown that temporal wavelet analysis of EEG at a given spatial location yields temporally stationary components at different temporal frequencies like delta, theta, alpha. On the other hand, spatial wavelet analysis of EEG at a given temporal location yields spatially stationary scalp maps at different spatial frequencies determined by the depth of individual EEG sources. Therefore, a spatio-temporal preprocessing of the EEG simplifies the complexity of the scalp map into several maps produced by individual EEG sources, prior to their source estimation. The spatio-temporal processing of the multichannel data without any distortion requires implementing the wavelet transform algorithms on a topographic space based on a realistic scalp model. The method introduced for this decomposition involves a flatting of the topographic paths on the scalp through contortion and the dyadic wavelet transform algorithms are applied. Which of those subtopographic maps of a specific wavelet coefficient to choose is an important issue for localization. This is determined by measuring the spatial correlation among the detail maps and those with high correlations are merged. If the maps contain similar topographic information this compels for reducing the high number of detail maps to a single one by merging them all. For real EEG data these maps are very likely to contain more varying topographic information. In that case, multiple individual maps may be important for identifying spatially separate sources. On the other hand, the MUSIC can distinguish between the components according to their temporal frequencies and can perform localization for each of these components. However, it fails to localize two sources which are correlated in time (having the same frequency content) by yielding a single approximate location for two separate sources. ICA can be used as a preprocessing tool prior to source localization, but the assumption that EEG sources are independent is not so easy to justify especially for the brain which has synchronous activity in distinct locations during information processing. As they are supportive

preprocessing tools for the source localization algorithms, time-frequency [97] analysis and spatial decomposition [13] procedures are important steps to correctly determine the locations of EEG generators. In this thesis, it is aimed to combine these approaches on a spatio-temporal domain with an emphasis on performing the analysis on the topographic surface based on a realistic head model. The source localization algorithms rely on the topographic data obtained from multichannel recordings. Therefore, it is intuitive that the simpler the map becomes, the more reliable the inverse localization will be. The spatio-temporal wavelet decomposition does not presume any mathematical condition on the decomposed maps like uncorrelatedness or independence. It proves to be a preprocessing method to disambiguate the information arising from possible combinations of temporal, frequency and/or spatial overlappings of the EEG generators.

4. Epilepsy in Neuroimaging

4.1 Clinical approach to epilepsy

Epilepsy is characterized by the uncontrolled excessive activity of either a brain region or all off the central nervous system. Epilepsy, can be categorized into three main types: grand mal epilepsy, petit mal epilepsy and focal epilepsy.

Extreme neuronal discharges generated in the cortex or generated in the deeper parts of the cerebrum may form grand mal epilepsy. Also, these discharges are transmitted to the spinal cord and cause generalized tonic/tonic-clonic convulsions of the entire body. It is thought that a grand mal attack is probably caused by the abnormal activations generated in the lower portions of the brain. The brain lesions formed after trauma can cause excess excitability and these lesions can transmit signals into the reticular activating system to elicit grand mal seizures. On the other hand, people who have hereditary tendency to epilepsy, may have grand mal attacks under some factors such as; strong emotional stimuli, alkalosis caused by overbreathing, drugs, loud noises or flashing lights. Similar to the grand mal epilepsy, petit mal epilepsy involves the reticular activating system. The petit mal epilepsy is characterized by an unconsciousness period of 3 to 30 seconds. During this period, the muscles in the head region have several contractions (generally, blinking the eyes).

Focal epilepsy can originate from almost any part of the brain, either localized regions of the cortex or deeper structures of the cerebrum and brain stem. Lesions such as a destroyed area of brain tissue, a tumor that compresses an area of the brain or a region with a functional abnormality can be the generator of the focal epileptic seizures [110]. The epiloptogenic region is defined as the brain area whose removal eliminates the seizures.

For the patients whose drug therapy turns out to be ineffective, it is a common

method to identify the locations of sources that trigger the seizure in the brain tissue and resect them through surgical means for treatment. Identification of the brain region that generates focal seizures is an extremely important step for epilepsy surgery operations.

Presurgical evalution steps include clinical history, physical and neurological inspections, interictal EEG, ictal EEG, radiological imaging data (MRI, CT, PET), neuropsychological tests and psychiatric inspections. The locations of the brain regions that are responsible from the focal epileptic attacks, can be localized using the abnormal spiking waves observed in EEG. If epileptogenic region is indicated through the analysis of the data obtained by these steps, no further investigations are required. When the seizures do not arise from visible lesions in MRI, the source of the seizure may not be accurately identified, or a part of the brain may be misidentified as the epileptogenic region [111]. If the findings of the MRI and those obtained by the scalp EEG do not overlap, then further analysis with PET, ictal SPECT, MEG and invasive EEG may be needed [112]. The results of these tests may not necessarily show the exact location of the epileptic foci. However, these information may guide the placement of the electrodes that are placed directly to the brain tissue.

EEG and MEG measurements with high temporal resolution properties, are extremely important for the estimation of the underlying electrical sources. Several studies were performed that aimed to identify the locations of the epileptic foci using inverse reconstruction with spherical and realistic head modeling. Despite the usage of spherical models in forward solution, the locations of the interictal generators estimated by FINE and MUSIC are found to be in concordance with the position of the lesions yielded through the MRI [14]. The source localization of the interictal epileptic activity was performed using the MEG data of the lesional frontal lobe epilepsy patients and a good level of spatial concordance was demonstrated by matching Magnetic source imaging localizations obtained by the equivalent current dipole approach with pre and postoperative anatomic MRI data [15]. As a distributed inverse solution, LORETA was used to obtain the spatial extent of the ictal and interictal generators of the partial epilepsy patients whose lesions were identified by MRI [16]. It was also reported that the

use of realistic head model increased the dipole localization accuracy for epileptiform spikes with respect to the results obtained by the use of the spherical head models [113].

It is well known that, in simulation studies localization error obtained by using the MUSIC algorithm is minimum for the focal sources in the absence of noise. Moreover, in several studies, in clinical epilepsy, MUSIC [83, 84, 114] and RAP-MUSIC [85, 86] algorithms are used for localizing the sources of the measured scalp data. On the other hand, electric source imaging was applied to the scalp EEG of 152 patients before the resection surgery. Almost all patients had pathological epileptogenic lesions that were observed from the structural MR images. Thus, using the locations of the lesions deduced from MRI, it became possible to compute the EEG localization sensitivity and specificity over a group of patients. The sensitivity and specificity of imaging method was defined by comparing the localization of the source maximum with the resected zone and surgical outcome. It was shown that the specificity and sensitivity increased with the number of scalp electrodes [115].

Intraoperative electrocorticography (ECoG) has been traditionally used in the surgical management of medically refractory partial epilepsies to identify the location of the epileptogenic area, to guide the extent of resection [116]. It was shown that reliable source reconstruction can be obtained by the usage of MUSIC algorithm on ECoG data [117] while spatially distributed activations located on the cortex can be recovered using imaging approaches [118].

In this section of the thesis, the epileptic source localization is performed using both the non-invasive and invasive measurements. The source locations that are obtained through the scalp EEG are compared with the ones which are estimated using the deep or ECoG measurments. Moreover, simultaneously measured invasive and non-invasive recordings are analyzed in order to investigate the localization accuracy of the inverse solutions.

4.2 Non-invasive and invasive imaging of epileptic sources

The biophysical properties of the measured scalp potentials prevents the researchers or the clinicians to estimate the location of the underlying sources accurately. On the other hand, in the absence of the low-conductivity property of the skull tissue, it is obvious that the deep electrode measurements yield more reliable information about the brain activity. The direct electrical measurements of the brain can be obtained using the deep or subdural electrodes. Both types of electrode placement procedures can distress the patient. Moreover, skull extraction is needed for the placement of the subdural electrodes while opening holes on the skull tissue may be sufficient enough in order to place the depth electrodes.

The ideal solution of presurgical epilepsy diagnosis for medically intractable patients is the accurate localization of the epileptogenic area using the non-invasive measurements.

Depth electrodes enable clinicians to measure the electrical potentials in the deep brain tissues and the electrical sources that are responsible from these measurements can be obtained by solving the inverse problem. In the case of of depth electrodes, a precise electrode registration and forward modeling are needed for the inverse solution based on the intracranial measurements. Finite Difference method is a suitable forward solver for the depth electrodes. The solution domain can be represented with cubes having dimensions to be equal with the size of each sensor point on the depth electrode strips. A more realistic modeling can be obtained by using the DT imaging data to form an anistropic realistic forward model for the epilepsy patients [119].

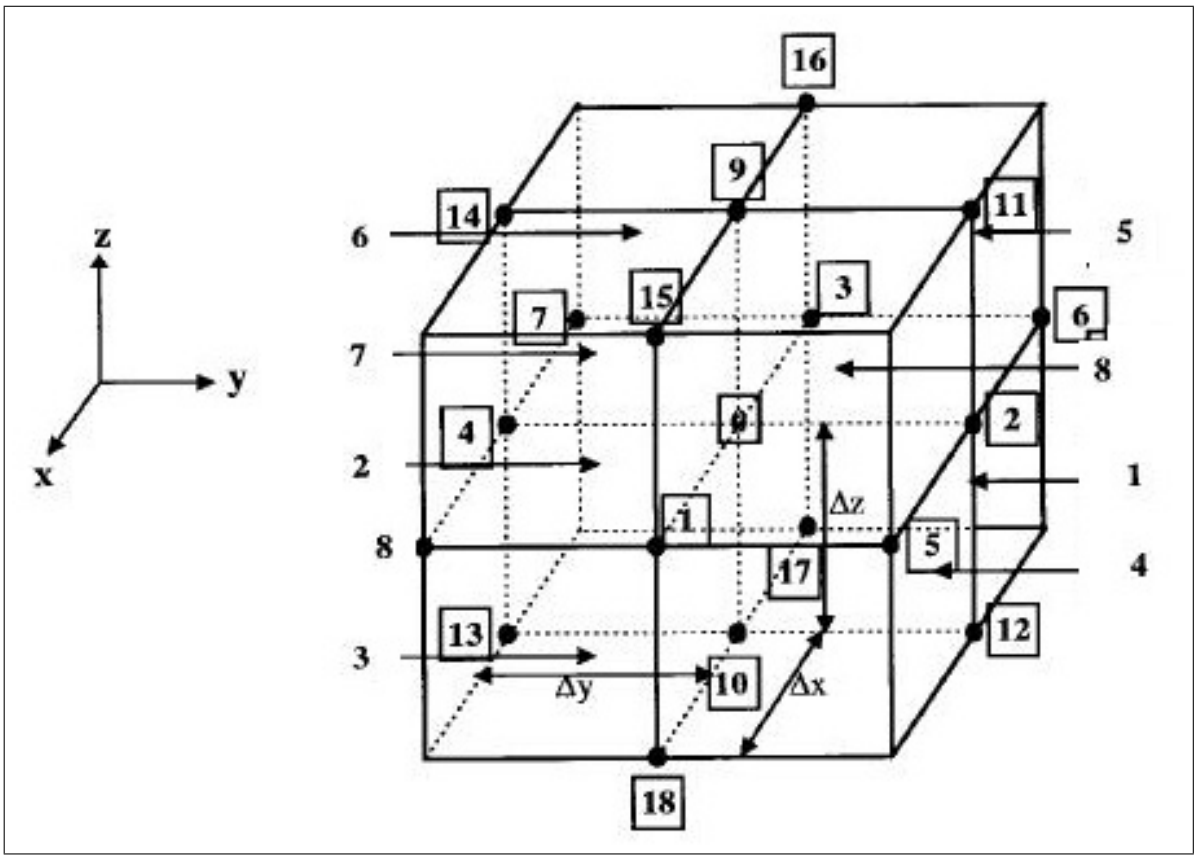

Figure 4.1 0 unit voxel element, Δx, Δy, Δz distances to the neighbouring voxels

4.2.1 Finite Difference Method

In a conductive medium, the electrical potentials caused by current dipoles can be calculated by the solution Poisson's differential equation (Eq.4.1),

$$\nabla(\sigma \nabla V) = J\delta(r - r_1) - J\delta(r - r2) \tag{4.1}$$

where $V \in \Re^{N_e \times 1}$, $\sigma \in \Re^{3\times 3}$ $r \in \Re^{3\times 1}$ is the location of the dipole, J denotes the current and r_1, r_2 direction of the current (dipole start and end points). Electrical conductivity and neighbouring properties of each volume element is taken into account for the solution of the FDM (Eq. 4.1) and Eq. 4.2 is used with Eq. 4.3.

$$\sigma = \begin{pmatrix} \sigma_{11} & \sigma_{12} & \sigma_{13} \\ \sigma_{21} & \sigma_{22} & \sigma_{23} \\ \sigma_{31} & \sigma_{32} & \sigma_{33} \end{pmatrix} \tag{4.2}$$

$$\sigma_{11}\frac{\partial^2 V}{\partial x^2}+\sigma_{22}\frac{\partial^2 V}{\partial y^2}+\sigma_{33}\frac{\partial^2 V}{\partial z^2}+2(\sigma_{12}\frac{\partial^2 V}{\partial x\partial y}+\sigma_{13}\frac{\partial^2 V}{\partial x\partial z}+\sigma_{23}\frac{\partial^2 V}{\partial y\partial z})+(\frac{\partial\sigma_{11}}{\partial x}+\frac{\partial\sigma_{12}}{\partial y}+\frac{\partial\sigma_{13}}{\partial z})\frac{\partial V}{\partial x}$$
$$(\frac{\partial\sigma_{12}}{\partial x}+\frac{\partial\sigma_{22}}{\partial y}+\frac{\partial\sigma_{23}}{\partial z})\frac{\partial V}{\partial y}+(\frac{\partial\sigma_{13}}{\partial x}+\frac{\partial\sigma_{22}}{\partial y}+\frac{\partial\sigma_{33}}{\partial z})\frac{\partial V}{\partial z}=J\delta(r-r_1)-J\delta(r-r2) \tag{4.3}$$

$$\sum_{i=1}^{18}U_iV_i-(\sum_{i=1}^{18}U_i)V_0=I\delta(r-r_1)-I\delta(r-r2) \tag{4.4}$$

The partial derivative operators in Eq. 4.3 can be written as the coeficients of U in Eq. 4.4 and the explicit expressions are given in Eq. 4.5 [120].

$$\begin{aligned}
U_1&=\tfrac{1}{4\Delta x^2}[\sigma_{11}(3)+\sigma_{11}(4)+\sigma_{11}(7)+\sigma_{11}(8)]\\
U_2&=\tfrac{1}{4\Delta y^2}[\sigma_{22}(1)+\sigma_{22}(4)+\sigma_{22}(5)+\sigma_{22}(8)]\\
U_3&=\tfrac{1}{4\Delta x^2}[\sigma_{11}(1)+\sigma_{11}(2)+\sigma_{11}(5)+\sigma_{11}(6)]\\
U_4&=\tfrac{1}{4\Delta y^2}[\sigma_{22}(2)+\sigma_{22}(3)+\sigma_{22}(6)+\sigma_{22}(7)]\\
U_5&=\tfrac{1}{4\Delta x\Delta y}[\sigma_{12}(4)+\sigma_{12}(8)]\\
U_6&=-\tfrac{1}{4\Delta x\Delta y}[\sigma_{12}(1)+\sigma_{12}(5)]\\
U_7&=\tfrac{1}{4\Delta x\Delta y}[\sigma_{12}(2)+\sigma_{12}(6)]\\
U_8&=-\tfrac{1}{4\Delta x\Delta y}[\sigma_{12}(3)+\sigma_{12}(7)]\\
U_9&=\tfrac{1}{4\Delta z^2}[\sigma_{33}(5)+\sigma_{33}(6)+\sigma_{33}(7)+\sigma_{33}(8)]\\
U_{10}&=\tfrac{1}{4\Delta z^2}[\sigma_{33}(1)+\sigma_{33}(2)+\sigma_{33}(3)+\sigma_{33}(4)]\\
U_{11}&=\tfrac{1}{4\Delta y\Delta z}[\sigma_{23}(5)+\sigma_{23}(8)]\\
U_{12}&=-\tfrac{1}{4\Delta y\Delta z}[\sigma_{23}(1)+\sigma_{23}(4)]\\
U_{13}&=\tfrac{1}{4\Delta y\Delta z}[\sigma_{23}(2)+\sigma_{23}(3)]\\
U_{14}&=-\tfrac{1}{4\Delta y\Delta z}[\sigma_{23}(6)+\sigma_{23}(7)]\\
U_{15}&=\tfrac{1}{4\Delta x\Delta z}[\sigma_{13}(7)+\sigma_{13}(8)]\\
U_{16}&=-\tfrac{1}{4\Delta x\Delta z}[\sigma_{13}(5)+\sigma_{13}(6)]\\
U_{17}&=\tfrac{1}{4\Delta x\Delta z}[\sigma_{13}(1)+\sigma_{13}(2)]\\
U_{18}&=-\tfrac{1}{4\Delta x\Delta z}[\sigma_{13}(3)+\sigma_{13}(4)]
\end{aligned} \tag{4.5}$$

According to reciprocity theorem, the electrical potential difference V_{e_i,e_j} of two electrodes (e_i, e_j) that is produced by the dipole at location $r(r_x, r_y, r_z)$ with the moment

vector $d(d_x, d_y, d_z)$ can be computed by solving the Eq. 4.6 [29]

$$V_{e_i,e_j}(r) = d^T \nabla V(r)(\frac{1}{I_{e_i}} - \frac{1}{I_{e_i}}) \tag{4.6}$$

where $\nabla V(r)$ is given in Eq. 4.7.

$$\nabla V(r) = (\frac{\delta V(r)}{\delta x}, \frac{\delta V(r)}{\delta y}, \frac{\delta V(r)}{\delta z})^T \in \Re^{3\times 1} \tag{4.7}$$

Assuming that each volume element can be a dipole source, the solution of linear system in Eq. 4.6 is provided for each source point using an iterative Conjugate gradient squared method. Thus, lead field matrix that transforms the source activity to the electrode activity is obtained.

4.2.2 Electrical source imaging with LORETA

Both parametric and imaging inverse solutions can be used on depth electrode measurements for localizing the sources. As a distributed solution, LORETA was used in several studies as mentioned above. LORETA inverse solution assumes that neighboring neuronal populations are simultaneously and synchronously activated. LORETA can be defined as selection of the smoothest of all posible *3D* current density distributions in the solution space. The solution space is a set of points on which the inverse solution will be searched. LORETA solution is implemented by minimizing the cost function given in Eq. 4.8

$$E(j) = ||V - Lj||^2_{C_e} + \lambda^2 ||Kj||^2 \tag{4.8}$$

where λ stands for the regularization parameter. LORETA imposes the spatial smoothness constraint onto the current distribution vector j. The spatial smoothness constraint is represented using the *3D* laplacian matrix K as illustrated in Fig.4.2. The laplacian operator on the solution space has the form of Eq. 4.9 [121]

$$K = (I_{Nv} - \frac{N}{6}) \otimes I_3 \tag{4.9}$$

where I_{Nv} is the unit matrice with the dimension of number of voxels (Nv) in the solution space and N is the number of neighbor voxels of each voxel in the solution space. For some voxels, it is not possible to find all the six predefined neighbors; i) the voxel might be at the boundary of the solution space, ii) calculated voxel coordinates might be out of the solution space. Thus, the number of orthogonal neighbours N for each voxel in the solution space has to be computed [122].

The computation of the regularization parameter λ is performed using the Akaike Bayesian Information Criterion (ABIC) [123].

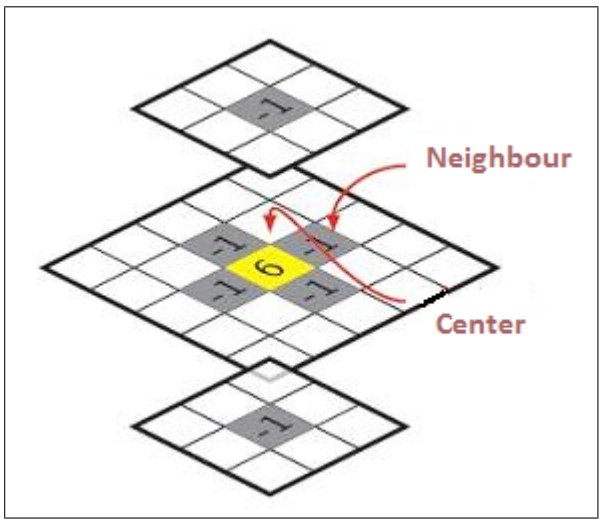

Figure 4.2 A center voxel is denoted with yellow color and its 6 orthogonal neighbours are represented with gray marks.

4.2.3 Electrical source imaging using, hierarchical observation model and Bayesian approach

The forward model of EEG given by a two-level hierarchical model can be formulated as in Eq. 4.10

$$Y = Lj + \epsilon_1 \qquad \epsilon_1 \approx N(0, C_e) \tag{4.10}$$

$$j = 0 + \epsilon_2 \qquad \epsilon_2 \approx N(0, C_p) \tag{4.11}$$

where ϵ_1 denotes the observation error and ϵ_2 represents the unknown source activity. The two-level model in Eq. 4.10 and Eq. 4.11 can be written as in Eq. 4.12 and the covariance (C_v) of the measured scalp data (Y) can be written as in Eq. 4.13.

$$Y = L\epsilon_2 + \epsilon_1 \tag{4.12}$$

$$C_v = LC_pL^T + C_e \tag{4.13}$$

The empirical Bayesian approach is adapted to solve the EEG inverse problem based on the hierarchical observation model Eq. 4.10. This source reconstruction method allows for a design of spatio-temporally optimized filter function that projects the EEG data at the sensor space to the current distribution in the source space.

$$Cov(vec(\epsilon_1)) = V_e \otimes C_e \tag{4.14}$$

$$Cov(vec(\epsilon_2)) = V_p \otimes C_p \tag{4.15}$$

The temporal correlation matrix (V_e) of the observation noise is assumed to be an identity matrix in this study. (The symbol $\otimes$ stands for the Kronecker product.) The temporal correlation structure of the sources (V_p), is constrained by the first 200 principal eigenvectors of a Gaussian auto-correlation matrix with standard deviation ($s = 2$), windowed with a rectangular function (nt) denoted as S [13]. S transforms the temporal covariance structure of the sources to a subspace that embeds the temporal covariance structure of the sensors. The spatial covariance structure of the sensor space is assumed as an identity matrix and given as

$$C_e = \lambda_1 Q_1 \tag{4.16}$$

and the spatial covariance structure of the source space is

$$C_p = \lambda_2 Q_2 + \lambda_3 Q_3 \tag{4.17}$$

where HQ_2H^T is the spatial smoothing (spatial coherence) constraint projected to the sensor space formed by applying a Gaussian kernel with a FWHM of $6mm$ to the

geodesic distances between the vertices of the triangles forming the source manifold. HQ_3H^T is similarly projected as the probability constraint for voxels for their belonging to the gray matter tissue. The hyperparameters of the covariance constraints λ_1, λ_2 and λ_3 are estimated using iterative restricted maximum likelihood (ReML) algorithm defined by Phillips et al. [124]. Once the hyperparameters of the covariance constraints are determined, the mean source activity is estimated using $\hat{j} = MYSS^T$ based on maximum a posteriori (MAP) operator M as shown in Eq. 4.18.

$$M = C_p H^T (HC_p H^T + C_e)^{-1} \tag{4.18}$$

The conditional expectation of the energy over sources is computed as

$$\hat{E} = M(YGY^T)M^T + (H^T C_e^{-1} H + C_p^{-1})^{-1} tr(GV) \tag{4.19}$$

where W is the time-frequency constraint matrix and G is the energy projection operator given as

$$G = SS^T WW^T SS^T \tag{4.20}$$

and V is the temporal correlation of signal and $V = V_e = V_p$. The diagonal terms of the energy matrix correspond the source energy.

4.2.4 Case 1: Epileptic source reconstruction using deep and scalp EEG

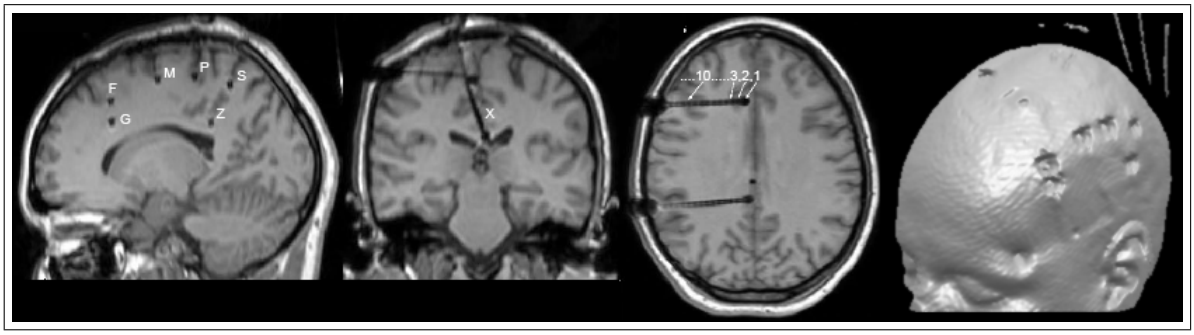

Figure 4.3 Sagittal, coronal, axial and *3D* views of postoperative T1 weighted MR images. Deep electrode locations are marked on the slices (Data is obtained from Czech Republic, Brno Epilepsy Center).

The MR images, surface EEG data and the deep electrode measurements were obtained from the Department of Neurology, Brno Epilepsy Center, Czech Republic. Interictal seizure data is collected from 19 channel electrode locations (Fp1, Fp2, F7, F3, Fz, F4, F8, T7, C3, Cz, C4, T8, P7, P3, Pz, P4, P8, O1, O2) and both of the sampling rates of the scalp and deep electrode EEGs are 128 Hz. A realistic head model is derived from the T1 weighted MR images of the subject as shown in Fig. 4.3. Boundaries of scalp, skull and brain regions are determined from the anatomical MR images and isotropic conductivity is assumed. The sufaces are tesselated with $4000, 4200$ and 4200 triangles. The realistic head model, locations of the scalp and deep electrodes can be seen in Fig. 4.4. Scalp electrodes are registered to the head model, by spline interpolation using the T1 weighted MR data and the inion and nasion coordinates. For the distributed source reconstruction process, the source space is discritized using cubic volume elements whose dimension is set to $4mm \times 4mm \times 4mm$. 105 contact points of deep electrodes are registered to realistic head model. The information including the physical properties of the strip electrodes and the locations where the strip electrodes enter the brain tissue, is used to compute the exact positions of the sensors in the brain.

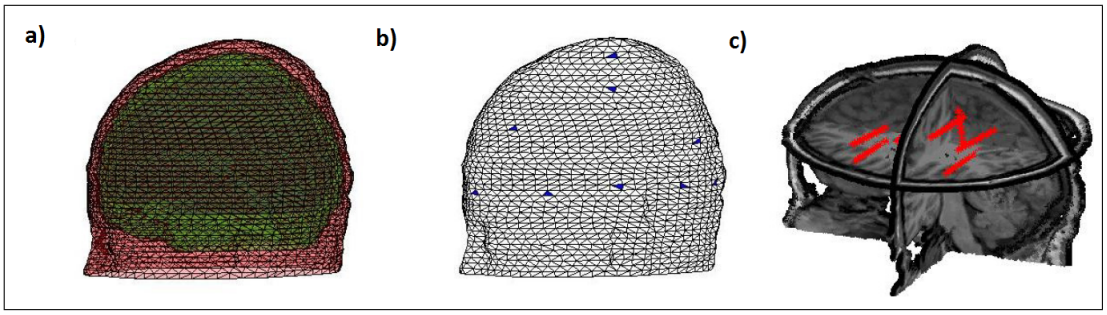

Figure 4.4 a)The realistic head model formed by triangulated surfaces of the scalp, skull and brain tissues. b) 19 electrodes are registered to scalp surfaces. Blue colored triangles denote the electorde locations. c) Red points denote the contact points of the deep electrodes. Deep electrodes are placed to the left hemisphere of the brain.

The scalp EEG and the deep electrode data is analyzed using two separate processes. For the scalp data, forward problem is solved using BEM COG approach. For each of the scalp EEG data frames which are marked to be related with the seizure, inverse solution is obtained through the LORETA approach. For the deep electrode data, FDM solution is computed only for the brain tissue that is bounded with the

limits determined by the locations of the deep electrodes. As epileptic discharge waveforms for the scalp EEG, 1150 spikes are selected by visual inspection. In a similar way, 1600 spikes are detected from deep electrode recordings. Inverse problem is solved using BEM based LORETA for the 1150 scalp EEG data individually and their average current source density is computed. The maximum value of this average map is determined as the source location. FDM based LORETA is applied to 1600 deep EEG spikes and their average current source distribution is computed. Several maxima of the average map are detected.

As a result, BEM based source distribution of scalp EEG is given in Fig. 4.5b. Epileptic focus appears to be in the vicinity of the C3 electrode as a superficial activity. This result complies with the surface EEG topography as shown in Fig. 4.5c. Multiple sources are observed in the FDM based source distribution of the deep EEG as shown in Fig. 4.5a. Only one of these sources, which is also the weakest one, is close to the source obtained by the scalp EEG localization. The other sources are deeper and have higher strengths [125].

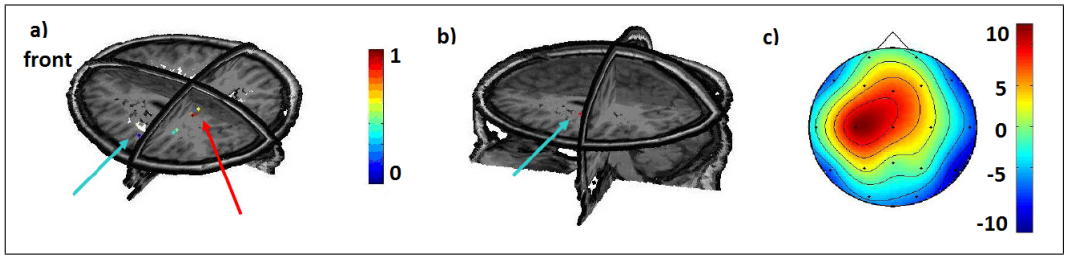

Figure 4.5 a)The source locations obtained from the deep electrodes using the FDM based, b) from the scalp EEG using the BEM based LORETA approach, respectively (activity is normalized individually). c) Average Scalp EEG topography of the selected 1150 peaks.

4.2.5 Case 2: Epileptic source reconstruction using subdural and scalp EEG

The MR images, surface EEG data and the subdural electrode measurements were obtained from the Department of Neurology, Cerrahpasa Medical School. The subject is reported to have at least one epileptic seizure in a day. Structural MR images of the subject was analyzed by the radiologists and a lesion could not be identified for

the seizure. The ictal and interictal scalp video EEG is collected from 20 electrodes (Fp1, Fp2, F7, F3, Fz, F4, F8, T7, C3, Cz, C4, T8, P7, P3, Pz, P4, P8, O1, O2, Oz).

Forward head model is obtained using T1 weighted MR images and the scalp, skull and brain surfaces are triangulated with 2466, 2340, 1575 vertices, and 4837, 4574, 3146 triangles, respectively as shown in Fig. 4.6.

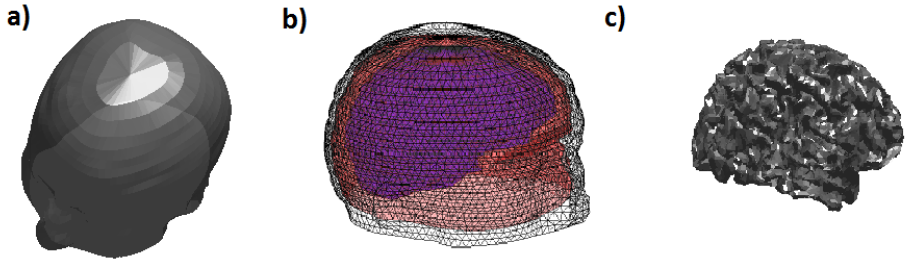

Figure 4.6 a) Scalp model is obtained using the MR images. b) Concentric surfaces of scalp, skull and the brain tissue having homogeneous conductivity values are triangulated with 2466, 2340, 1575 vertices and 4837, 4574, 3146 triangles, respectively. c) Cortical source space used for the inverse problem.

RAP-MUSIC algorithm is used for source reconstruction of preictal EEG measurements. Activation points are marked with red spheres as shown in Fig. 4.9. The placement of subdural electrodes are decided using the information obtained from the physical examination, video recorings and the dipole location that is gathered through the scalp EEG (gray spheres in Fig. 4.9). Subdural electrodes are placed on the cortex with an invasive operation. The subdural electrodes were incompatible with the MR, therefore postoperative structural images were acquired by CT. These images were then used to check whether the location of the subdural electrodes are appropriate or not. 80 subdural electrodes with 1cm inner distance which are placed over the cortex is shown in Fig. 4.8.

The contrast of the electrodes are higher than the image value of the other tissues. Thus, the digital coordinates of the subdural electrodes are calculated by using a basic thresholding. Once the locations of the subdural electrodes on CT images are found, these locations are needed to be converted to the MR space on which the realistic head was computed. The CT images and MR images are coregistered in order to find the corresponding locations of the subdural electrodes on the MR image. This

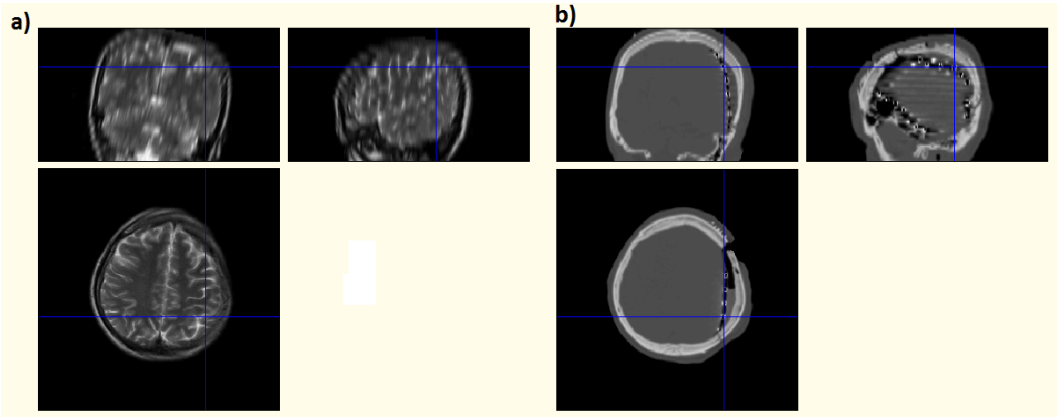

Figure 4.7 a) MR image, b) White dots in the CT images denote the locations of the subdural electrode contacts

procedure enabled us to analyze the multimodal information on a common spatial space (Fig. 4.7). After the placement of the subdural electrodes, video EEG recordings are

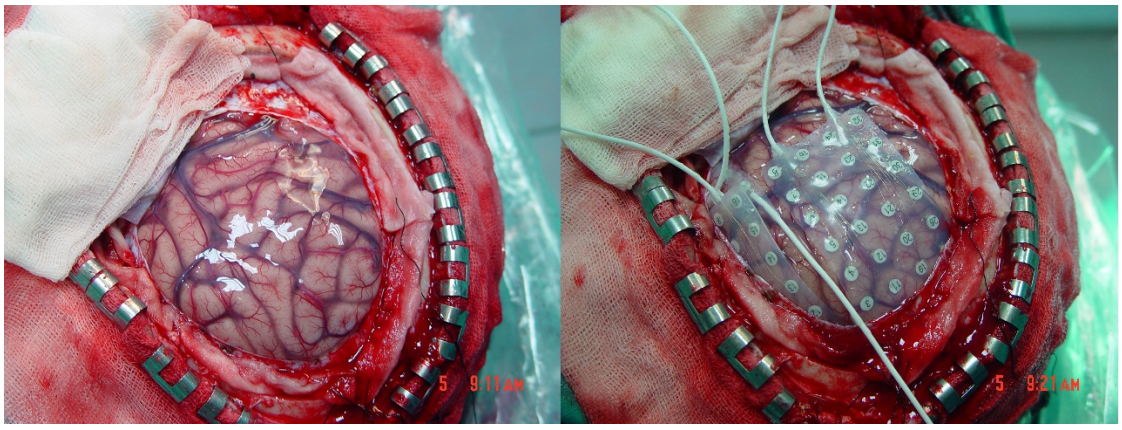

Figure 4.8 Placement of the subdural electrodes to the right hemisphere of the subject during an invasive operation (Image is obtained from Neurosurgery Department, Cerrahpasa Medical School).

performed for 24 hours without the scalp electrodes. In this time period, the patient had 2 seizures, and preictal period source locations are identified as shown in Fig. 4.9. When the two result sets are compared, 1 cm distance was observed between the source locations obtained through the scalp EEG and the subdural electrodes.

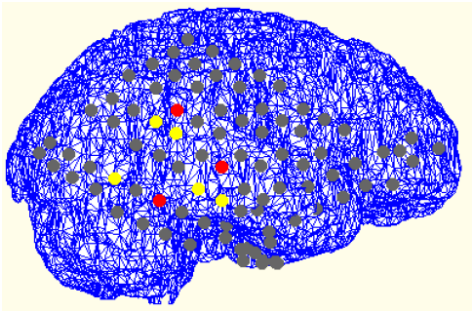

Figure 4.9 Subdural electrode source localization is shown in yellow, scalp EEG source localization is shown in red and the locations of the other subdural contact points are drawn with gray color.

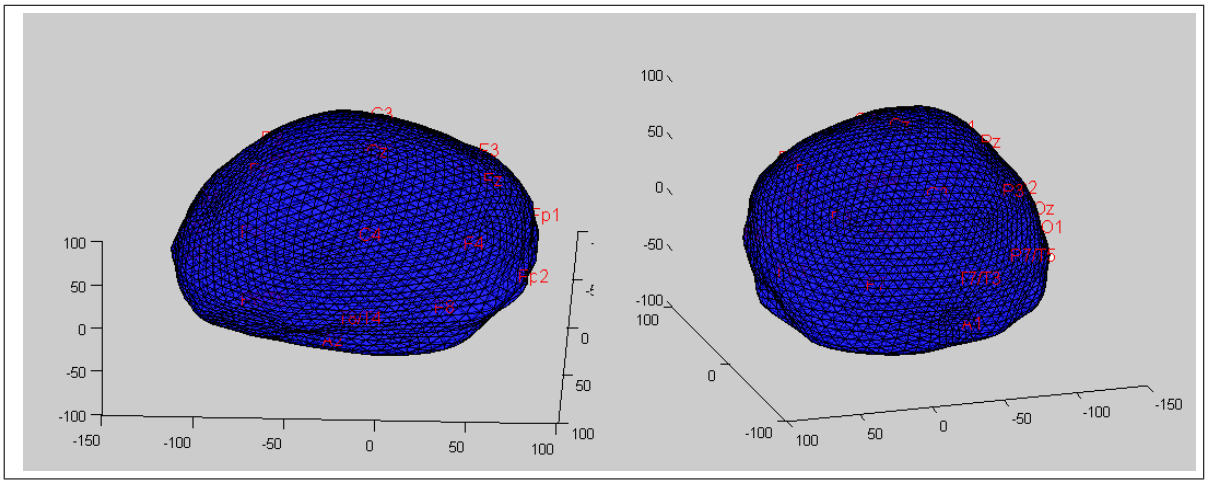

Figure 4.10 Scalp model is represented with 5000 triangles and 2500 vertices. 22 electrode locations are registered to the scalp model using international $10-20$ electrode placement system.

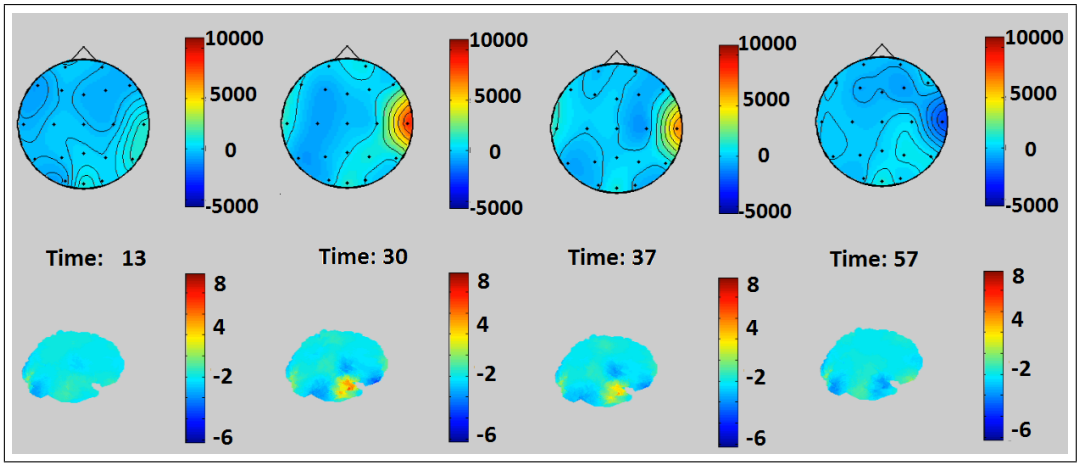

Figure 4.11 Preictal period topographic distribution of the electrical potentials and the correponding source images on the cortical surface estimated through the linear inverse solution.

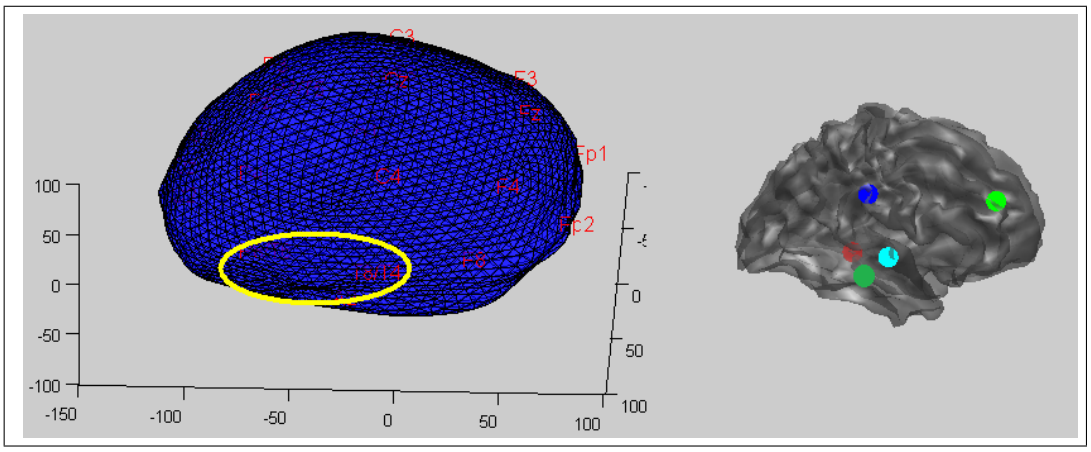

Figure 4.12 (Left) The anotomical location that is thought to be responsible from the seizures is marked with a yellow ellipse. (Right) The source locations that are estimated by the inverse solution for 4 different seizures are marked with colored spheres.

4.2.6 Case 3: Epileptic source reconstruction using simultaneously measured deep and scalp EEG

Anatomical MR and CT imaging was applied to the patient in order to test if there exists a lesion. Radiological inspectation results could not identify anatomical lesions. The dose of the antiepileptic drugs are decreased and the video EEG recordings are performed for one day. Neurological analyses of the video EEG recordings yield some abnormal waveform activity at right parieto-occipital electrodes. These activity patterns are thought to be responsible from the seizures. Because of the observation noise, the projection of these patterns to right temporal and frontal areas, complicates the exact source localization of the seizure. It was reported that the origin of the seizures are at the right hemisphere at the back or at the mid part, probably right mid temporal areas.

Realistic head model of the patient is formed using the anatomical MR images as shown in Fig. 4.10. Source reconstruction is performed using both RAP-MUSIC and Bayesian distributed inverse solution for the preictal period scalp EEG (Fig. 4.11). Neurologists used the information collected from the video EEG findings, semiological data and the source activation maps obtained by the inverse solution, in order to decide the locations of the subdural electrodes. After the placement of subdural electrodes, postoperative anatomic MR imaging is performed (Fig. 4.13). These anatomical images

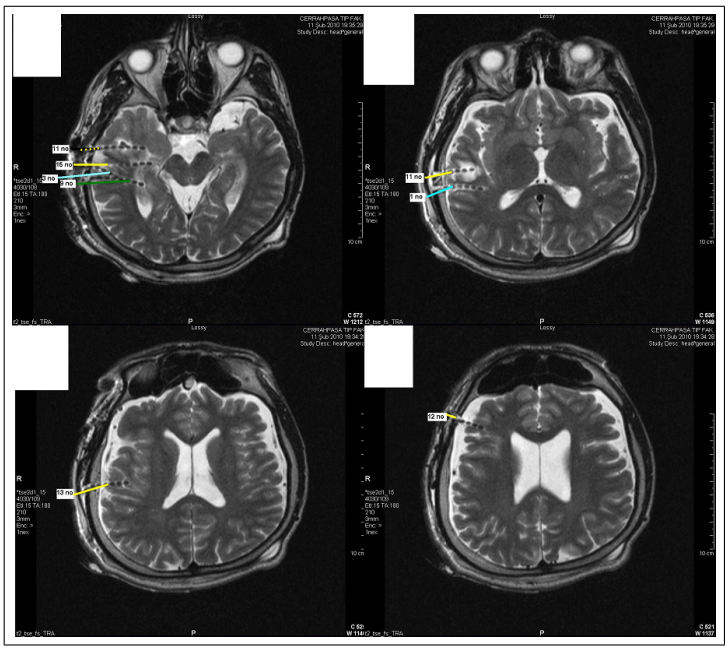

Figure 4.13 Postoperative T2 wieghted MR images. The locations of the deep electrodes are shown with colored markers (64 contacts).

are used to register the subdural electrodes to the realistic head model. Geometrical properties of the electrodes are used to model the deep sensors. The locations of the start and end points of these electrodes in the head model is calculated (Fig. 4.13). By this way, the contact points of the deep electrodes are registered to the inverse solution space as shown in Fig. 4.14. After the deep electrode placement, video EEG recordings of the patient are performed. With the reduction of the dosage of the antiepileptic drugs, patient had 3 seizures during the recordings. Simultaneous scalp EEG measurement is also performed during this period. The video EEG recordings are analyzed by the neuorologists and the case report is summarized as;

- Irregular delta waves originated from the bilateral centro-parietal area, propagates to frontal area and at postictal period irregular delta waves were observed in frontal-central area.
- Significant EEG activity is observed at the right temporal area
- Irregular waveforms observed at T6-T4, theta and delta, (4-6 Hz), and propagates in 2 seconds to all right hemisphere, and finalizing with a rhytmic activity.

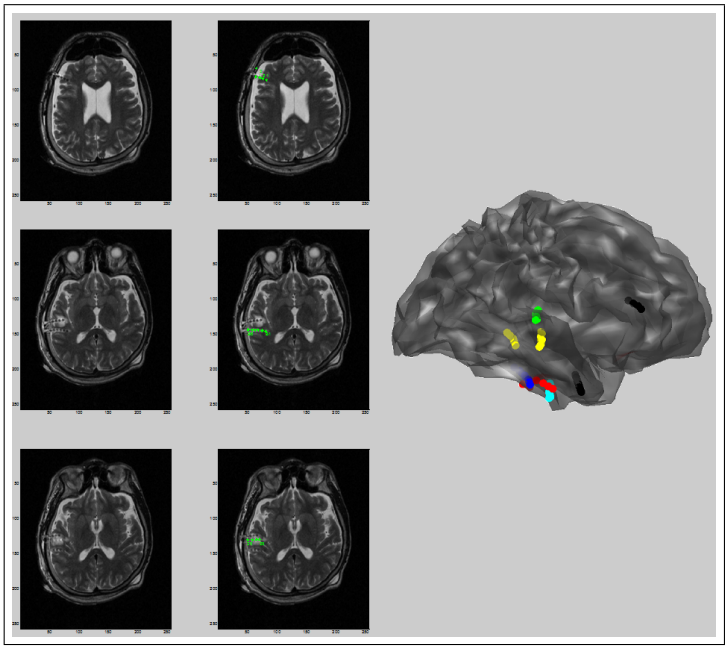

Figure 4.14 Locations of the deep electrode contacts are shown; i) on the T2 weighted MR images and ii) on the cortical source space.

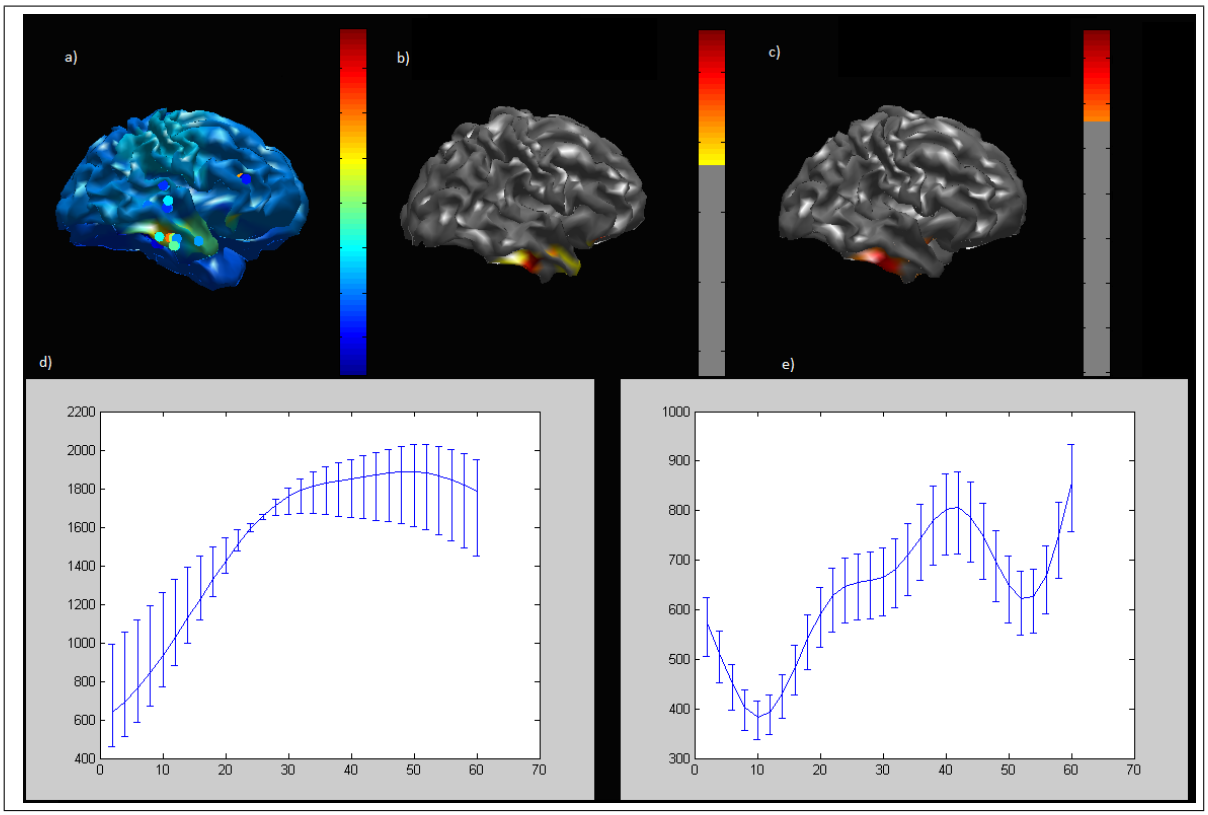

Figure 4.15 a) Deep electrode activity of preictal period b) Preictal deep electrode activity amplitude greater than its 80% of the maximum value c) Source activity deduced from the linear inverse solution d) The temporal dynamics of the deep electrode measurements which are projected to the cortical surface (sampling rate: 1024 Hz) e) The temporal waveform obtained through the linear inverse solution.

In order to investigate the localization accuracy of the inverse solutions, the epileptogenic brain locations are estimated using the linear and RAP-MUSIC algorithms separately on the preictal seizure scalp EEG. The simultaneosuly measured preictal deep electrode measurements are assumed to show the exact locations of the epileptic focus. This information is used as a reference to compare the output obtained using the scalp EEG. Linear inverse solution exposed that the preictal sources are localized within a $6-7$ mm distance from the sources deduced by the deep measurements as seen in Fig. 4.15. Both spatial extend and the temporal waveform of the sources exposed by the linear inverse solution are in agreement with the respective deep electrode measurements. On the other hand, the epileptic focus locations obtained by the RAP-MUSIC inverse solution differed from the deep electrode measurements.

4.3 Discussion and Conclusion

Invasive measurements provide a detailed information about the activity of the epileptic sources without a significant noise corruption and signal distortion. In the analysis of the deep and scalp EEG data of the first subject, forward problem of scalp source reconstruction was solved using BEM COG while the FDM solution was computed for the deep electrodes. FDM has the opportunity to compute the electrical potential values inside the brain tissue within the millimeter resolution. Also FDM based deep EEG localization was much more sensitive to the sources inside the brain. Source imaging for both datasets were performed using the LORETA approach. LORETA was used to obtain the spatial extent of the ictal and interictal generators of the partial epilepsy patients [16]. From the scalp EEG, seizure source was localized as a superficial one while the FDM based analysis of the deep electrode measurements exhibited the same area with some additional deep sources. It is well known that when the scalp EEG is used, LORETA has a poor sensitivity to the deep sources than to the superficial ones. The results indicate that using the deep electrode measurements even the deep sources can be captured by LORETA.

As a parametric inverse solution, RAP-MUSIC algorithm was used for localizing

the sources of the measured scalp data [85, 86]. It was also shown that reliable source reconstruction could be obtained when implemented on the ECoG measurements [117]. For the second subject, RAP-MUSIC inverse solution was obtained for both the ECoG and scalp EEG data based on a BEM realistic forward model. When the two result sets were compared, it was seen that the estimated activity from the scalp measurements differ at most 1 cm distance from the source locations obtained through the subdural electrodes.

For the third subject, simultaneously measured deep electrodes and scalp electrode data were analyzed separately. The exact locations of the epileptogenic area were deduced from the preictal deep electrode measurements. This information was used to compare the scalp EEG source localization results. Both types of source reconstruction approaches (parametric and imaging) were performed on the scalp EEG data. For the parametric approach, RAP-MUSIC algorithm, and for the imaging approach, Bayesian approach was adopted as a linear solution. In this case, linear solution was succeeded in localizing the sources with minimum localization error while the epileptic focus locations obtained by the RAP-MUSIC inverse solution differed from the deep electrode measurements. Moreover, the temporal waveform of the sources exposed by the linear inverse solution were similar to the respective deep electrode measurements.

The invasive electrode placement procedure is a difficult and a risky operation both for the surgeon and the patient. Thus, the locations of the electrodes and the number of the electrodes that are going to be used, must be selected properly. For this reason, the non-invasive measurements should be carefully analyzed and the epileptic source locations should be estimated as a prior information for further invasive studies.

5. Multimodal functional neuroimaging: EEG & fMRI fusion

5.1 EEG & fMRI fusion theory

Functional magnetic resonance imaging (fMRI), encoded by the blood oxygen level dependent (BOLD) signal, is widely used for making inferences about regionally specific activations in the brain. However, the relationship between BOLD and neuronal activity still needs to be elaborated as to how the hemodynamic response is influenced by the temporal dynamics of the underlying neuronal activity. Since the electrophysiological signals are more directly related with the neuronal dynamics, it is well suited to study the relationship between the hemodynamic signal and the neuronal activity patterns non-invasively by combining the fMRI BOLD signal having a fine spatial resolution of milimeters with the electroencephalogram (EEG) registering the neuroelectrical activity at a high temporal resolution in milliseconds.

The plausibility of such multimodal imaging approach is mainly based on the solid findings of neurovascular coupling studies carried out in animal brain with invasive intracranial electrophysiological measurements within voxels of the BOLD signal (Logothetis et al. [126]). These studies revealed that the hemodynamic signal shows a strong correlation with the local field potentials, that reflect the sum of post-synaptic activity within a brain volume, rather than the multiunit activity corresponding to the summation of the action potentials generated in the neighboring neurons. These results suggest that a similar correlation is also plausible between the scalp recorded EEG and BOLD signals, because the EEG is also based on cortical post-synaptic activity similar to the local field potentials. However, the critical distinction between local field potentials and the EEG is that due to the volume-conduction in the brain and the spatial smoothing effect of the skull and the scalp tissues, the EEG reflects only the part of the synaptic activity that is synchronous among a large group of voxels distributed in a wide area of the cortex (Nunez 2000, [127]). Hence, EEG reflects a subset of the activities present in the cortical volume. Transient waveforms such as epileptic spikes

as well as the spontaneous, evoked or induced rhythms in various frequency bands of the EEG reflect such synchronization patterns (Basar 92-2001 [128, 129]).

The basic philosophy of the integration resides on exploiting the virtue of one modality to compensate for the weakness of the other in terms of temporal or spatial resolution. The relationship between EEG and fMRI is denoted with positive, negative or no correlations between the signals [130, 131, 132, 133]. These types of EEG/fMRI integration studies mainly focussing on asymmetric approaches are twofold;

i) Temporal information obtained from the EEG can be used as a constraint or regressor in the analysis of fMRI [17, 18]. As a temporal information, a vector that included the time indices of the epileptic spikes or the amplitude of the alpha rhythm was convolved with a canonical hemodynamic response function (HRF) to obtain a reference function which is used to correlate with the BOLD response (Goldman et al., 2002;Moosmann et al., 2003). In another study, the power of the scalp measurements in the alpha band in 2.5 s epochs that corresponds to a TR period is computed using FFT. The alpha power was averaged over the four bipolar channels (T6-O2, O2-P4, T5-O1, O1-P3) and then the averaged time series was convolved with an a priori hemodynamic response function. Finally, a voxel-wise correlation computation was performed between the resulting and the fMRI time series. It was shown that the alpha power correlated negatively with the MRI signal in the occipital parts while positive correlations of alpha power with the MRI signal were observed in the thalamus [134].

A similar correlation investigation study was performed by Laufs et,al. The spectral power of the averaged $O1/O2$, $C3/C4$, $F3/F4$ channels were computed for one second epochs. The computed power was then mean-scaled and averaged across the alpha band ($8-12$Hz) and downsampled to achieve the temporal resolution of the fMRI. For the computation of correlation between EEG and fMRI, a design matrix was formed that included alpha band power convolved with HRF as a regressor. Motion correction confounds and high-pass filtering were also included in the design matrix. A significant cortical activity (bilateral frontal and parietal) was found when the alpha band power decreased. For all three regressors, similar activations were observed while

the best significance was achieved with $O1/O2$ electrodes [20].

Recently, a method that automatically extracts the interictal eplieptiform discharges (IED) from the scalp EEG measurements based on ICA and wavelet analysis was used for the combination of EEG-fMRI data. The wavelet power of the EEG signal due to IED was used as a regressor in GLM to identify the brain regions that were responsible from the IEDs [18]. All these studies used the temporal information obtained from the EEG to explain the BOLD signal changes.

ii) EEG inverse problem can be constrained spatially by the high resolution fMRI active regions as the precursors to the source reconstructed images (asymmetric fMRI-EEG approaches) [23, 24, 25, 26, 27].

The source covariance matrix that contains the information about the BOLD response to the stimuli was used to constrain the the EEG linear inverse solution [27]. This procedure was also used within a parametric empirical Bayesian framework [28] where the voxels that are known to be significantly active via the fMRI analysis were used to form spatial priors on the EEG sources.

Another type of data driven approach was used to define a voxel based EEG-BOLD transfer function by predicting the changes in BOLD signal using the current and past values of the scalp EEG data as an exploratory variable [135]. The fundamental limitation of the these data driven asymmetrical integration approaches come from the attempt to predict one phenonemon using the information coming from the other, instead of fully exploiting the simultaneously recorded data from the two modalities. This way, either the temporal limitations of the fMRI or the spatial limitations of the EEG are alleviated. A more sophisticated attempt to overcome this non-ubiquity of EEG-fMRI is to propose symmetrical approaches by i) either proposing biophysical models that can incorporate the electrophysiological and hemodynamic activities within a framework of a set of coupled equations that can explain the behavior of both activites [136, 137] ii) or empolying several data driven approaches based on decompositions and/or inversions [138, 139, 140]. Both the symmetrical and asymetrical

approaches are critically reviewed in ([141, 142]).

5.2 Steady State Visual Evoked Potentials

As the temporal resolutions of both modalities are in different scales, a reliable exploration of the relationship between the synchronized neuroelectrical activity patterns and the hemodynamic response requires the alignment of the temporal resolution of both signals on a common scale. The steady-state evoked potentials are well-controlled measures among the synchronization schemes, which reflect oscillatory EEG patterns that can be stationary for the time period of the BOLD signal. On the other hand, steady-state evoked potentials still include the high temporal resolution of the EEG in terms of well-resolved temporal frequencies of the stationary oscillatory responses. They occur in existence of stimulus trains with an inter-stimulus interval (ISI) which is shorter than a complete processing of a single stimulus [143]. The EEG response to a single stimulus is observed as a decay in hundreds of milliseconds, while driving the brain with stimulus trains having shorter ISIs result in regular oscillatory responses. For example, in the visual modality the EEG segments averaged phase-locked to the stimuli enable us to observe the EEG oscillations at the stimulation frequency and its first and second harmonics with flickering light up to 100 Hz frequency [144]. The amplitudes at the stimulation frequency and its harmonics can be easily determined from the frequency spectrum of the SSVEP. This also helps to exclude the effects of the EEG artifacts occurring at other frequency ranges, leading to a relatively stable electrophysiological measurement. These characteristics of SSVEP makes it a preferred method for the investigation of basics of EEG/fMRI fusion studies without the assumption that the two signals at two different time scales are originated from the same neuronal sources.

Functional neuroimaging of the steady state behaviour of the human brain using PET/EEG [145], fMRI/EEG [146] dates back to the beginning of 2000's. The steady state behaviour of the brain is also simultaneously measured with EEG-fMRI in [147]. In these studies, the major approach is based on correlating the parameters such as

the spectral power obtained from EEG electrodes and the fMRI BOLD signal within the framework of GLM. Various combinations of spectral information based on SSVEP sensor data are constructed to form regressor vectors in asymmetric EEG to fMRI integration process. On the other hand, a direct comparison between the steady state EEG and BOLD activities on a source space was performed by computing the neuronal efficacies and the EEG mean source power values of the voxels that were achieved by solving the fMRI-constrained distributed EEG inverse problem [148]. The SSVEP data that was used in [148] was formed by averaging the (simultaneously recorded) EEG data over the stimulation periods. However, our approach in this study is motivated by a simple yet adequate technique to incorporate the EEG and the fMRI data on a common temporal extent without averaging the EEG data in time. By constructing the EEG sources unimodally with no spatial constraints imposed by the fMRI activity maps, we studied the coupling between the two activities on a common spatial solution space over a common temporal domain. The space we use can be defined as the cortical manifold obtained from the white-gray matter boundary and the temporal domain is sampled with the TR interval of the BOLD signal. Unlike Wan et al., the distributed EEG source maps are reconstructed for both the stimulation and the resting conditions that correspond to each fMRI scan. SSVEP data is projected to source space and energy time series are computed by employing a Bayesian source reconstruction algorithm proposed by Friston et al. [124]. This reconstruction method allows for a design of spatio-temporally optimized filter function which maps the EEG data at the sensor space to the current distribution in the source space. It may optimize the mapping with several spatial and temporal constraints as well as allowing for a computation of EEG source energy defined by a time-frequency constraint. This procedure enabled us to estimate a time series of EEG source energy maps (SEM) having the same spatial and temporal resolution with the fMRI data.

5.3 Asymmetric Temporal Fusion of EEG & fMRI

5.3.1 Localization of Brain activity with BOLD Signal Changes

As a noninvasive tool, fMRI can generate source images of the activity in the brain resulting from sensory stimulation or cognitive function. When neural activity increases in a region of the brain, the local MR signal formed in that part of the brain increases by a small amount (typically only 1-to-several percent of the average image signal intensity) caused by the changes in blood oxygenation. The difference in magnetic properties of oxyhaemoglobin and deoxygenated haemoglobin in blood is the basis of the fMRI studies and the fMRI signal is called as the Blood Oxygeneation Level Dependent signal (BOLD). Functional brain mapping experiments include alternating periods of a stimulus task and a control task. During the implementation of the task/control periods, dynamic echo planar images are collected covering the all or interested part of the brain. After a repetition time (TR), all the images are acquired again. The data structure of the resulting data set is a time series of the *3D* images. The data is further analyzed to extract the areas of activation. The signal time course of each voxel is investigated whether the signal shows a significant change between the stimulus and control periods. Statistical analysis is performed to exhibit the significance of the detected activation [149].

Cardiac, respiratory motions and head movements create signal fluctuations that are observed in the fMRI measurements [150]. Generally, movement effects are corrected with a postprocessing operation after the data collection. The correction is applied using a translation and a rotation operator that align the image with a reference image. The first image of the serie or the average image of the serie can be selected to be the reference image. Physiological and physical processes involved in the generation of an fMRI BOLD signal produce a time-series with correlated noise. To remove these systematic non-BOLD variations is possible by the reduction of the correlation in the noise.

5.3.2 General Linear Modelling

The GLM-based statistical analysis are performed to determine the voxels which are significantly related with the task condition for both the EEG and fMRI data separately. Also, GLM is used in the EEG informed fMRI analysis to reveal voxels (virtual electrodes) whose EEG and fMRI temporal patterns are significantly correlated. The general formalism of the GLM [21] used in this thesis is outlined below.

$$y = X\beta + \epsilon \tag{5.1}$$

where $\epsilon \in N(0, \sigma^2 I)$, X stands for the design matrix which contains the regressors and the confounds. In the framework of this study, y is used for the i)fMRI data and ii)EEG power time series data for each voxel.

For the fMRI case, the BOLD signal includes substantial amounts of low-frequency noise related with the physiological events like breathing and respiratory effects. This low frequency noise is solved by the use of high-pass filtering. High-pass filtering can be applied by adding appropriate columns to the design matrix or the input BOLD can be filtered prior to the estimation step of the β. Generally, a 128 seconds high pass filter is formed with Discrete cosine transform (DCT) set. After forming the design matrix X, $\hat{\beta}$ is computed using ordinary least squares as in Eq.5.2 (estimation OLS).

$$\hat{\beta} = (X^T X)^{-1} X^T y \tag{5.2}$$

The data are serially correlated (temporally autocorrelated) and this violates the assumptions of the noise model in the GLM to be $Cov(e) = \sigma^2 I$.

$$\hat{e} = y - X\hat{\beta} \tag{5.3}$$

A first order AR process (Eq. 5.4 and Eq. 5.5) is adapted to form a matrix for pre-whitening (A) the noise. Multilplying both sides of Eq. 5.1 with A provides (Eq. 5.6)

the error covariance to be spherical.

$$\hat{e}(t) = a\hat{e}(t-1) + \epsilon_t \quad N(0, \sigma^2) \tag{5.4}$$

$$A = \begin{bmatrix} 1 & 0 & 0 & ... & 0 & 0 & 0 \\ -a & 1 & 0 & ... & 0 & 0 & 0 \\ 0 & -a & 0 & ... & 0 & 0 & 0 \\ . & . & . & ... & 0 & 0 & 0 \\ . & . & . & ... & 1 & 0 & 0 \\ 0 & 0 & 0 & ... & -a & 1 & 0 \\ 0 & 0 & 0 & ... & 0 & -a & 1 \end{bmatrix} \tag{5.5}$$

$$Ay = AX\beta + Ae \tag{5.6}$$

After the whitening process, parameters are estimated by using the Eq. 5.7

$$\hat{\beta} = ((AX)^T(AX))^{-1}Ay \tag{5.7}$$

and t statistics based on ML estimates are performed using Eq 5.8.

$$t = \frac{c^T\hat{\beta}}{std(c^T\hat{\beta})} \tag{5.8}$$

where c stands for the contrast vector, $std(c^T\hat{\beta})$ is given in Eq. 5.9 and in Eq. 5.10 and residual matrix R is given in Eq. 5.11.

$$std(c^T\hat{\beta}) = \sqrt{c^T(AX)^\dagger(AX)^{\dagger^T}c} \tag{5.9}$$

$$\sigma^2 = \frac{\sum(Ay - AX\beta)^2}{trace(R)} \tag{5.10}$$

$$R = I - AX(AX)^\dagger \tag{5.11}$$

In the case of fMRI processing, the design matrix contains the stimulus pat-

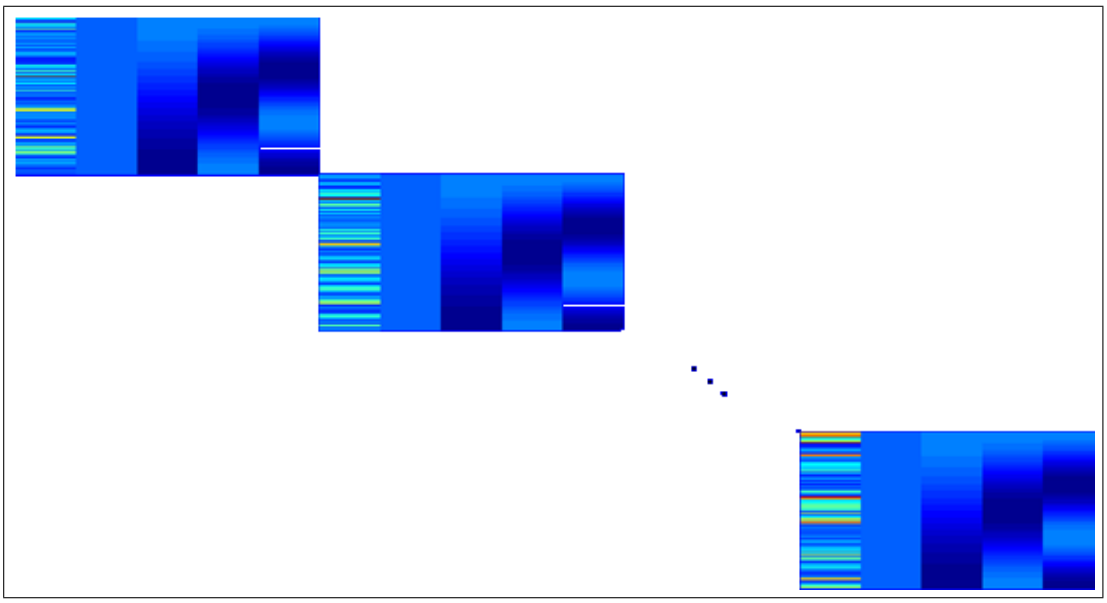

Figure 5.1 A typical design matrix of a voxel for multiple subjects.

tern convolved with the canonical HRF, and its time and dispersion derivatives, and movement confounds. For the unimodal EEG GLM analysis, the distinction is that the stimulus pattern is not convolved with the canonical HRF. On the other hand, for the EEG informed fMRI analysis, an individual design matrix (Fig. 5.1) is formed including the EEG power time series for each voxel.

5.3.3 Simultaneously recorded EEG&fMRI

12 healthy volunteers (6 female, 6 male; mean age 25.8 ± 3.7 years) simultaneously recorded EEG/fMRI steady-state visual responses were studied in this research. The study procedure was approved by the local ethics committee of Istanbul University, Istanbul Faculty of Medicine. Each volunteer is properly informed about the procedure and signed informed consent before the experiment. The volunteers preserved their habitual bedtime in order not to sleep during the experiment.

5.3.3.1 Experimental Setup and Stimulation. The photic stimulus was generated via an electro-magnetically isolated light source with a set of four light-emitting

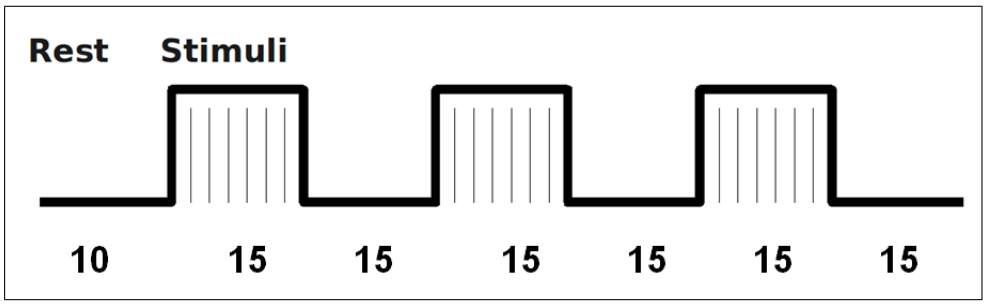

Figure 5.2 Stimulus Paradigm

diodes (LED) and a digital switching circuit. During the application the MR scanner room was kept dim. With the help of the duty cycle set to 50% the energy was kept constant. The light source was placed in one meter distance at the back of the MR. It was set in line with the subject, and controlled by a digital I/O card (National Instruments DAQCard-6062E). In order to determine the "on" and "off" periods of the visual stimuli precisely, external device synchronization output of the MRI scanner was used to trigger the digital I/O card. As a result, the periods of the stimuli are defined in terms of repetition time (TR) parameter of EPI sequence. In order to simultaneously register event markers on the EEG pattern, the signal output of digital I/O card and synchronization output of MRI scanner are connected to the EEG amplifier. The reflection screen, a mirror coated with a semi-transparent paper, was placed over the head coil (field of view 54.8^o), and the subjects were instructed to focus on the fixation cross on this mirror. The frequencies of the stimuli applied vary from 6 to 14 Hz with 2Hz steps. The visual stimulation sequence is created to start with an "off"-period (baseline) with a duration of 10 TR, which is followed by three 15 TR visual stimulation periods, each ending with a 15 TR "off"-period. Each sequence lasted 100 TR (298.1 s), where it took totally 70 minutes. The varying stimulation frequencies were applied in randomly selected order in every experiment. This way, bias of the frequency sequence on the SSVEP and fMRI responses are avoided. During the experiment the volunteers were allowed to rest among sequences with keeping their scan position unchanged.

5.3.3.2 MRI data acquisition. The MR scanning used in this study was a 1.5T MR scanner (Achieva, Philips Healthcare, Best, The Netherlands) with SENSE-Head-8 coil at NPISTANBUL Neuropsychiatry Hospital, Istanbul. In addition to the clinical routine cranial scan, T1-weighted MPRAGE sequence (voxel size 1.25/1.25/1.2 mm; 130 slices; and field of view 240 mm) were performed for high resolution anatomical images for each subject. Following the structural scans, each subject was scanned with MR compatible EEG caps about 20 minutes. The parameters of the BOLD scan comprised a dynamic $T2*$-weighted gradient echo (GE) echo planar imaging (EPI) sequence with 100 dynamics, and two additional dynamics were used for steady state purposes of tissue magnetization. AC-PC aligned 32 axial slices with slice thickness of 4 mm without gap and a field of view of 230×230 mm (matrix $= 64 \times 64$ voxel) covering the whole cerebrum were acquired as functional EPI volumes. The EPI sequence has a repetition time (TR) of 2981 ms and echo time (TE) of 50 ms. The TR time is specifically chosen not to fit a multiple of the period of any stimulation frequency. This aims the avoidance of the phase-locking of the residual MR gradient artifacts in the EEG with the visual stimuli.

5.3.3.3 EEG data acquisition. Simultaneous recording was taken via an MR compatible EEG amplifier (BrainAmp MR+, Brain Products, Germany) with 30 channels EEG (extended 10/20 system) and 1 channel ECG. The EEG signal filtered between 0.01 and 250 Hz was digitized with a sampling rate of 5 kHz. A hardware (Synch-Box, Brain Products, Germany) was used for synchronization of the MR scanner clocks and the EEG digitizer. This maintains the MR gradient artifacts to appear as constant waveforms in the EEG pattern. Those gradient artifacts were substracted based on the Average Artifact Subtraction (AAS) method [151] using the Brain Analyzer software (Brain Products, Germany). Following this removal, also the ballistocardiographic (BCG) artifacts were substracted with a method which relies on an average template of the BCG artifact using the timing of the R wave in the ECG trace. Finally, the eye and muscle artifacts were removed manually, and the EEG was down-sampled to 1kHz.

5.3.4 General Analysis Scheme

Simultaneously recorded SSVEP and fMRI data were registered to a common spatio-temporal space in order to perform a voxel by voxel fixed effect GLM analysis. The common domain for temporal scale was selected as the number of the fMRI scans and cortical surface was selected for the spatial scale. SSVEP data were projected to the source space and the EEG SEMs were computed at each time window for a duration of TR seconds. The fMRI data were sampled on the cortical surface to match the spatial domain of the SSVEP SEMs. In this way, two sets of neuronal data ($n_{vertice} \times n_{scans}$), containing the BOLD and the SSVEP SEM values were obtained. Finally, the dataset of each subject (12 subjects) was concatenated to perform the fixed effect analyses.

Spatial activation patterns were determined by applying fixed effect GLM analysis to each dataset for every stimulation frequency. The fixed effect design matrix for fMRI analysis consists of a basic boxcar model convolved with a canonical HRF and its temporal derivatives. For the SSVEP SEM data, the design matrix for the GLM analysis was formed by the same basic boxcar signal. SPMs of activation regions were obtained by testing for positive BOLD and SEM changes using corrected $p < 0.05$ threshold. Finally, EEG informed fMRI analysis (asymmetric fusion) is computed in order to express the relation between the BOLD & EEG source time series in a woxel-wise manner. This temporal asymmetric fusion process required a separate (individual) design matrix for each voxel. The details of this procedure are explained under the following sub-headings.

5.3.5 EEG data analysis & source energy maps

For a given predefined set of dipole source positions, orientations and strengths, scalp potentials are computed using the Boundary Element Method (BEM) with the Center of Gravity (COG) approach at a finite set of electrode locations on a realistic head model [66, 29]. The realistic human head is modeled based on the MNI anatomy and composed of three homogeneous isotropic conductor boundaries representing the

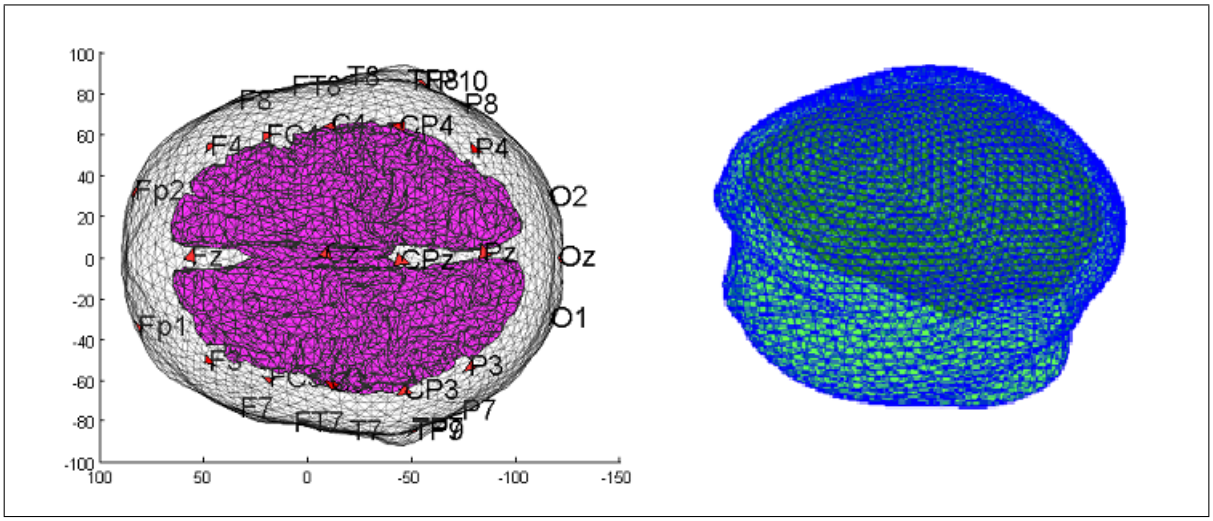

Figure 5.3 The locations of the sensors are marked with associated labels. The scalp surface, canonical cortical surface (left) and the scalp, inner skull surfaces (right) of the realistic head model are plotted.

scalp, outer skull and the inner skull, respectively. The vertices forming the cortical mesh of the brain is used as source space. The triangulated boundaries forming the head model that we used in this study is obtained using the SPM8 library [152] as shown in Fig. 5.3.

30 electrode locations are registered to the scalp surface by spline interpolation using the 10-20 electrode placement, inion-nasion and pre-auricular coordinates. Forward problem is solved to compute the lead field matrix H, using the 5124 (n_s) vertex points of the segmented cortical mesh on which the current dipoles are oriented normal to the cortical surface. Thus, each vertex of the cortical mesh acted as a virtual (intra-cortical) electrode [22].

The squared norm of the response projected onto the subspace (W) is computed and assigned as the energy (power) of the corresponding time (volume) indice for each vertice. Time frequency matrix (W) is formed by using a set of sine−cosine pair of sinusoids associated with the interested frequency band (w) and its two harmonics as shown in Fig. 5.4 (Eq.5.13).

$$W = [\sin(wt);\ \cos(wt);\ \sin(2wt);\ \cos(2wt);\ \sin(3wt);\ \cos(3wt)]^T \qquad (5.12)$$
$$t = [0 : 2\pi/(nt-1) : 2\pi]$$

The EEG source reconstruction methodology based on empirical Bayesian approach, [153] enabled us to compute the source energy within a given frequency band. The EEG/fMRI integration approach that we use in this study is based on determining the spatial regions whose source energy is temporally correlated with the steady state BOLD response. Several combinations of spectral power are computed based on SSVEP data which can explain the signal changes in BOLD time series [147, 148]. This leads us to obtain an exploratory variable that can be used to explain the BOLD signal by summing the power of the SSVEP signal at the stimulation frequency and its first 2 harmonics. The SEMs are computed for each 1s time block of the SSVEP data using Eq.5.13

$$SEM_{i,st}(t) = \sum_{f=1}^{3} \hat{E}(i, t, st \times f) \quad i = 1:1:5124 \qquad (5.13)$$

where $SEM_{i,st}(t)$ denoted the source energy map value at the $i.th$ source location of stimulation frequency st. t is the time index and $\hat{E}$ stands for the source energy operator. SSVEP SEMs are in temporal alignment with the the measured BOLD time series at all stimulation frequencies (6Hz, 8Hz, 10 Hz, 12Hz, 14Hz) without loss of information in EEG.

5.3.6 EEG & fMRI processing

fMRI data is pre-processed prior to performing GLM analysis. Motion correction, slice timing correction, spatial smoothing using a Gaussian kernel of FWHM 8.0 mm, grand-mean intensity normalization of the entire 4D dataset and highpass filtering are applied. All images are spatially normalized into a standard space (MNI152, 2mm) [152]. Then, fMRI data is projected from voxel-space to the cortical source space by

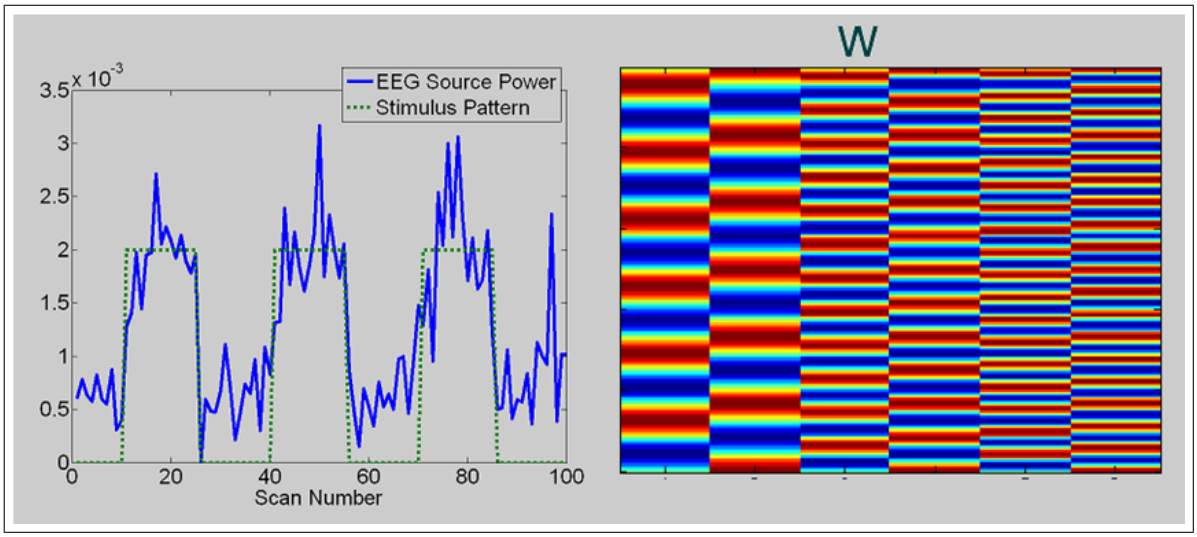

Figure 5.4 Left: Stimulus pattern is shown in green color. A power time course of a voxel choosen from the occipital lobe is plotted with blue color. Rigt: The structure of the W matrix for 6Hz stimulation frequency. The design matrix includes the 3 sets of sine-cosine columns for 6 Hz, 12Hz and 18 Hz.

sampling/averaging along the normal of each vertex from the inner (white matter/gray matter) to the outer (grey matter/CSF) boundary, and the average BOLD value is assigned to corresponding vertex. This process enabled us to perform fMRI and EEG data modelling and analysis in the same cortical source space. Spatial regions regarding to the stimulus paradigm are identified by applying fixed effect (12 subjects) GLM analysis [154] separately to fMRI and SSVEP SEM maps for each stimulation frequency. GLM time series analysis with local autocorrelation correction is used to find BOLD related signal changes devoting the visual stimulation periods from the rest periods [155]. The design matrix is formed to include the basic boxcar model convolved with a canonical HRF and its temporal derivative. Apart from this, SEM time series with local autocorrelation correction is used to find EEG source power related signal changes discriminating the visual stimulation periods from the rest periods. For this process, only basic boxcar model is used in the design matrix. Statistical parameter maps (SPMs) of activation regions are obtained by testing for positive BOLD and SEM changes using corrected $p<0.05$ threshold.

5.3.7 EEG informed fMRI processing

The common spatial region of the thresholded SEM-SPMs and fMRI-SPMs are guaranteed to be significantly correlated with the stimulus temporal pattern (fixed effect GLM analysis, $p<0.05$) although they correspond to different physiological events. To investigate the relationship between the temporal patterns of the SEM and BOLD signals, a fixed effect SEM informed fMRI analyses is performed for each source forming the spatial intersection regions

$$fMRI_j = X_j\beta + \epsilon, \quad j \in (SPMoffMRI \bigcap SPMofSEM) \tag{5.14}$$

$$\begin{bmatrix} fMRI_j(1) \\ fMRI_j(2) \\ \vdots \\ fMRI_j(100) \end{bmatrix} = \begin{bmatrix} SEM_{j,st}(1) & 1 \\ SEM_{j,st}(2) & 1 \\ \vdots & \vdots \\ SEM_{i,st}(100) & 1 \end{bmatrix} \begin{bmatrix} \beta_1 \\ \beta_2 \end{bmatrix} + \begin{bmatrix} \epsilon_1 \\ \epsilon_2 \\ \vdots \\ \epsilon_{100} \end{bmatrix} \tag{5.15}$$

where X_j is the design matrix of $j.th$ source that contains the mean corrected SEM_j convolved with canonical HRF and a vector of ones as shown in Eq. 5.15. β values of the sources are estimated by linear least squares after the high pass filtering and prewhitening (AR(1) model) operations. For each voxel, a different design matrix was produced. The SEM informed fMRI activated regions were determined by estimating the correlation of the SEM signal with the BOLD using an appropriate contrast in a source-wise Student's t-test. This process was repeated for each stimulation frequency separately. SEM informed fMRI analysis ensured that the active regions were correlated with the stimulus paradigm both electrophysiologically and hemodynamically. This can alleviate the bias which may possibly arise from the asymmetrical way of predicting one signal in terms of the other. More specifically, those regions which did not exhibit significant activation both electrophysiologically and hemodynamically but indicating a significant correlation between each other, were automatically eliminated.

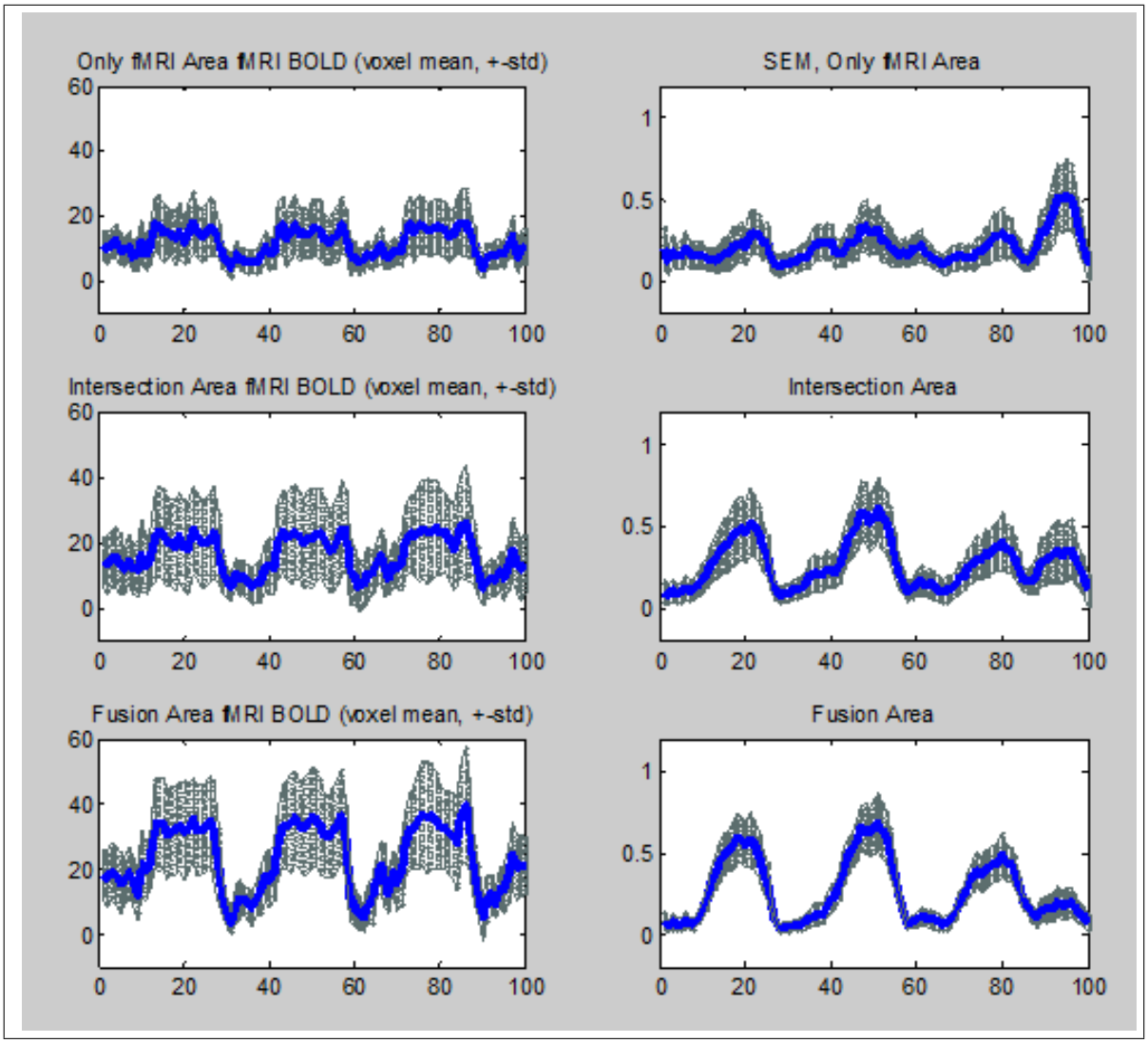

Figure 5.5 The BOLD and SSVEP time series of the voxels for a single subject that are deduced from the fixed effect unimodal GLM analysis of 12 subjects for the 8Hz stimulation frequency. The plots are drawn for three cases; i) The area in which only BOLD activation exist, ii) The intersection area of BOLD and EEG activation, iii) The fusion area where the source energy time series of the voxels are significantly corellated with the BOLD

5.4 Results

Unimodal fixed effect analysis of BOLD time series for each stimulus frequency yielded significant activations in the occipital lobe especially in the primary (BA17), secondary visual areas (BA18, BA19) and lingual gyrus. The extent of the fMRI activation maps were approximately similar for all stimulation frequencies (Fig. 5.8, Fig. 5.9). The illustration in Fig. 5.6 depicts the activated regions for 8Hz stimulus frequency ($p < 0.05$, corrected).

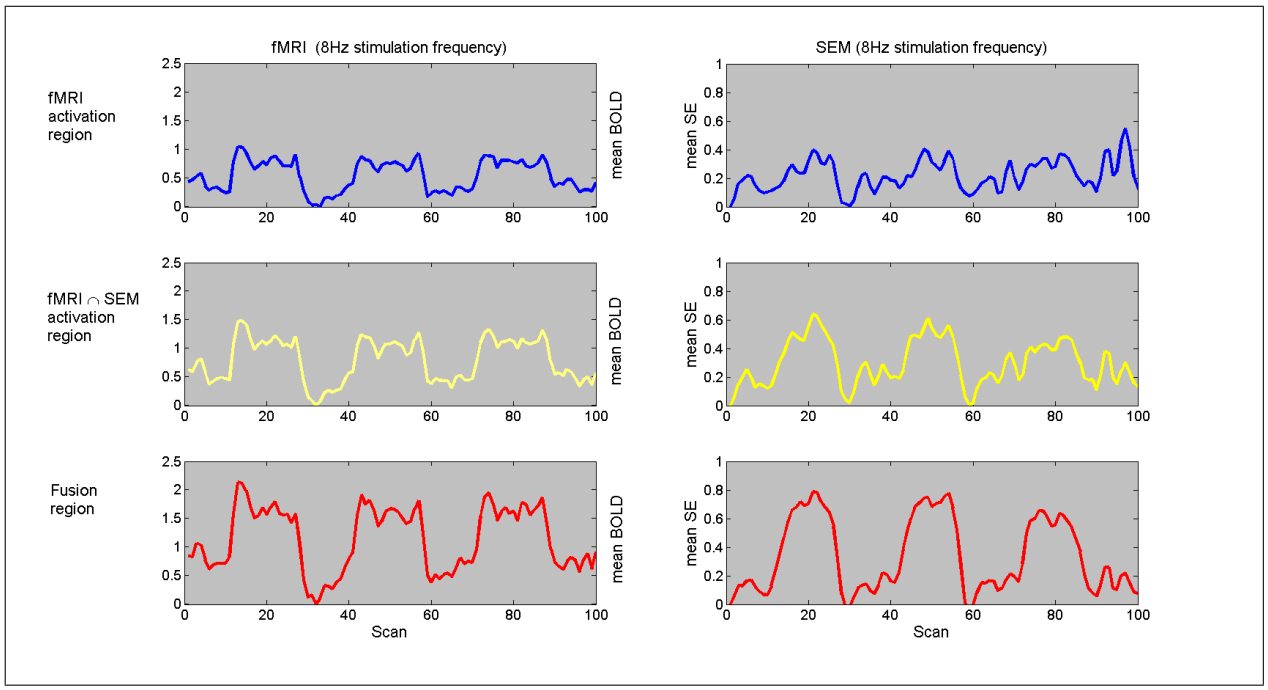

Figure 5.6 fMRI BOLD (left column) and SEM_f (right column) mean voxel signal intensity time series presented for three cases regarding to $8Hz$ stimulation frequency; (first row) i) The map obtained from the fixed effect SEM_{8Hz} analysis using the contrast that compares the visual stimulation periods with the rest periods (t-test, $p < 0.05$) is excluded from the fMRI map exhibited by the similar analysis ($p < 0.05$). The resulting map consists of the voxels whose BOLD responses are correlated with the stimulus paradigm unlike the SEM_{8Hz} time series. ii) The maps of the fixed effect SEM and BOLD analysis ($p < 0.05$) are spatially intersected to figure out the voxels whose BOLD and SEM_{8Hz} time series are correlated with the stimulus temporal pattern. iii) Fusion region is obtained via the SEM_{8Hz} informed fMRI BOLD series analysis which is computed for each voxel of the intersection map. Significant temporal correlation values between BOLD and SEM_{8Hz} (HRF convolved) time series of these voxels are observed for this fusion region.

The power of the alpha, beta and gamma bands excluding the power at the stimulation frequency and at its first 2 harmonics were also computed to test the possible indirect effects of the stimulation on SEMs of the background. No significant activity change in response was obtained by the unimodal fixed effect SPM analysis of these SEM signals in the alpha, beta, gamma range. On the other hand, SPM analysis of SEM_f for each stimulus frequency exhibited significant increase of activation in stimulation blocks mainly localized in the primary and secondary visual cortices near the surface. All of these SEM_f activations were observed as spatial subsets of the activation maps obtained from the corresponding fMRI time series. The computed source patterns of SSVEPs (Fig. 5.7, Fig. 5.8, Fig. 5.9, $p < 0.05$) are in agreement with the previous findings [156, 157, 158].

The spatial intersection of these $fMRI - SEM_f$ activation maps revealed the common areas which were correlated with the stimulus boxcar pattern independent of the measurement modality. The spatial intersection of these $fMRI - SEM_f$ maps were further used as a mask for the SEM_f informed fMRI analysis. An individual design matrix was formed for each voxel on the intersection area by using the SSVEP SEM_f time series as an exploratory variable to explain the BOLD signal and the relation between the two activities were investigated with a fixed effect GLM analysis. SEM_f informed fMRI analysis yielded focal activation maps localized in the $BA17, 18, 19$ for each stimulation frequency. In sum, the analyses constituted three spatial activation patterns; i) the spatial region in which only BOLD time series were correlated with the stimulus paradigm, ii) the spatial region in which SEM_fs were correlated with the stimulus paradigm. Because all SEM_fs were spatial subsets of the BOLD activation maps, these correspond to the intersection of BOLD activation maps and SEMs, iii) the fusion maps which directly exhibited the temporal correlation between the BOLD and SEM_f time series within the intersection maps. The fusion maps constituted by the voxels whose SEM_f time series were positively correlated with the corresponding BOLD time series within the intersection maps were obtained by the fixed effect analysis (corrected, $p < 0.05$) for each stimulation frequency. Fig. 5.7 displays the locations of the voxels that correspond to the above activation cases for the 8Hz stimulation frequency. Corresponding time series that are obtained by averaging over the subjects across the voxels are shown in Fig. 5.6.

The mean percent BOLD and SEM_f signal intensity changes of the voxels that constituted these fusion maps were computed for the three consecutive stimulation blocks and averaged over 12 subjects. On these fusion activation maps it was observed that the maximum of the mean percent BOLD signal intensity change was at 12 Hz stimulation frequency while the maximum for the mean SEM_f change was at 8Hz.

For a comparison of the results obtained at the source space with the conventional SSVEP measurements on the scalp, the sum of the spectral peaks at the stimulation frequency and its first and second harmonics of the mean scalp SSVEP signal at the O1, Oz, O2 channels at 5 visual stimulation frequencies were calculated by

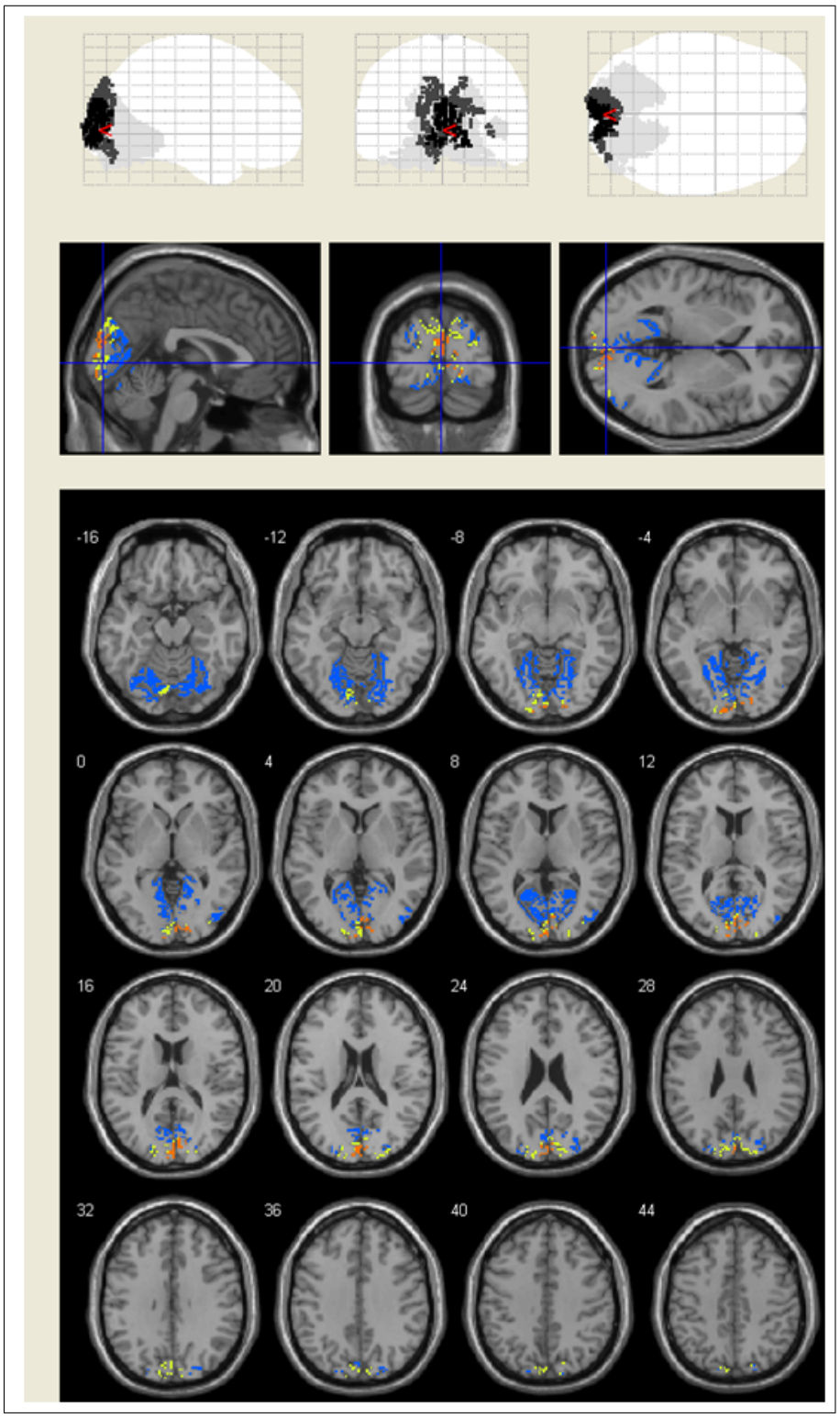

Figure 5.7 The activation patterns for 8Hz stimulus frequency are plotted; (first row) The activated locations are represented on a glass brain in three orthogonal planes. The lighter gray, gray and black color codes denote the; fMRI activation region, spatial intersection of fMRI and SEM_f activation maps and fusion activation, respectively ($p < 0.05$). (second row) The activation patterns are overlaid on anatomical T1 weighted MNI template image with the color blue for fMRI activation region, yellow for spatial intersection of fMRI and SEM_f activation maps and red for the fusion activation. (third row) The activation patterns are overlaid on transversal anatomical T1 slices. The fMRI activation results are masked with the locations of the cortical mesh vertices prior to the representation and computation of the percent pBOLD intensity features.

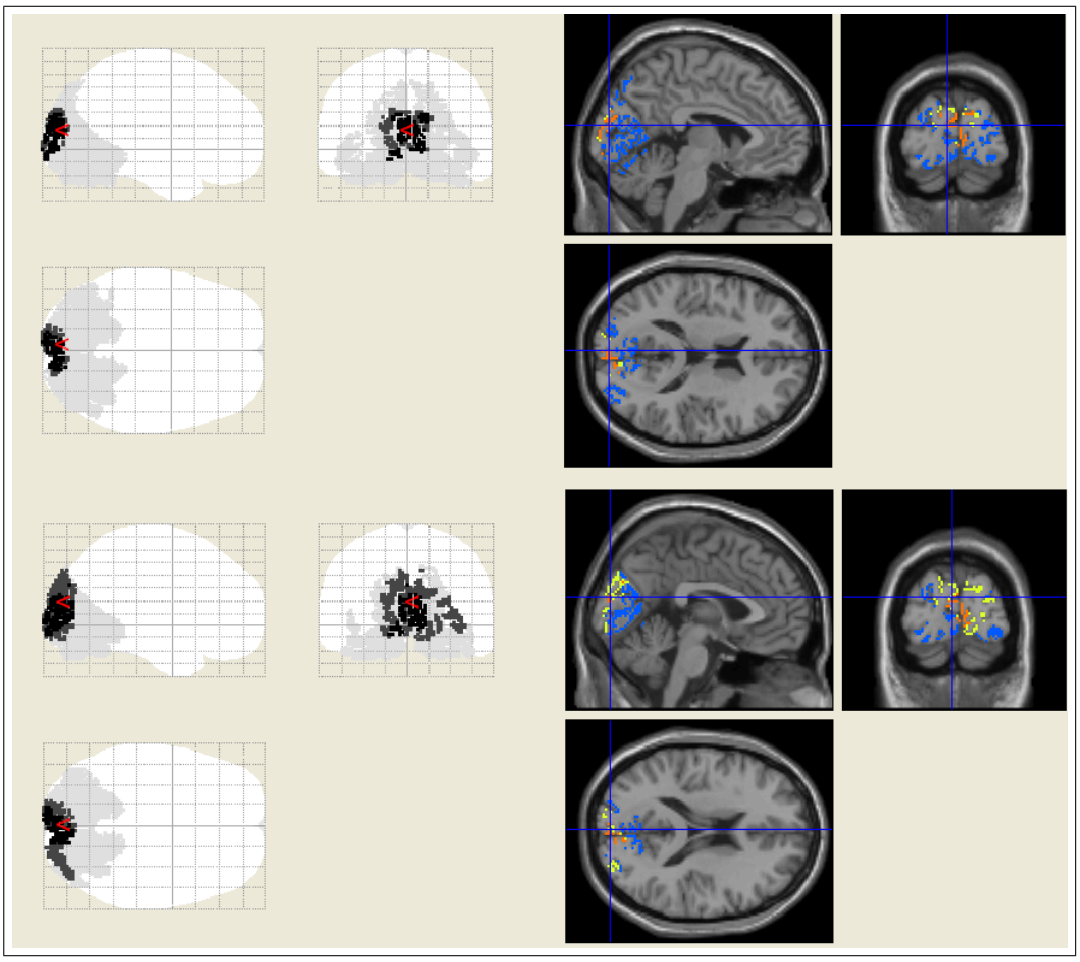

Figure 5.8 The activation patterns for 6Hz (top) and 10Hz (bottom) stimulus frequencies are plotted. The activated locations are represented on a glass brain in three orthogonal planes. The lighter gray, gray and black color codes denote the; fMRI activation region, spatial intersection of fMRI and SEM_f activation maps and fusion activation, respectively ($p < 0.05$).

computing the magnitudes of the Fast Fourier Transforms (FFT) of the SSVEP signals averaged over 1 s time-windows. Mean amplitudes of the time-averaged scalp SSVEPs had the maximum value at 8Hz stimulation frequency in line with the maximum of the SEM_f signal intensity change.

5.5 Discussion and Conclusion

In this study, the EEG informed fMRI analysis was performed using the maps that were obtained by intersecting the unimodal EEG activation maps with the unimodal fMRI maps. Instead of using the conventional time-averaged SSVEP data, we

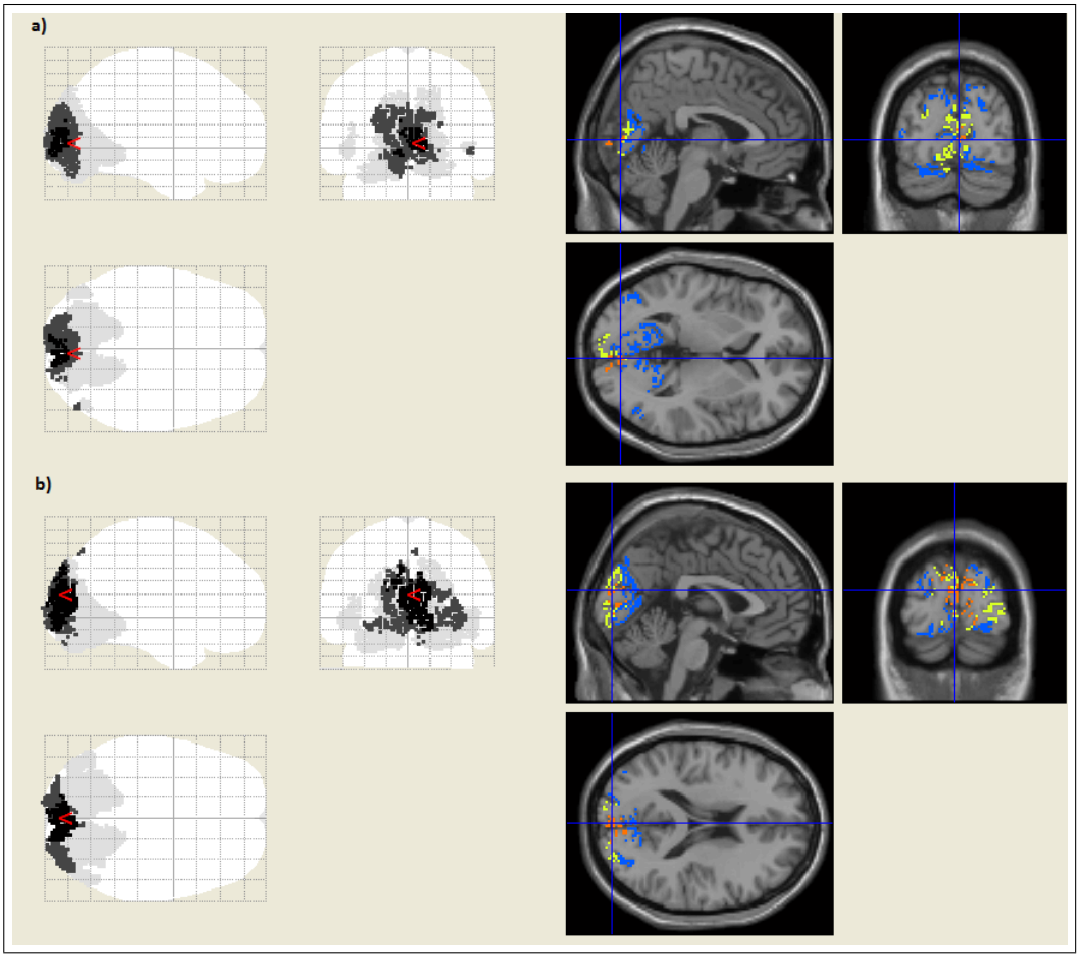

Figure 5.9 The activation patterns for 12Hz (top) and 14Hz (bottom) stimulus frequencies are plotted. The activated locations are represented on a glass brain in three orthogonal planes. The lighter gray, gray and black color codes denote the; fMRI activation region, spatial intersection of fMRI and SEM_f activation maps and fusion activation, respectively ($p < 0.05$).

computed the SSVEP source energy maps by determining the voxels showing a significant change in the EEG source power at the stimulation frequency and its first two harmonics during the stimulation period with respect to the rest. Thus, the voxels of the intersection maps were guaranteed to produce significant electrophysiological and hemodynamic responses. However, it is not always the case that the EEG and hemodynamic responses coexist at a meaningful level within a certain brain spot. We observed this fact through the standard unimodal analysis of both the EEG and the fMRI data as the SSVEP source energy maps existed in a region which was always a subset of the BOLD activity maps. This indicates that a hemodynamic activity change does not necessarily need to generate an SSVEP activity. One of the well-known explanations of such an incongruity between the far-field electrical potentials measured in EEG and the local neuronal activity is the presence of a spherically symmetric dendritic current distribution (close field) and relatively remote sources located in the deep structures that do not significantly contribute to the scalp EEG. However, as our solution space is limited to the cortex, where the apical dendrites of the pyramidal neurons build an open field, the above two factors cannot explain the missing contribution of the cortical regions with a significant BOLD activity to the EEG. Apart from the close field possibility, another plausible explanation of such incongruity between the local neuronal activity and the far-field EEG signals is the synchronization within and among voxels. Local electrical activity that contributes to the scalp recorded EEG requires a certain level of synchronization of post-synaptic activity among the neurons within a voxel in addition to a synchronization among a large set of voxels. However, we can claim that, as long as there exists a neural activity within a voxel, we observe a significant BOLD signal change irrespective from such a synchronization [131]. Contrarily, a moderate level of neuronal response which enterprises a high synchronization among a population may produce significant EEG without a noticable BOLD change due to its minor hemodynamic demand. In earlier studies, the presence of a synchronous high voltage spontaneous alpha rhythm has been reported to be associated with the decrease of the BOLD signal of the occipital cortex below the level it occurred during low amplitude occipital EEG [20, 19]. A possible cause of this observation might be that the neuronal activity responsible for the alpha synchronization is not only existing in the cortex but partly located in a subcortical structure such as thalamus. On the other hand,

non-synchronized occipital EEG relies on a relatively higher level of cortical activation which requires a relatively higher BOLD activity. Our findings did not show such incongruity between the SSVEP and BOLD activity maps for the stimulation frequencies we studied. The SSVEP source energy maps were always observed as the spatial subsets of the corresponding fMRI BOLD maps. This indicates that the evoked EEG rhythms in contrast to the spontaneous ones always necessitate a cortical metabolic demand. This further indicates that there exist voxels with a high BOLD signal change which do not contribute to the SSVEP response (Fig. 5.6). These voxels are the ones which have an electrical activity pattern that does not correlate with the stimulation but yield a moderate level of BOLD response correlated with the stimulation. Our voxel-wise EEG informed fMRI fusion analysis yields a relatively small group of voxels that exhibit a strong resemblance between the EEG and the fMRI responses. Interestingly, these voxels show the highest EEG and fMRI amplitude changes due to stimulation although their spatial extent is rather minimal. There exist some other voxels whose EEG and fMRI responses are correlated with the stimulation but the former can not predict the latter. These voxels, which are outside the fusion area but which coexist in unimodal fMRI and EEG analyses, show a relatively lower amplitude of EEG and fMRI responses compared with those of the fusion area voxels.

In the analyses of the time averaged SSVEPs, absolute amplitudes of evoked potentials are taken into account while the amplitude increase from the rest periods are ignored. However, there is no such shortcoming in our source space GLM analysis since it eliminates the absolute intensity of the baseline activity and captures its change.

As pointed out in [159], the symmetric fusion tools originated from the need to overcome the limitations of asymmetric approaches, but one should not be overconfident about their optimality against the asymmetrical approaches for EEG-fMRI integration. The asymmetrical approaches can still answer a great many questions about the common behaviour of the EEG and fMRI. The simplicity of their assumptions makes them attractive to capture the neurovascular dynamics behind the EEG-fMRI data. As the SSVEP source energy maps obtained by using the power of the EEG at the stimulation frequency and its first two harmonics were used in the present analyses

instead of the time-averaged SSVEP data, this result reveals that both the evoked and induced oscillations in the visual cortex elicited by the stimulations necessitate a metabolic demand.

6. General Summary and Conclusion

New signal modeling techniques are important to study the spatio-temporal properties of the brain activity measurements as the EEG, ERP and fMRI. Integration of data on different temporal and/or spatial scales may open up new vistas for the functional neuroimaging of the brain. This problem is addressed in three different ways here. The first one is a decomposition whereas the other two are integration of functional Neuroimaging data coming from different scales, domains or modalities. The first approach which aims wavelet analysis followed by source imaging of scalp EEG is a decomposition of the brain activity into different spatial and temporal scales. The second approach aims for the integration of EEG data on different scales for epileptic source imaging. Finally, the third approach is an integration of data coming from two different modalities to perform neuroimaging of brain activity under steady state stimulation.

In Chapter 3, the spatio-temporal decomposition of EEG topographies is implemented using two different approaches; i) radial basis functions and ii) wavelet decomposition. The proposed and implemented decomposition methods decompose the topographies into simpler maps by assuming that the EEG topographies are formed by the superimposition of simpler topographies. This procedure enables us to apply the source localization procedures to the simpler topographies. Radial basis functions are used as kernel functions in order to explain the EEG topographies with simpler subtopographies. The simulation results are given in Fig. 3.3 and the corresponding source maps are shown in Fig. 3.4. The localization results are in agreement with the simulation source parameters.

As pre-processing tools, time-frequency [97] analysis and spatial decomposition [13] procedures are used prior to the source localization. The main objective of Chapter 3 is to show that the complex EEG topographies can be expressed as the summation of the subtopographies having different spatio-temporal frequency characteristics by the

use of combined time-frequency and spatial decomposition methods on the realistic scalp models. *1D* discrete wavelet transform is implemented on *3D* cartesian space as spatial filters that decompose the topographies into subtopographies. By the use of this technique, the complex scalp EEG topographies are split into simpler topographies (subtopography) whose summation yields the original complex topography. The technique is implemented on a realistic head model derived from the anatomical MR images. Because of the complexity of the *3D* spatial wavelet decomposition, a more efficient version of the method on the realistic head models is developed which uses the contorted and flattened realistic scalp model. The proposed spatial decomposition techniques are applied to the simulated datasets. These datasets include the topographies that are generated by two or more distinct sources which cannot be accurately localized by the use of parametric inverse solutions. The original source locations of the simulated dataset are estimated without any source localization error after the implementation of the developed spatio-temporal decomposition.

In Chapter 3, this technique is applied on the ERPs that are collected from 24 subjects using the Go and NoGo CPT paradigms. The ERPs are averaged over the subjects and spatio-temporal wavelet decomposition process is applied for each paradigm. The resulting subtopographies are further source localized and it is seen that additional information is gathered through the source localization of the subtopographies instead of using the raw ERPs.

As a result, it is observed that temporal wavelet analysis of EEG at a given spatial location yields temporally stationary components at temporal frequency bands like delta, theta, alpha. Spatial wavelet analysis of EEG at a given temporal location yields spatially stationary scalp maps at spatial frequency bands. The characteristics of these maps are determined by the depth and extension of individual EEG sources. A spatio-temporal preprocessing of the EEG simplifies the complexity of the scalp map by separating it into several submaps each of which is produced by an individual EEG source. This is a very convenient preprocessing prior to source localization for the isolation of different maps corresponding to different dipole sources. This way, even the temporally correlated EEG sources can be localized after spatio-temporal

decomposition of EEG.

In Chapter 4, various source reconstruction algorithms are performed on the clinical epilepsy datasets. Both, the parametric and linear inverse solution methodologies are implemented using the invasive and non-invasive EEG recordings. RAP-MUSIC method is used for the parametric solution while LORETA and Bayesian source reconstruction methods are applied for the linear case. The scalp measurement inverse solution accuracy is analyzed using the reference information obtained through the invasive recordings. In a previous study, the correlation between the cortical reconstructed EEG and subdural measurements of a subject was found as 0.79 [160]. Similarly, in our case, correlation coefficient values varying from 0.72 to 0.84 were computed between the preictal seizure time series of the deep electrodes and the source reconstructed time series at the same sites.

In the pre-operative period, the results obtained by the scalp EEG seizure localization may lead us to decide about the number and the positions of the invasive electrodes. Thus, the non-invasive measurements should be carefully analyzed to use as a prior information for further invasive studies.

The spatial resolution of the EEG inverse solution is limited while it has a high temporal resolution. This spatial limitation can be improved with the use of multimodal functional neuroimaging measurements such as EEG&fMRI. In Chapter 5, an EEG&fMRI information integration (fusion) method is proposed that allows the investigation of the brain activity using the simultaneously measured EEG&fMRI data. The steady state paradigms which are used to reflect oscillatory EEG patterns that can be stationary for the time period of the BOLD signal, are adopted for the simultaneous measurements. EEG&fMRI data is collected from 12 subjects under five different stimuli. For the EEG&fMRI fusion process, a common spatio-temporal domain is formed and the multimodal data is tranformed to this domain. The spatial part of this domain is selected as the cortical manifold on which the source localization procedure is implemented. Therefore, the measured scalp potentials are projected to the cortex. The voxel-wide fMRI measurements are sampled on the same cortical

surface which enabled us the spatial registration of the both activity.

The temporal resolution of the fMRI is based on the HRF that varies between 10-20 seconds while it is much faster for the EEG. The temporal registration of spontaneous EEG measurements with the BOLD signal should be solved without any loss of information. To overcome this problem, the SSVEP source energy power values of the cortical manifold are computed for each sequential temporal window with TR duration. Thus, a volumetric source energy time series is achieved having the same dimensions with the fMRI measurements.

As a conventional statistical fMRI analysis technique, General Linear Modeling (GLM) is adopted for the voxel time series obtained from the EEG inverse solution. Separate GLM analyses are performed for spatio-temporally registered EEG and BOLD for five visual stimuli having different stimulus frequencies. Statistical parameter maps (SPMs) are obtained using appropriate contrast vectors for each stimulus. Moreover, a similar technique is implemented for the voxel-wise EEG informed fMRI analysis. The novelty of the implemented fusion method (asymmetric temporal fusion) is that a unique design matrix is individually formed for each source volume in the solution space. After the parameter estimation of the design matrix, SPMs are estimated containing the temporal EEG&fMRI correlation information for each stimulation frequency.

It is observed that the summation of EEG source energy of the stimulation frequency and its two harmonics is sufficient to express the stimulus paradigm for some of the voxels mainly localized in the occipital regions. On the other hand, it is shown that, when the stimulation frequency and its two harmonics are excluded, the source energy time series corresponding to the other frequency bands namely beta, theta, alpha and gamma, are not adequate to follow the temporal pattern of the stimulus paradigm. Moreover, the results of the statistical fixed effect GLM analysis indicate that the EEG sources of the SSVEPs are the spatial subsets of the corresponding fMRI maps for each stimulation frequency (RFT corrected, $p < 0.05$). It is also observed that none of the voxels are negatively correlated with the BOLD.

We developed here new signal modeling and analysis methods that would exploit the spatio-temporal nature of the EEG data obtained in various clinical and physiological settings. This is expected to improve the technical capabilities of Neuroimaging in multimodal image fusion, dipole source imaging and functional decomposition of brain electrical activity. There is no doubt that these technical improvements have a strong potential to be used in theoretical areas studying cognition, attention, memory, perception and connectivity. There is also a room for application in practical areas as brain computer interfacing, neurosurgical planning, neuro-psychological diagnosis of certain disorders, monitoring their progress and assessing their therapy. Certainly, the methods proposed in the thesis are merely demonstrations of the applicability and potential of these spatio-temporal methods. There is yet to be done to apply these tools to various cognitive and neurological data to show their broader applicability in Neuroimaging.

APPENDIX A. The Appendices A-D offer the list of publications originated from the of Ph.D. dissertation study.

A.1 Publications in Journals

1. Simultaneous EEG/fMRI analysis of the resonance phenomena in steady-state visual evoked responses.
   Bayram, A. Bayraktaroglu, Z. Karahan, E. Erdogan, B. Bilgic, B. Ozker, M. Kasikci, I. **Duru, A. D.**Ademoglu, A. Oztürk, C. Arikan, K. Tarhan, N. Demiralp, T. Clinical EEG and neuroscience, 2011, 42:2, pp98–106 (SCIE)

2. Analysis of brain electrical topography by spatio-temporal wavelet decomposition **Adil Deniz Duru**, Ademoglu A,Demiralp T., Mathematical and Computer Modelling 49 (2009) 2224:2235 (SCIE)

3. Epilectic Source Localization: Deep Electrode Measurements versus Scalp EEG **Adil Deniz Duru**, Ahmet Ademoglu, International Journal of Bioelectromagnetism, Vol. 11, No. 4, pp175–178, 2009

A.2 Publications in Books

1. Temel ve Uygulamali Kognitif Nörobilimler Ders Kitabi
   EEG Bilesenlerinin Dalgacik Onisleme ve Dipol Kaynak Yerellestirimi ile Goruntulenmesi
   Adil Deniz Duru, Prof.Dr. Ahmet Ademoglu, Bogaziçi Üniversitesi, Biyomedikal Mühendisligi
   Prof. Dr. Tamer Demiralp, Istanbul Hastanesi, Fizyoloji

2. Source Localization of Subtopographic Brain Maps for Event Related Potentials (ERP)

Adil Deniz Duru, Ali Bayram, Tamer Demiralp, Ahmet Ademoglu
ENCYCLOPAEDIA OF HEALTHCARE INFORMATION SYSTEMS
Volume III, pp: 1247-1252

3. Source Localization of Subtopographies Decomposed by Radial Basis Functions
Adil Deniz Duru, Ahmet Ademoğlu
Medical Imaging and Augmented Reality, Lecture Notes in Computer Science
0302-9743 (Print) 1611-3349 (Online)2008
Volume 5128 pp 108-115

A.3 Conference Proceeding Papers

1. Duru, A.D.; Erdogan, S.B.; Kasikci, I.; Bayram, A.; Ademoglu, A.; Demiralp, T.; , "Investigaton of the neuronal efficacy and EEG source power under steady-state visual stimulation," Engineering in Medicine and Biology Society,EMBC, 2011 Annual International Conference of the IEEE , vol., no., pp.6576-6579, Aug. 30 2011-Sept. 3 2011 doi: 10.1109/IEMBS.2011.6091622

2. Implementation of Low Resolution Electro-Magnetic Tomography with fMRI Statistical Maps on Realistic Head Models
Adil Deniz Duru, Hamdi Eryilmaz, Uzay Emir, Zubeyir Bayraktaroglu, Tamer Demiralp and Ahmet Ademoglu
Proceedings of the 29th Annual International Conference of the IEEE EMBS City Internationale, Lyon, France August 23-26, 2007, pp 5239-5242

3. Neuroimaging of Event Related Brain Potentials (ERP) using fMRI and Dipole Source Reconstruction
H. Hamdi Eryilmaz, **Adil Deniz Duru**, Burak Parlak, Ahmet Ademoglu and Tamer Demiralp
Proceedings of the 29th Annual International Conference of the IEEE EMBS

City Internationale, Lyon, France August 23-26, 2007, pp 3384-3387

4. Bayesian EEG Dipole Source Localization using SA-RJMCMC on Realistic Head Model
   Gokcen Yildiz,**A.Deniz Duru**, Ahmet Ademoglu and Tamer Demiralp
   Proceedings of the 29th Annual International Conference of the IEEE EMBS City Internationale, Lyon, France August 23-26, 2007, pp 4268-4272

5. Source Localization of Subtopographic Brain Maps for Event Related Potentials (ERP)
   Adil Deniz Duru, Ali Bayram, Tamer Demiralp and Ahmet Ademoglu
   Proceedings of the 28th IEEE EMBS Annual International Conference New York City, USA, Aug 30-Sept 3, 2006 Pp 4832-4834

6. Coregistration of fNIRS Data on to the Realistic Head Model
   Uzay Emrah Emir, **Adil Deniz Duru**, Ahmet Ademoglu, Ata Akin
   Proceedings of the 2005 IEEE Engineering in Medicine and Biology 27th Annual Conference

A.4 National Conference Proceedings

1. Determination and anatomical mapping of thalamic stroke regions to anatomical atlas
   Talamik İnme bolgelerinin belirlenmesi ve anatomik atlasta eslestirilmesi Ozel, P., Uslu, F.I., **Duru, A.D.,**Erdogan, S.B., Gokyigit, A., Ademoglu, A. 15th National Biomedical Engineering Meeting, BIYOMUT2010

2. Epileptic source localizations based on EEG and SDE measurements
   Yuzeyel ve kortikal EEG verileri ile epileptik odak yerellestirimi **Duru, A.D.,**Akdeniz,

G., Kara, E., Ozkara, Ç., Uzan, M., Ademoglu, A., Demiralp, T. 2010 15th National Biomedical Engineering Meeting, BIYOMUT2010 , art. no. 5479788

3. Sizofren Deneklerden Alınan İşlevsel Yakın Kızılaltı Spektreskopi Verilerinin Altband Filtrelenmesi
   Ercan Kara, Nermin Topaloğlu, Esin Karahan, **Adil Deniz Duru**, Ata Akın, Hasan Herken
   Biyomut 2008

4. EEG Dipol Kaynaklarinin MZMC Yöntemleri ile Yerellestirilmesi
   Gokcen Yildiz, **A.Deniz Duru**, Ahmet Ademoglu
   Biyomut 2007, Mayis 2007

5. Olaya Iliskin Potansiyellere (OIP) Ait Beyin Alt Harita Bilesenlerinin Kaynaklarinin Yerellestirilmesi
   A.D. Duru, A. Bayram, T. Demiralp ve A. Ademoglu
   Istanbul, Biyomut 2006

6. Islevsel Yakin Kizil Otesi Spektroskopu verilerinin Gercek Kafa Modelinin Uzerine Cakistirilmasi
   Emir U., **Duru A.D.**,Ademoglu A., Akin A.
   Biyomut 2005, Istanbul 2005

7. Olaya Iliskin Sureclerin iMRG ve EEG Kaynak Yerellestirimi ile Goruntulenmesi
   Hüseyin Hamdi Eryilmaz, **Adil Deniz Duru**ve Ahmet Ademoglu
   Istanbul, Biyomut 2006

A.5 Conference Abstracts

1. Comparison of Epileptic Source Localizations Based on EEG and SDE Measurements

   Adil Deniz Duru, Gülsüm Akdeniz, Çiğdem Özkara, Mustafa Uzan, Ahmet Ademoglu, Tamer Demiralp

   Annual Meeting of the Organization for Human Brain Mapping 2010

2. Görsel kortekste doğrusallık dışı hemodinamik yanıtlardaki sinirsel mekanizmanın incelenmesi

   Sinem Burcu Erdoğan, **Adil Deniz Duru,**Itır Kaşıkçı, Elif Kurt, Ahmet Ademoğlu, Tamer Demiralp

   Ulusal Sinirbilimleri Konferansı (USK), 2011, Istanbul, Turkiye

3. Radial Basis Function Decomposition of Topographic EEG Maps.

   D. A. Duru, A. Ademoglu and T. Demiralp

   10th International Conference on Cognitive Neuroscience (ICON X), September 1st-5th, 2008, Bodrum, Turkey. Absract Book, p. 446.

4. Combined ICA-Bayesian MCMC Reconstruction of EEG Sources.

   G. Yildiz, **A.D. Duru**, A. Ademoglu and T. Demiralp

   10th International Conference on Cognitive Neuroscience (ICON X), September 1st-5th, 2008, Bodrum, Turkey. Abstract Book, p. 132.

5. Spatiotemporal analysis of event related brain potentials

   Ademoglu A and **Duru A.D.**

   Euro-mediterranean Conference on Biomathematics

   Cairo, 26-28 June 2007

6. Subtopographic EEG Source localization after Spatio-temporal wavelet decomposition

   Adil Deniz Duru, Tamer Demiralp, Ahmet Ademoglu

International Workshop on Image Analysis in the Life Sciences Theory and Applications (IEEE)
Johannes Kepler University, Linz Austria, Feb 28 - March 2,2007

7. Subtopographic EEG Source localization after Spatio-temporal wavelet decomposition
Duru A. D*., Eryilmaz H., Bayram A., Demiralp T., Ademoglu A.
13th World Congress of Pshychophysiology, Istanbul 2006

8. Source Localization of Topographic EEG Maps Prefiltered by Spatio-Temporal Wavelets
A. Ademoglu,, **A. D. Duru**, T. Demiralp
IX. International Conference on Cognitive Neuroscience, Havana Cuba, SEPTEMBER 2005

9. Source Localization of Topographic EEG Maps Prefiltered by Spatio-Temporal Wavelets
A. Ademoglu , **A. D. Duru**, A. Bayram, T. Demiralp
Brain Dynamics and Cognition Conference, Izmir, 2005

10. EEG ve olaya iliskin potansiyellerde gercekci kafa modeli ile kaynak yerellestirimi
Ademoglu, A., **Duru, D.**, Ergen, M. , Istefanopulos, Y., and Baykan, B. , Demiralp, T.
T. III. Ulusal Sinir Bilimleri Kongresi Pamukkale/Denizli 2004

11. Source localization of electrical dipoles using wavelet prefiltering and MUSIC scanning
Ademoglu, A.,**Duru, D.**, Demiralp T., Istefanopulos, Y., and Baykan, B.
Evoked Potentials International Conference XIV, $3th$ National Neuroscience

Congress Leipzig 2004

REFERENCES

1. Knoll, G. F., "Single-photon emission computed tomography," in *Proc. IEEE,*, Vol. 71, pp. 320–329, 1983.

2. Jaszczak, R. J., "Tomographic radiopharmaceutical imaging," in *Proc. IEEE,*, Vol. 76, pp. 1079–1094, 1988.

3. Belliveau, J., D. Kennedy, R. McKinstry, B. Buchbinder, R. Weisskoff, M. Cohen, J. Vevea, T. Brady, and B. Rosen, "Functional mapping of the human visual cortex by magnetic resonance imaging," *Science*, Vol. 254, no. 5032, pp. 716–719, 1991.

4. Baillet, S., J. C. Mosher, and R. M. Leahy, "Electromagnetic brain mapping," *IEEE Signal Processing magazine*, pp. 14–30, November 2001.

5. Berger, H., "Uber das elektroenkephalogramm des menschen," *Archiv fur Psychiatrie und Nervenkrankheiten*, Vol. 87, pp. 527–570, 1929.

6. Scherg, M., T. Best, and P. Berg, "Multiple source analysis of interictal spikes: goals, requirements, and clinical values," *J. Clin. Neurophysiol.*, Vol. 16, pp. 214–224, 1999.

7. Schmit, R. O., "Multiple emitter location and signal parameter estimation," *IEEE Trans. Antennas Propagation*, Vol. 34, pp. 276–280, 1986. reprint of the original paper presented at RADC Spectrum Estimation Workshop, 1979.

8. Ademoglu, A., D. Duru, T. Demiralp, Y. Istefanopulos, and B. Baykan, "Source localization of electrical dipoles using wavelet prefiltering and music scanning," in *Evoked Potentials International Conference XIV Abstract Book*, (Leipzig–Germany), p. 86, Evoked Potentials International Conference XIV, 28-31 March 2004.

9. Demiralp, T., and A. Ademoglu, "Decomposition of event-related brain potentials into multiple functional components using wavelet transform," *Clinical Electroencephalography*, Vol. 32, no. 3, pp. 122–138, 2001.

10. Koenig, T., F. Marti-Lopez, and P. A. Valdes-Sosa, "Topographic time frequency decomposition of the eeg," *NeuroImage*, Vol. 14, pp. 383–390, 2001.

11. Zhukov, L., D. Weinstein, and C. Johnson, "Independent component analysis for eeg source localization an algorithm that reduces the complexity of localizing multiple neural sources," *IEEE Engineering in Medicine and Biology*, pp. 87–96, May/June 2000.

12. Miwakeichi, F., E. Martinez-Montes, P. A. Valdes-Sosa, N. Nishiyama, H. Mizuhara, and Y. Yamaguchia, "Decomposing eeg data into space time frequency components using parallel factor analysis," *NeuroImage*, Vol. 22, pp. 1035–1045, 2004.

13. Wang, K., H. Begleiter, and B. Porjesz, "Spatial enhancement of eventrelated potentials using multiresolution analysis," *Brain Topography*, Vol. 10, no. 3, pp. 191–200, 1998.

14. Ding, L., G. a. Worrell, T. D. Lagerlund, and B. He, "3D source localization of interictal spikes in epilepsy patients with MRI lesions.," *Physics in medicine and biology*, Vol. 51, pp. 4047–62, Aug. 2006.

15. Genow, A., C. Hummel, G. Scheler, R. Hopfenga, M. Kaltenha, M. Buchfelder, J. Romsto, and H. Stefan, "Epilepsy surgery, resection volume and msi localization in lesional frontal lobe epilepsy," *NeuroImage*, Vol. 21, pp. 444–449, 2004.

16. Worrell, G. A., T. D. Lagerlund, F. W. Sharbrough, B. H. Brinkmann, N. E. Busacker, K. M. Cicora, and T. J. Brien, "Localization of the epileptic focus by low-resolution electromagnetic tomography in patients with a lesion demonstrated by mri," *Brain Topography*, Vol. 12, no. 4, pp. 273–282, 2000.

17. Lemieux, L., a. Salek-Haddadi, O. Josephs, P. Allen, N. Toms, C. Scott, K. Krakow, R. Turner, and D. R. Fish, "Event-related fMRI with simultaneous and continuous EEG: description of the method and initial case report.," *NeuroImage*, Vol. 14, pp. 780–7, Sept. 2001.

18. Formaggio, E., S. F. Storti, A. Bertoldo, P. Manganotti, A. Fiaschi, and G. M. Toffolo, "Integrating EEG and fMRI in epilepsy.," *NeuroImage*, Vol. 54, pp. 2719–2731, Nov. 2010.

19. Goldman, R. I., J. M. Stern, J. Engel, and M. S. Cohen, "Simultaneous EEG and fMRI of the alpha rhythm.," *Neuroreport*, Vol. 13, pp. 2487–92, Dec. 2002.

20. Laufs, H., a. Kleinschmidt, a. Beyerle, E. Eger, a. Salek-Haddadi, C. Preibisch, and K. Krakow, "EEG-correlated fMRI of human alpha activity," *NeuroImage*, Vol. 19, pp. 1463–1476, Aug. 2003.

21. Friston, K. J., P. Jezzard, and R. Turner, "Analysis of functional MRI time-series," *Human Brain Mapping*, Vol. 1, no. 2, pp. 153–171, 1994.

22. Esposito, F., A. Aragri, T. Piccoli, G. Tedeschi, R. Goebel, and F. Di Salle, "Distributed analysis of simultaneous EEG-fMRI time-series: modeling and interpretation issues.," *Magnetic resonance imaging*, Vol. 27, pp. 1120–30, Oct. 2009.

23. Henson, R. N., G. Flandin, K. J. Friston, and J. Mattout, "A Parametric Empirical Bayesian framework for fMRI-constrained MEG/EEG source reconstruction.," *Human brain mapping*, Vol. 00, Jan. 2010.

24. Liu, a. K., J. W. Belliveau, and a. M. Dale, "Spatiotemporal imaging of human brain activity using functional MRI constrained magnetoencephalography data: Monte Carlo simulations.," *Proceedings of the National Academy of Sciences of the United States of America*, Vol. 95, pp. 8945–50, July 1998.

25. Babiloni, F., C. Babiloni, F. Carducci, L. Angelone, C. D. Gratta, G. L. Romani, P. M. Rossini, and F. Cincotti, "Linear inverse estimation of cortical sources by using high resolution eeg and fmri priors," *IJBEM*, Vol. 3, no. 1, pp. 1–11, 2001.

26. Phillips, C., M. D. Rugg, and K. J. Friston, "Anatomically Informed Basis Functions for EEG Source Localization: Combining Functional and Anatomical Constraints," *NeuroImage*, Vol. 16, pp. 678–695, July 2002.

27. Yang, L., Z. Liu, and B. He, "EEG-fMRI reciprocal functional neuroimaging.," *Clinical neurophysiology : official journal of the International Federation of Clinical Neurophysiology*, Vol. 121, pp. 1240–1250, Apr. 2010.

28. Henson, R. N., D. G. Wakeman, V. Litvak, and K. J. Friston, "A parametric empirical bayesian framework for the eeg/meg inverse problem: Generative models for multi-subject and multi-modal integration," *Front Hum Neurosci.*, Vol. 5, no. 76, pp. 1–16, 2011.

29. Hallez, H., B. Vanrumste, R. Grech, J. Muscat, W. D. Clercq, A. Vergult, Y. D'Asseler, K. P. Camilleri, S. G. Fabri, S. V. Huffel, and I. Lemahieu, "Review on solving the forward problem in EEG source analysis.," *Journal of neuroengineering and rehabilitation*, Vol. 4, p. 46, Jan. 2007.

30. Nunez, P., and R. Srinivasan, *Electric Fields of the Brain: The Neurophysics of EEG*, Oxford University Press, 2nd ed., 2006.

31. Plonsey, R., "Action potential sources and their volume conductor fields," in *Proceedings of the IEEE*, Vol. 65, pp. 601–611, 1977.

32. Lytton, W., *From Computer to Brain: Foundations of Computational Neuroscience*, Springer, 2002.

33. Schaul, N., "The fundamental neural mechanisms of electroencephalography," *Electroencephalography and clinical Neurophysiology*, Vol. 106, pp. 101–107, 1998.

34. Ramo, Simon, Whinnery, R. John, and T. van Duzer, *Fields and Waves in Communication Electronics*, John Wiley & Sons, 1984.

35. Oostendorp, T., J. Delbeke, and D. Stegeman, "The conductivity of the human skull: results of in vivo and in vitro measurements.," *Biomedical Engineering, IEEE Transactions*, Vol. 47, no. 11, pp. 1487–1492, 2000.

36. Goncalves, S., J. de Munck, J. Verbunt, F. Bijma, R. Heethaar, and F. L. da Silva, "In vivo measurement of the brain and skull resistivities using an eit-based method and realistic models for the head.," *Biomedical Engineering, IEEE Transactions*, Vol. 50, no. 6, pp. 754–767, 2003.

37. Lai, Y., W. van Drongelen, L. Ding, K. E. Hecox, V. L. Towle, D. M. Frim, and B. He, "Estimation of in vivo human brain-to-skull conductivity ratio from simultaneous extra and intra-cranial electrical potential recordings.," *Clin Neurophysiol*, Vol. 116, no. 2, pp. 456–465, 2005.

38. Rush, S., and D. Driscoll, "Current distribution in the brain from surface electrodes.," *Anesthesia and analgesia*, Vol. 47, no. 6, pp. 717–723, 1967.

39. Geddes, L. A., and L. E. Baker, "The specific resistance of biological material a compendium of data for the biomedical engineer and physiologist," *Med Biol Eng*, Vol. 5, no. 3, pp. 271–293, 1967.

40. Basser P, Mattiello J, L. D., "Mr diffusion tensor spectroscopy and imaging.," *Biophysical Journal*, Vol. 66, pp. 259–267, 1994.

41. Tuch, D., V. Wedeen, A. Dale, J. George, and J. Belliveau, "Conductivity tensor mapping of the human brain using diffusion tensor mri," in *Proceedings in National Academie of Science 2001*, Vol. 98, pp. 11697–11701, 2001.

42. Wolters, C. H., A. Anwander, X. Tricoche, D. Weinstein, M. A. Koch, and R. S. MacLeod, "Influence of tissue conductivity anisotropy on eeg/meg field and return current computation in a realistic head model: a simulation and visualization study using high resolution finite element modeling.," *Neuroimage*, Vol. 30, pp. 813–826, 2006.

43. Haueisen, J., D. Tuch, C. Ramon, P. Schimpf, V. Wedeen, J. George, and J. Belliveau, "The influence of brain tissue anisotropy on human eeg and meg.," *NeuroImage*, Vol. 15, pp. 159–166, 2002.

44. Hallez, H., P. V. Hese, B. Vanrumste, P. Boon, Y. D'Asseler, I. Lemahieu, and R. V. de Walle, "Dipole localization errors due to not incorporating compartments with anisotropic conductivities: Simulation study in a spherical head model.," *International Journal of Bioelectromagnetism*, Vol. 7, pp. 134–137, 2005.

45. Pursula, A., J. Nenonen, E. Somersalo, E. Ilmoniemi, and T. Katila, "Bioelectromagnetic calculations in anisotropic volume conducters," in *Proceedings of Biomag2000*, pp. 659–662, 2000.

46. Sun, M., "An efficient algorithm for computing multishell spherical volume conductor models in eeg dipole source localization," *IEEE Trans. on Biomdical Eng.*, Vol. 44, pp. 1243–1252, December 1997.

47. de Munck, J. C., and M. J. Peters, "A fast method to compute the potential in the multisphere model," *IEEE Transactions on Biomedical Engineering*, Vol. 40, no. 11, pp. 1166–1174, 1993.

48. Fuchs, M., J. Kastner, M. Wagner, S. Hawes, and J. Ebersole, "A standardized boundary element method volume conductor model.," *Clinical neurophysiology*, Vol. 113, no. 5, pp. 702–712, 2002.

49. Vatta, F., F. Meneghini, F. Esposito, S. Mininel, and F. D. Salle, "Realistic and spherical head modeling for eeg forward problem solution: a comparative cortex-based analysis.," *Computational intelligence and neuroscience*, pp. 1–11, 2010.

50. Roth, B., A. Gorbach, and S. Sato, "How well does a three-shell model predict positions of dipoles in a realistically shaped head?," *Electroencephalography and Clinical Neurophysiology*, Vol. 87, pp. 175–184, 1993.

51. Roth, B. J., D. Ko, I. R. von Albertini-Carletti, D. Scaffidi, and S. Sato, "Dipole localization in patients with epilepsy using the realistic shaped head model.," *Electroencephalography and Clinical Neurophysiology*, Vol. 102, no. 3, pp. 160–166, 1997.

52. Huiskamp, G., M. Vroeijenstijn, R. van Dijk, G. Wieneke, and A. van Huffelen, "The need for correct realistic geometry in the inverse eeg problem.," *IEEE Transactions on Biomedical Engineering*, Vol. 46, no. 11, pp. 1281–1287, 1999.

53. Cuffin, B. N., "Effects of local variations in skull and scalp thickness on eeg's and meg's.," *IEEE Transactions on Biomedical Engineering*, Vol. 40, pp. 42–48, 1993.

54. Chauveau, N., X. Franceries, B. Doyon, B. Rigaud, J. P. Morucci, and P. Celsis, "Effects of skull thickness, anisotropy, and inhomogeneity on forward eeg/erp computations using a spherical three dimensional resistor mesh model.," *Human Brain Mapping*, Vol. 21, no. 2, pp. 86–97, 2003.

55. Frackowiak, R., K. Friston, C. Frith, R. Dolan, C. Price, S. Zeki, J. Ashburner, and W. Penny, *Human Brain Function*, Academic Press, 2nd ed., 2003.

56. Ashburner, J., and K. Friston, "Unified segmentation," *NeuroImage*, Vol. 26, pp. 839–851, 2005.

57. Fletcher, D. J., A. Amir, D. L. Jewett, and G. Fein, "Improved method for computation of potentials in a realistic head shape model.," *IEEE transactions on biomedical engineering*, Vol. 42, no. 11, pp. 1094–1104, 1995.

58. Ferguson, A. S., X. Zhang, and G. Stroink, "A complete linear discretization for calculating the magnetic field using the boundary element method.," *IEEE transactions on bio-medical engineering*, Vol. 41, no. 5, pp. 455–460, 1994.

59. Ferguson, A. S., and G. Stroink, "Factors affecting the accuracy of the boundary element method in the forward problem. i. calculating surface potentials," *IEEE Trans. Biomed. Engng*, Vol. 44, pp. 1139–1155, November 1997.

60. de Munck, J. C., "A linear discreatization of the volume conductor boundary integral equations using analytically integrated elements," *IEEE transactions on bio-medical engineering*, Vol. 39, no. 9, pp. 986–990, 1992.

61. Srebro, R., "A modified boundary element method for the estimation of potential fields on the scalp," *IEEE transactions on bio-medical engineering*, Vol. 43, no. 6, pp. 650–653, 1996.

62. Lorensen, W., and H. Cline, "Marching cubes: A high resolution 3d surface construction algorithm," in *Proceedings of the 14th annual conference on Computer graphics and interactive techniques*, Vol. 21, 1987.

63. Sarvas, J., "Realistic Conductivity Geometry Model of the Human Head for Interpretation of Neuromagnetic Data," *IEEE Trans Biomed Eng*, Vol. 36, no. 2, pp. 1–7, 1989.

64. Meijs, J. W., O. W. Weier, M. J. Peters, and A. V. Oosterom, "On the numerical accuracy of the boundary element method," *IEEE transactions on bio-medical engineering*, Vol. 36, no. 10, pp. 1038–1049, 1989.

65. Schlitt, H., L. Heller, R. Aaron, E. Best, and D. M. Ranken, "Evaluation of boundary element methods for the eeg forward problem: effect of linear interpolation.," *IEEE transactions on bio-medical engineering*, Vol. 42, no. 1, pp. 52–58, 1995.

66. Hamalainen, M., and R. Ilmoniemi, "Interpreting measured magnetic fields of the brain: estimates of current distributions.," preprint, Helsinki University of Technology, 1984. Technical Report.

67. Schimpf, P., C. Ramon, and J. Haueisen, "Dipole models for the eeg and meg," *Biomedical Engineering, IEEE Transactions on*, Vol. 49, pp. 409 –418, may 2002.

68. Wolters, C. H., M. Kuhn, A. Anwander, and S. Reitzinger, "A parallel algebraic multigrid solver for finite element method based source localization in the human brain," *Computing and Visualization in Science*, no. 5, pp. 165–177, 2002.

69. Kauppinen, P., J. Hyttinen, P. Laarne, and J. Malmivuo, "A software implementation for detailed volume conductor modelling in electrophysiology using finite difference method.," *Computer methods and programs in biomedicine*, Vol. 58, pp. 191–203, Feb. 1999.

70. Jing, L., Z. Shanan, and B. He., "A finite difference method for solving the three-dimensional eeg forward problem.," in *Annual International Conference of the IEEE Engineering in Medicine and Biology Society. IEEE Engineering in Medicine and Biology Society.*, Vol. 3, pp. 1540–1543, 2005.

71. Darvas, F., D. Pantazis, and R. M. Leahy, "Mapping human brain function with meg and eeg : methods and validation.," *NeuroImage*, Vol. 23, pp. 289–299, 2004.

72. Lederman, C., A. Joshi, I. Dinov, L. Vese, A. Toga, and J. D. Van Horn, "The generation of tetrahedral mesh models for neuroanatomical MRI.," *NeuroImage*, Vol. 55, pp. 153–64, Mar. 2011.

73. Scherg, M., and D. von Cramon, "A new interpretation of the generators of baep waves i-v: results of a spatio-temporal dipole model.," *Electroencephalogry and Clin Neurophysiol.*, Vol. 62, pp. 290–299, Jul 1985.

74. Cuffin, B. N., "A method for localizing eeg sources in realistic head models.," *IEEE transactions on bio-medical engineering*, Vol. 42, pp. 68–71, Jan 1995.

75. Finke, S., R. Gulrajani, and J. Gotman, "Conventional and reciprocal approaches to the inverse dipole localization problem of electroencephalography," *Biomedical Engineering, IEEE Transactions on*, Vol. 50, pp. 657 –666, june 2003.

76. Aine, C., M. Huang, J. Stephen, and R. Christopher, "Multistart algorithms for meg empirical data analysis reliably characterize locations and time courses of multiple sources," *NeuroImage*, Vol. 12, pp. 159–179, 2000.

77. Miltner, W., C. Braun, R. E. Johnson, and A. D. S. Rutchkin, "A test of brain electrical source analysis (besa): a simulation study," *Electroencephalogr. Clin. Neurophysiol.*, Vol. 91, pp. 295–310, 1994.

78. Scherg, M., and J. S. Ebersole, "Brain source imaging of focal and multifocal epileptiform eeg activity," *Clin. Neurophysiol.*, Vol. 24, pp. 51–60, 1994.

79. Mosher, J. C., P. S. Lewis, and R. M. Leahy, "Multiple dipole modeling and localization from spatio-temporal meg data," *IEEE Trans. On Biomedical Engineering,*, Vol. 39, no. 6, pp. 541–557, 1992.

80. Mosher, J. C., and R. M. Leahy, "Source Localization Using Recursively Applied and Projected (RAP) MUSIC," *IEEE Trans. Signal Processing*, Vol. 47, no. 2, pp. 332–340, 1999.

81. Mosher, J. C., and R. M. Leahy, "Recursive music: a framework for eeg and meg source localization," *IEEE Trans. Biomed. Engng*, Vol. 45, no. 11, pp. 1342–1354, 1998.

82. Mosher, J. C., R. M. Leahy, and P. S. Lewis, "Eeg and meg: forward solutions for inverse methods," *IEEE Trans. Biomed. Engng*, Vol. 46, no. 3, pp. 245–259, 1999.

83. Gavaret, M., J. M. Badier, P. Marquis, F. Bartolomei, and P. Chauvel, "Electric source imaging in temporal lobe epilepsy.," *J Clin Neurophysiol*, Vol. 21, no. 4, pp. 267–282, 2004.

84. Gavaret, M., J. M. Badier, P. Marquis, A. McGonigal, F. Bartolomei, and J. Regis, "Electric source imaging in frontal lobe epilepsy.," *J Clin Neurophysiol*, Vol. 23, no. 4, pp. 358–370, 2006.

85. Kobayashi, K., T. Akiyama, T. Nakahori, H. Yoshinaga, and J. Gotman, "Systematic source estimation of spikes by a combination of independent component analysis, rapmusic. i: principles and simulation study.," *Clin Neurophysiol*, Vol. 113, no. 5, pp. 713–724, 2002.

86. Kobayashi, K., T. Akiyama, T. Nakahori, H. Yoshinaga, and J. Gotman, "Systematic source estimation of spikes by a combination of independent component analysis, rapmusic. ii: preliminary clinical application.," *Clin Neurophysiol*, Vol. 113, no. 5, pp. 725–734, 2002.

87. Dale, A., and M. Sereno, "Improved Localization of Cortical Activity By Combining EEG and MEG with MRI Cortical Surface Reconstruction," *Neuroscience*, Vol. 3, pp. 59–70, 1992.

88. Pascual-marqui, R. D., "Review of Methods for Solving the EEG Inverse Problem," *International Journal*, Vol. 1, no. 1, pp. 75–86, 1999.

89. Gorodnitsky, I. F., S. J. George, and R. D. Bhaskar, "Neuromagnetic source imaging with focuss: a recursive weighted minimum norm algorithm," *Electroencephalogry and Clin Neurophysiol.*, Vol. 95, pp. 231–251, May 1995.

90. Grech, R., T. Cassar, J. Muscat, K. P. Camilleri, S. G. Fabri, M. Zervakis, P. Xanthopoulos, V. Sakkalis, and B. Vanrumste, "Review on solving the inverse problem in EEG source analysis.," *Journal of neuroengineering and rehabilitation*, Vol. 5, p. 25, Jan. 2008.

91. Pascual-Marqui, R. D., C. M. Michel, and D. Lehmann, "Low resolution electromagnetic tomography: A new method for localizing electrical activity in the brain.," *Int. J. Psychophysiol.*, Vol. 18, pp. 49–65, 1994.

92. Menendez, G. R. D. P., M. M. Murray, C. M. Michel, R. Martuzzi, S. L. Gonzalez, and E. Laura., "Electrical neuroimaging based on biophysical constraints.," *Neuroimage*, Vol. 21, pp. 527–539, 2004.

93. Pascual-Marqui, R. D., "Standardized low resolution brain electromagnetic tomography (sloreta): technical details.," *Methods, Findings in Experimental Clinical Pharmacology*, Vol. 24, pp. 5–12, 2002.

94. Sekihara, K., S. Maneesh, and S. S. Nagarajan, "Localization bias and spatial resolution of adaptive and non-adaptive spatial filters for meg source reconstruction.," *NeuroImage*, Vol. 25, pp. 1056–1067, 2005.

95. Mattout, J., C. Phillips, W. D. Penny, M. D. Rugg, and K. J. Friston, "MEG source localization under multiple constraints: an extended Bayesian framework.," *NeuroImage*, Vol. 30, pp. 753–67, Apr. 2006.

96. Friston, K., L. Harrison, J. Daunizeau, S. Kiebel, C. Phillips, N. Trujillo-Barreto, R. Henson, G. Flandin, and J. Mattout, "Multiple sparse priors for the M/EEG inverse problem.," *NeuroImage*, Vol. 39, pp. 1104–20, Mar. 2008.

97. Andino, S. L. G., R. G. de Peralta Menendez, C. M. Lantz, O. Blank, C. M. Michel, and T. Landis, "Non-stationary distributed source approximation: An alternative to improve localization procedures," *Human Brain Mapping*, Vol. 14, pp. 81–95, 2001.

98. Marquardt, D., "An algorithm for least-squares estimation of nonlinear parameters," *SIAM J. Appl. Math.*, Vol. 11, pp. 431–441, 1963.

99. Levenberg, K., "A method for the solution of certain problems in least squares," *Quart. Appl. Math.*, Vol. 2, pp. 164–168, 1944.

100. Duru, A. D., and A. Ademoglu, "Source localization of subtopographies decomposed by radial basis functions," in *Medical Imaging and Augmented Reality* (Dohi, T., I. Sakuma, and H. Liao, eds.), Vol. 5128 of *Lecture Notes in Computer Science*, pp. 108–115, Springer Berlin / Heidelberg, 2008.

101. Meyer, Y., *Wavelets and operators*, Cambridge University Press, 1990.

102. Daubechies, I., "Orthonormal bases of compactly supported wavelets.," *Comm. in Pure and Applied Math.*, Vol. 41, pp. 909–996, 1988.

103. Grossman, A., and J. Morlet, "Decomposition of hardy functions into square integrable wavelets of constant shape," *SIAM J Math. Anal.*, Vol. 15, pp. 723–736, 1984.

104. Mallat, S., "A theory for multiresolution signal decomposition: The wavelet representation.," *IEEE Transactions on Pattern Analysis and Machine Intelligence*, Vol. 11, pp. 674–693, 1989.

105. Duru, A. D., A. Bayram, T. Demiralp, and A. Ademoglu, "Source localization of subtopographic brain maps for event related potentials (erp)," in *Engineering in Medicine and Biology Society, 2006. EMBS '06. 28th Annual International Conference of the IEEE*, pp. 4832 –4834, 30 2006-sept. 3 2006.

106. Duru, A. D., A. Bayram, T. Demiralp, and A. Ademoglu, *Source Localization of Subtopographic Brain Maps for Event Related Potentials (ERP)*, Vol. 3 of *Encyclopedia of Healthcare Information Systems*, pp. 1247–1252. New York: Information Science Reference (an imprint of IGI Global), 2008.

107. "Statistical parameter mapping toolbox http://www.fil.ion.ucl.ac.uk/spm/," *(SPM)*, 2005.

108. Duru, A. D., A. Ademoglu, and T. Demiralp, "Analysis of brain electrical topography by spatio-temporal wavelet decomposition," *Mathematical and Computer Modelling*, Vol. 49, pp. 2224–2235, June 2009.

109. Alsan, E. K., Z. Bayraktaroglu, H. Gurvit, Y. H. Keskin, M. Emre, and T. Demiralp, "Comparative analysis of event-related potentials during go/nogo and cpt: Decomposition of electrophysiological markers of response inhibition and sustained attention," *Brain Research*, Vol. 1104, pp. 114–128, 2006.

110. Guyton, A. C., *Textbook of Medical Physiology*, Philadelphia: W. B. Saunders Company, 7th ed., 1986.

111. Miller, J. W., and A. J. Cole, "Is it necessary to define the ictal onset zone with eeg prior to performing resective epilepsy surgery?," *Epilepsy & behavior*, Vol. 2, pp. 178–181, February 2011.

112. Duncan, J. S., "Selecting patients for epilepsy surgery: synthesis of data.," *Epilepsy & behavior*, Vol. 2, pp. 230–232, February 2011.

113. Silva, L., *EEG analysis: theory and practice.*, pp. 1135–1164. Electroencephalography: Basic Principles, Clinical Applications and Related Fields, Baltimore: Williams Wilkins, 4 ed., 1999. In: E. Niedermeyer and F. Lopes da Silva (Eds.).

114. Jansen, F. E., G. Huiskamp, A. C. van Huffelen, M. Bourez-Swart, E. Boere, T. Gebbink, K. L. Vincken, and O. van Nieuwenhuizen, "Identification of the epileptogenic tuber in patients with tuberous sclerosis: A comparison of high-resolution eeg and meg," *Epilepsia*, Vol. 47, no. 1, pp. 108–114, 2006.

115. Brodbeck, V., L. Spinelli, A. M. Lascano, M. Wissmeier, M. I. Vargas, S. Vulliemoz, C. Pollo, K. Schaller, C. M. Michel, and M. Seeck, "Electroencephalographic source imaging: a prospective study of 152 operated epileptic patients.," *Brain, A journal of Neurology*, Vol. 134, no. 10, pp. 2887–2897, 2011.

116. Kuruvilla, A., and R. Flink, "Intraoperative electrocorticography in epilepsy surgery: useful or not?," *Seizure*, Vol. 12, pp. 577–584, 2003.

117. Dümpelmann, M., J. Fell, J. Wellmer, H. Urbach, and C. E. Elger, "3D source localization derived from subdural strip and grid electrodes: a simulation study.," *Clinical neurophysiology : official journal of the International Federation of Clinical Neurophysiology*, Vol. 120, pp. 1061–9, June 2009.

118. Grova, C., J. Daunizeau, J.-M. M. Lina, C. G. Bénar, H. Benali, and J. Gotman, "Evaluation of eeg localization methods using realistic simulations of interictal spikes," *NeuorImage*, Vol. 29, pp. 734–753, 2006.

119. Rullmann, M., A. Anwander, M. Dannhauer, S. K. Warfield, F. H. Duffy, and C. H. Wolters, "Neuroimage eeg source analysis of epileptiform activity using a 1 mm anisotropic hexahedra finite element head model.," *NeuroImage*, Vol. 44, no. 2, pp. 399–410, 2009.

120. Saleheen, H., and K. Ng, "New finite difference formulations for general inhomogeneous anisotropic bioelectric problems," *Biomedical Engineering, IEEE Transactions on*, Vol. 44, pp. 800 –809, sept. 1997.

121. Yamashita, O., A. Galka, T. Ozaki, R. Biscay, and P. Valdes-Sosa, "Recursive penalized least squares solution for dynamical inverse problems of eeg generation," *Human Brain Mapping*, Vol. 21, pp. 221–235, 2004.

122. Duru, A., H. Eryilmaz, U. Emir, Z. Bayraktaroglu, T. Demiralp, and A. Ademoglu, "Implementation of low resolution electro-magnetic tomography with fmri statistical maps on realistic head models," in *Engineering in Medicine and Biology Society, 2007. EMBS 2007. 29th Annual International Conference of the IEEE*, pp. 5239 –5242, aug. 2007.

123. Galka, A., O. Yamashita, T. Ozaki, R. Biscay, and P. Valdes-Sosa., "A solution to the dynamical inverse problem of eeg generation using spatiotemporal kalman filtering.," *NeuroImage*, Vol. 23, pp. 435–453, 2004.

124. Friston, K., R. Henson, C. Phillips, and J. Mattout, "Bayesian estimation of evoked and induced responses.," *Human brain mapping*, Vol. 27, pp. 722–35, Sept. 2006.

125. Duru, A. D., and A. Ademoglu, "Epileptic source localization: Deep electrode measurements versus scalp eeg," *International Journal of Bioelectromagnetism*, Vol. 11, no. 4, pp. 175–178, 2009.

126. Logothetis, N., J. Pauls, M. Augath, T. Trinath, and A. Oeltermann, "Neurophysiological investigation of the basis of the fmri signal," *Nature*, Vol. 412, no. 954, pp. 150–157, 2001.

127. Nunez, P. L., "Toward a quantitative description of large-scale neocortical dynamic function and eeg," *Behavioral and Brain Sciences*, Vol. 23, no. 3, pp. 371–398, 2000. Discussion 399-437.

128. Basar, E., and T. H. Bullock, *Induced Rhythms in the Brain.*, Springer Verlag, 1992.

129. Basar, E., M. Schürmann, C. Başar-Eroglu, and T. Demiralp, "Selectively distributed gamma band system of the brain.," *Int J Psychophysiol*, Vol. 39, no. 2-3, pp. 129–135, 2001.

130. Rugg, M. D., "Convergent approaches to electrophysiological and hemodynamic investigations of memory.," *Hum Brain Mapp*, Vol. 6, pp. 394–398, 1998.

131. Nunez, P. L., and R. B. Silberstein, "On the relationship of synaptic activity to macroscopic measurements: does co-registration of eeg with fmri make sense?," *Brain Topogr*, Vol. 13, pp. 79–96, 2000.

132. Debener, S., M. Ullsperger, M. Siegel, and A. K. Engel, "Single-trial eeg-fmri reveals the dynamics of cognitive function.," *Trends Cogn Sci*, Vol. 10, pp. 558–563, 2006.

133. Ritter, P., and A. Villringer, "Simultaneous eeg-fmri.," *Neurosci Biobehav Rev*, Vol. 30, pp. 823–838, 2006.

134. Goldman, R. I., J. M. Stern, J. Engel, and M. S. Cohen, "Simultaneous eeg and fmri of the alpha rhythm.," *Neuroreport*, Vol. 13, no. 18, pp. 2487–2492, 2002.

135. Sato, J. a. R., C. Rondinoni, M. Sturzbecher, D. B. de Araujo, and E. Amaro, "From EEG to BOLD: brain mapping and estimating transfer functions in simultaneous EEG-fMRI acquisitions.," *NeuroImage*, Vol. 50, pp. 1416–26, May 2010.

136. Sotero, R. C., N. J. Trujillo-Barreto, Y. Iturria-Medina, F. Carbonell, and J. C. Jimenez, "Realistically coupled neural mass models can generate EEG rhythms.," *Neural computation*, Vol. 19, pp. 478–512, Feb. 2007.

137. Riera, J. J., J. Watanabe, I. Kazuki, M. Naoki, E. Aubert, T. Ozaki, and R. Kawashima, "A state-space model of the hemodynamic approach: nonlinear filtering of BOLD signals.," *NeuroImage*, Vol. 21, pp. 547–67, Feb. 2004.

138. Moosmann, M., "Correlates of alpha rhythm in functional magnetic resonance imaging and near infrared spectroscopy," *NeuroImage*, Vol. 20, pp. 145–158, Sept. 2003.

139. Martinez-Montes, E., P. a. Valdes-Sosa, F. Miwakeichi, R. I. Goldman, and M. S. Cohen, "Corrigendum to Concurrent EEG/fMRI analysis by multiway partial least squares," *NeuroImage*, Vol. 26, pp. 973–973, July 2005.

140. Daunizeau, J., and K. J. Friston, "A mesostate-space model for EEG and MEG.," *NeuroImage*, Vol. 38, pp. 67–81, Oct. 2007.

141. Rosa, M. J., J. Daunizeau, and K. J. Friston, "EEG-fMRI Integration a critical review of biophysical modeling and data analysis approaches," *Journal of Integrative Neuroscience*, Vol. 09, no. 04, p. 453, 2010.

142. Valdes-Sosa, P. A., J. M. Sanchez-Bornot, R. C. Sotero, Y. Iturria-Medina, Y. Aleman-Gomez, J. Bosch-Bayard, F. Carbonell, and T. Ozaki, "Model driven EEG/fMRI fusion of brain oscillations.," *Human brain mapping*, Vol. 30, pp. 2701–21, Sept. 2009.

143. Regan, D., *Human brain electrophysiology: evoked potentials and evoked magnetic fields in science and medicine.*, New York: Elsevier, 1989.

144. Herrmann, C. S., "Human eeg responses to 1-100 hz flicker: resonance phenomena in visual cortex and their potential correlation to cognitive phenomena.," *Experimental Brain Res*, Vol. 137, no. 3-4, pp. 346–353, 2001.

145. Pastor, M. a., J. Artieda, J. Arbizu, M. Valencia, and J. C. Masdeu, "Human cerebral activation during steady-state visual-evoked responses.," *The Journal of neuroscience : the official journal of the Society for Neuroscience*, Vol. 23, pp. 11621–7, Dec. 2003.

146. Gutschalk, a., R. Mase, R. Roth, N. Ille, a. Rupp, S. Hähnel, T. W. Picton, and M. Scherg, "Deconvolution of 40 Hz steady-state fields reveals two overlapping source activities of the human auditory cortex.," *Clinical neurophysiology : official journal of the International Federation of Clinical Neurophysiology*, Vol. 110, pp. 856–68, May 1999.

147. Rosa, M. J., J. Kilner, F. Blankenburg, O. Josephs, and W. Penny, "Estimating the transfer function from neuronal activity to BOLD using simultaneous EEG-fMRI.," *NeuroImage*, Vol. 49, pp. 1496–509, Jan. 2010.

148. Wan, X., J. Riera, K. Iwata, M. Takahashi, T. Wakabayashi, and R. Kawashima, "The neural basis of the hemodynamic response nonlinearity in human primary visual cortex: Implications for neurovascular coupling mechanism.," *NeuroImage*, Vol. 32, pp. 616–25, Aug. 2006.

149. Buxton, R. B., *Introduction to Functional Magnetic Resonance Imaging*, Cambridge University Press, 2002.

150. Hu, X., T. H. Le, T. Parrish, and P. Erhard, "Retrospective estimation and correction of physiological fluctuation in functional mri.," *Magn. Reson. Med.*, no. 34, pp. 201–212, 1995.

151. Allen, P. J., G. Polizzi, K. Krakow, D. R. Fish, and L. Lemieux, "Identification of EEG events in the MR scanner: the problem of pulse artifact and a method for its subtraction.," *NeuroImage*, Vol. 8, pp. 229–39, Oct. 1998.

152. "Statistical parameter mapping toolbox http://www.fil.ion.ucl.ac.uk/spm/," *(SPM)*, 2008.

153. Phillips, C., J. Mattout, M. D. Rugg, P. Maquet, and K. J. Friston, "An empirical Bayesian solution to the source reconstruction problem in EEG.," *NeuroImage*, Vol. 24, pp. 997–1011, Feb. 2005.

154. Friston, K. J., a. P. Holmes, K. J. Worsley, J.-P. Poline, C. D. Frith, and R. S. J. Frackowiak, "Statistical parametric maps in functional imaging: A general linear approach," *Human Brain Mapping*, Vol. 2, no. 4, pp. 189–210, 1994.

155. Woolrich, M. W., B. D. Ripley, M. Brady, and S. M. Smith, "Temporal autocorrelation in univariate linear modeling of fmri data," *NeuroImage*, Vol. 14, pp. 1370–86, 2001.

156. Srinivasan, R., E. Fornari, M. G. Knyazeva, R. Meuli, and P. Maeder, "fmri responses in medial frontal cortex that depend on the temporal frequency of visual input," *Experimental Brain Res*, Vol. 180, no. 4, pp. 677–691, 2007.

157. Sammer, G., C. Blecker, H. Gebhardt, P. Kirsch, R. Stark, and D. Vaitl, "Acquisition of typical EEG waveforms during fMRI: SSVEP, LRP, and frontal theta.," *NeuroImage*, Vol. 24, pp. 1012–24, Feb. 2005.

158. Krolak-Salmon, P., M. A. Henaff, C. Tallon-Baudry, B. Yvert, M. Guenot, A. Vighetto, F. Mauguiere, and O. Bertrand, "Human lateral geniculate nucleus and visual cortex respond to screen flicker," *Ann. Neurol.*, Vol. 53, no. 1, pp. 73–80, 2003.

159. Rosa, M. J., J. Daunizeau, and K. J. Friston, "EEG-fMRI integration : A critical review of biophysical modelling and data analysis," no. 44, pp. 1–39.

160. Zhang, Y., L. Ding, W. van Drongelen, K. Hecox, D. M. Frim, and B. He, "A cortical potential imaging study from simultaneous extra- and intracranial electrical recordings by means of the finite element method.," *NeuroImage*, Vol. 31, pp. 1513–24, July 2006.